ATLAS CONF Note

ATLAS-CONF-2021-053

2nd November 2021

Combined measurements of Higgs boson production and decay using up to 139 fb^{-1} of proton–proton collision data at $\sqrt{s}$ = 13 TeV collected with the ATLAS experiment

The ATLAS Collaboration

A combination of measurements of Higgs boson production cross sections and branching fractions is presented. The combination is based on the analyses of the Higgs boson decay modes $H \to \gamma\gamma$, ZZ^*, WW^*, $\tau\tau$, $b\bar{b}$, $\mu\mu$, $Z\gamma$ and searches for decays into invisible final states using up to 139 fb^{-1} of proton–proton collision data collected at $\sqrt{s}$ = 13 TeV with the ATLAS detector. Combined cross section measurements are presented for the gluon–gluon fusion (ggF) and vector-boson fusion (VBF) processes, and for associated production with vector bosons (VH) or top-quarks ($t\bar{t}H$, tH). Compared to the previous combined measurement, the $Z\gamma$ decay mode is included for the first time, together with a few additional production processes in the $b\bar{b}$ and $\tau\tau$ decay channels. In addition, several of the previous input measurements are updated to the full Run 2 data set. The global signal strength, defined as the measured Higgs boson signal yield normalised to its SM prediction, is determined to be 1.06 ± 0.06. Measurements in kinematic regions defined within the simplified template cross section framework are also reported. The results are interpreted in terms of modifiers applied to the Standard Model couplings of the Higgs boson to other particles, and are also used to set exclusion limits on parameters in the Standard Model Effective Field Theory framework and in several benchmark scenarios of the Two Higgs Doublet Model. No significant deviations from Standard Model predictions are observed.

ATLAS-CONF-2021-053
02 November 2021

1 Introduction

Following the discovery of the Higgs boson (H) [1–6] by the ATLAS [7] and CMS [8] experiments, its properties have been probed using proton–proton (pp) collision data produced by the Large Hadron Collider (LHC) at CERN. The coupling properties of the Higgs boson to other Standard Model (SM) particles, such as its production cross sections in pp collisions and decay branching fractions, can be precisely computed within the SM, given the value of the Higgs boson mass. Measurements of these properties can therefore provide stringent tests of the validity of the SM.

Higgs boson production and decay rates were measured using the Run 1 data set collected in the years 2011 and 2012, through the combination of ATLAS and CMS measurements [9]. These measurements have been extended using the Run 2 data set recorded by the ATLAS detector from 2015 to 2018, using up to 139 fb^{-1} of pp collision data produced by the LHC. The analyses target several production and decay modes, including: multiple production modes for the $H\to\gamma\gamma$ [10], $H\to ZZ^*\to 4\ell$[1] [11], $H\to WW^*$ [12], $H\to\tau\tau$ [13] decay channels; the $H\to b\bar{b}$ decay channel probed in three exclusive production modes: in association with a weak vector boson (VH, where $V = W$ or Z) [14–16], in the weak vector-boson fusion (VBF) production process [17], and in association with a top–antitop pair ($t\bar{t}H$) [18]; $t\bar{t}H$ production in multilepton final states (WW^*, ZZ^* and $\tau\tau$) [19]; the $H\to\mu\mu$ decay channel [20]; the $H\to Z\gamma$ decay channel [21]; and the Higgs boson decays into invisible final states ($H\to inv$) produced via the VBF process [22]. In the latter case, no other Higgs boson production modes are considered since the corresponding current measurements do not significantly improve the signal sensitivity. This note presents an update of the previous combined measurement of Higgs boson properties at $\sqrt{s} = 13$ TeV with up to 139 fb^{-1} of pp collision data [23]. The $H\to Z\gamma$ decays, the $H\to b\bar{b}$ decays with highly boosted Higgs bosons [15], and the $H\to\tau\tau$ decays in WH and ZH production modes as well as in the $t\bar{t}H$ production mode with both τ leptons decaying hadronically are included for the first time, while the following analyses are updated to the full Run 2 data set: $H\to WW^*$ and $H\to\tau\tau$ analyses targeting both the gluon–gluon fusion (ggF) and the VBF production modes, and $H\to b\bar{b}$ in VBF and $t\bar{t}H$ production modes. The updated data set in each case corresponds to an approximately factor four increase in integrated luminosity compared to the previous ATLAS publications, allowing for a reduction of the statistical uncertainty in the combined measurements. A Higgs boson mass value of $m_H = 125.09$ GeV, corresponding to the central value of the combination of ATLAS and CMS measurements in Run 1 [24], is used for SM predictions, assuming no uncertainty on the Higgs boson mass. Similar measurements [25–35], as well as their combination [36], have been reported by the CMS Collaboration.

Most of the input analyses, namely $H\to\gamma\gamma$, $H\to ZZ^*\to 4\ell$, $H\to WW^*$, $H\to\tau\tau$ and $H\to b\bar{b}$, measure the Higgs boson signal yields in phase-space regions (particle-level bins) based on the simplified template cross-section (STXS) framework [37–40]. The Stage 1.2 of STXS framework is used, allowing for measurements with an increased granularity compared to the previous results [23]. These cross sections are defined in the fiducial region $|y_H| < 2.5$, where y_H is the Higgs boson rapidity, and partitioned within each Higgs boson production process into multiple kinematic regions based on the transverse momentum of the Higgs boson, the number of associated jets and their kinematics, and the transverse momentum of associated W or Z bosons.

In search for physics beyond the SM (BSM), potential deviations of combined Higgs boson production and decay rate measurements from SM predictions are interpreted within the context of three frameworks: a framework of coupling modifiers κ applied to the SM values of Higgs boson couplings [41]; a SM

[1] Throughout the note ℓ denotes the light charged leptons e and μ.

Effective Field Theory (SMEFT) framework [42], describing the SM as a low-energy manifestation of a more complete BSM theory by means of additional higher-dimensional operators which modify the tensor structure of Higgs boson couplings; and several benchmark scenarios within the Two Higgs Doublet Model (2HDM) [41, 43–45] as an example of a UV-complete theory. Previous results of such interpretations can be found in Ref. [23, 46].

The note is structured as follows. Section 2 describes the data used and the analyses considered in the combination. Section 3 provides a short description of the statistical procedure. The measurement of the signal strength μ, defined as the ratio of the total Higgs boson signal yield to its SM prediction, is presented in Section 4 together with the measurements of cross section times branching fraction products for the main production and decay processes within $|y_H| < 2.5$. Section 5 presents results in the STXS framework. The interpretations of the data within the κ, the SMEFT and the 2HDM frameworks are presented in Sections 6, 7 and 8, respectively. Section 9 summarises the results.

2 Input measurements for the combination

The results of this note are based on pp collision data delivered by the LHC and collected by the ATLAS experiment[2] [47–49] between 2015 and 2018 at a center-of-mass energy of 13 TeV. The uncertainty in the combined 2015–2016 integrated luminosity is 2.1%, and 1.7% in the combined 2015–2018 integrated luminosity [50], obtained using the LUCID-2 detector [51] for the primary luminosity measurements.

The analyzed decay channels, targeted production modes and integrated luminosities of the input analyses entering a given combined measurement are shown in Table 1. The details can be found in the individual analysis references. The overlap between the events selected by each analysis included in the combination is found to be negligible.

All input analyses use a consistent set of event generators for the Higgs boson Monte Carlo (MC) samples, as described in the individual analysis references. The corresponding production cross sections as well as the branching fractions used for each Higgs boson decay mode are based on the higher-order state-of-the-art theoretical calculations [37]. The particle-level Higgs boson events were passed through the GEANT 4 [52] simulation of the ATLAS detector [53] and reconstructed using the same analysis software as used for the data. Event pileup is included in the simulation by overlaying inelastic pp collisions, such that the average number of interactions per bunch crossing reproduces that observed in the data. The inelastic pp collisions were simulated with PYTHIA8 using the MSTW2008LO [54] set of PDFs with the A2 [55] set of tuned parameters or using the NNPDF2.3LO set of PDFs with the A3 [56] set of tuned parameters. While the $H \to ZZ^*$, $H \to \gamma\gamma$, $H \to \mu\mu$, $H \to inv$ and $t\bar{t}H$ multilepton input measurements are the same as for the previous round of combination results, the $H \to Z\gamma$ decays, the $H \to b\bar{b}$ decays from highly boosted Higgs bosons produced in association with a vector boson, as well as the $H \to \tau\tau$ decays in WH, ZH and $t\bar{t}H(\tau_{had}\tau_{had})$ production modes are included in the combination for the first time. In addition, the measurements in the $H \to b\bar{b}$ decay channel targeting the VBF and $t\bar{t}H$ production modes as well as the measurements in the $H \to WW^*$ and $H \to \tau\tau$ channels targeting both the ggF and VBF production modes are updated with the full Run 2 data set. Besides the increased amount of data, updated analyses introduce

[2] ATLAS uses a right-handed coordinate system with its origin at the nominal interaction point (IP) in the center of the detector and the z-axis along the beam pipe. The x-axis points from the IP to the center of the LHC ring, and the y-axis points upwards. Cylindrical coordinates (r, ϕ) are used in the transverse plane, ϕ being the azimuthal angle around the z-axis. The pseudorapidity is defined in terms of the polar angle θ as $\eta = -\ln\tan(\theta/2)$. Angular distance is measured in units of $\Delta R \equiv \sqrt{(\Delta\eta)^2 + (\Delta\phi)^2}$.

Table 1: The decay channels, targeted production modes and integrated luminosity ($\mathcal{L}$) used for each input analysis of the combination. The references for the input analyses and information about which combined measurements they enter are also provided. The $t\bar{t}H(4\ell)$ and $t\bar{t}H(\tau_{\text{had}}\tau_{\text{had}})$ input analyses are complementary to the multilepton $t\bar{t}H$ analysis in Ref. [19], with no overlapping event selection criteria.

Decay channel	Target Production Modes	$\mathcal{L}$ [fb^{-1}]	Ref.	Used in combined measurement
$H \to \gamma\gamma$	ggF, VBF, $WH, ZH, t\bar{t}H, tH$	139	[10]	Everywhere
$H \to ZZ^*$	ggF, VBF, $WH, ZH, t\bar{t}H(4\ell)$	139	[11]	Everywhere
	$t\bar{t}H$	36.1	[19]	Everywhere but STXS and SMEFT
$H \to WW^*$	ggF, VBF	139	[12]	Everywhere
	$t\bar{t}H$	36.1	[19]	Everywhere but STXS and SMEFT
$H \to \tau\tau$	ggF, VBF, $WH, ZH, t\bar{t}H(\tau_{\text{had}}\tau_{\text{had}})$	139	[13]	Everywhere
	$t\bar{t}H$	36.1	[19]	Everywhere but STXS and SMEFT
$H \to b\bar{b}$	WH, ZH	139	[14–16]	Everywhere
	VBF	126	[17]	Everywhere
	$t\bar{t}H$	139	[18]	Everywhere
$H \to \mu\mu$	ggF, VBF, $VH, t\bar{t}H$	139	[20]	Everywhere but STXS and SMEFT
$H \to Z\gamma$	ggF, VBF, $VH, t\bar{t}H$	139	[21]	Everywhere but STXS and SMEFT
$H \to inv$	VBF	139	[22]	Sec. 6.3 & 6.5

various measurement improvements. Most notably, the selection and categorisation of the reconstructed events in these analyses is generally refined to allow for the measurements of Higgs boson signal yields in highly-granular phase-space regions of the Stage 1.2 STXS framework. The $H \to WW^*$ analysis introduces a measurement of the ggF production mode in the final state with two or more reconstructed jets. In the $H \to \tau\tau$ analysis, the treatment of ggF events with large Higgs boson momentum is refined, the selection of VBF events is improved by multivariate techniques and two new categories of reconstructed events targeting the $t\bar{t}H$ and VH production modes are added based on the kinematic properties and tagged flavour of the jets in the event. The $t\bar{t}H$, $H \to b\bar{b}$ cross section is now measured as a function of the Higgs boson transverse momentum. The VBF, $H \to b\bar{b}$ analysis introduces an improved separation of signal and background processes and dedicated control regions in data for the estimates of dominant background contributions.

Among all the input analyses, $H \to inv$ is considered only in a subset of the interpretation results that are presented in Section 6, i.e. only for the scenarios in which BSM contributions lead a $H \to inv$ signature. The remaining ones are included in every set of results except for the $t\bar{t}H$ multilepton, $H \to \mu\mu$ and $H \to Z\gamma$ analyses which are excluded from the STXS measurements (Section 5) and from the interpretation within the SMEFT framework (Section 7), due to their lack of sensitivity in highly granular STXS kinematic regions.

3 Statistical model

The statistical methods used in this note follow those of Ref. [9]. The results of the combination are obtained from a likelihood function defined as the product of the likelihoods of each input analysis. These are themselves products of likelihoods computed in mutually exclusive regions selected in the analysis, referred to as analysis categories.

The number of signal events in each analysis category k is expressed as

$$n_k^{\text{signal}} = \mathcal{L}_k \sum_i \sum_f (\sigma \times B)_{if} \, (A \times \epsilon)_{if}^k \tag{1}$$

where the sum runs over production modes i (i = ggF, VBF, WH, ZH, $t\bar{t}H$, ...) or the partitioned STXS bins as described in Section 5.1, and decay final states f ($f = \gamma\gamma, ZZ^*, WW^*, \tau\tau, b\bar{b}, \mu\mu, \ldots$), $\mathcal{L}_k$ is the integrated luminosity of the data set used in category k, and $(A \times \epsilon)_{if}^k$ is the acceptance times efficiency factor in category k for production mode i and final state f. The cross section times branching fraction $(\sigma \times B)_{if}$ for each relevant pair (i, f) are the parameters of interest of the model. The measurements presented in this note are obtained from fits in which $(\sigma \times B)_{if}$ are free parameters (Section 4.3), or in which they are re-expressed in terms of smaller sets of parameters: of a single signal-strength parameter μ (Section 4.1), of the cross sections σ_i in each of the main production modes (Section 4.2), of ratios of cross sections and branching fractions (Sections 4.4 and Section 5.2), of coupling modifiers (Section 6), or of parameters of the SMEFT (Sections 7) and the UV-complete BSM models (Section 8). Additional parameters, referred to as nuisance parameters, are used to describe systematic uncertainties and background quantities that are constrained by sidebands or control regions in data. The estimates of those nuisance parameters related to systematic uncertainties are modeled with distributions that correspond to auxiliary measurements (e.g. Gaussian), and relevant terms are included in the likelihood function.

Systematic uncertainties that affect multiple analyses are modeled with common nuisance parameters to propagate the effects of these uncertainties coherently to all measurements. The assessment of the associated uncertainties varies between data samples, reconstruction algorithms and software releases, leading to differences between analyses performed using the full Run 2 data set and those using 2015 and 2016 data only. Between these two sets of analyses, components of systematic uncertainties in the luminosity, the electron/photon resolution and energy scale, and in the electron reconstruction and identification efficiencies are treated as correlated. Uncertainties due to the limited number of simulated events used to estimate expected signal and background yields are included using the simplified version of the Beeston–Barlow technique [57] implemented in the HistFactory tool [58]. They are counted among the systematic uncertainties.

Theory uncertainties in the signal, such as missing higher-order QCD corrections and PDF-induced uncertainties, affect the expected signal yields of each production and decay process, as well as the signal acceptance in each category. These uncertainties are modeled by a common set of nuisance parameters[3] in most channels. For the signal-strength (Section 4.1) and coupling modifier (Section 6) results and constraints on new phenomena (Sections 7 and 8), which rely on the comparison of measured and SM-expected yields, both the acceptance and signal yield uncertainties are included. For the cross-section and branching fraction results from Sections 4.2 through 5, only acceptance uncertainties are considered.

Compared to individual input measurements, systematic theory uncertainties associated with the signal predictions in STXS bins have been updated for the combination to closely follow the granularity of the Stage 1.2 binning scheme (see Section 5). The QCD scale uncertainties in ggF are updated for all input channels which are sensitive to the ggF production mode (i.e. $H \to \gamma\gamma$, $H \to ZZ^*$,$H \to WW^*$, $H \to \tau\tau$ channels and in the VBF $H \to b\bar{b}$ analysis where the ggF contribution is sizable). Out of 18 uncertainty sources in total, two uncertainty sources account for overall fixed-order and resummation effects, two cover the migrations between different jet multiplicity bins, seven sources are introduced for the modeling of the Higgs boson transverse momentum (p_T^H) in different phase-space regions, four account for the uncertainty

[3] For higher-order QCD corrections, they are common within a given production mode.

on the distribution of the di-jet invariant mass (m_{jj}) variable, one covers the modeling of the Higgs boson plus two leading jets transverse momentum (p_T^{Hjj}) distribution in the ≥2-jet region, one the modeling of the Higgs boson plus one jet transverse momentum ($p_T^H j$) over p_T^H distribution in the high-p_T^H region, and finally, one source takes into account the uncertainty from the choice of the top quark mass scheme.

For all presented results, the effects of correlations between the uncertainties on the Higgs boson branching fractions are modeled using the correlation model specified in Ref. [37]. Possible modifications in the correlation scheme due to BSM contributions are considered negligible for the observed small deviations from the SM predictions. Uncertainties due to dependencies on SM parameter values and missing higher-order effects are included for the partial decay widths and propagated to the branching fractions and are correlated among all decay channels. The uncertainties due to modeling of background processes are typically treated as uncorrelated between analyses.

The measurement of the parameters of interest is carried out using a statistical test based on the profile likelihood ratio [59],

$$\Lambda(\boldsymbol{\alpha}) = \frac{L(\boldsymbol{\alpha}, \hat{\hat{\boldsymbol{\theta}}}(\boldsymbol{\alpha}))}{L(\hat{\boldsymbol{\alpha}}, \hat{\boldsymbol{\theta}})} ,$$

where $\boldsymbol{\alpha}$ and $\boldsymbol{\theta}$ are respectively the parameters of interest and the nuisance parameters. In the numerator, the nuisance parameters are set to their profiled values $\hat{\hat{\boldsymbol{\theta}}}(\boldsymbol{\alpha})$, which maximise the likelihood function for fixed values of the parameters of interest $\boldsymbol{\alpha}$. In the denominator, both the parameters of interest and the nuisance parameters are set to the values $\hat{\boldsymbol{\alpha}}$ and $\hat{\boldsymbol{\theta}}$ respectively which jointly maximise the likelihood.

In the asymptotic regime, in which the likelihood is approximately Gaussian, the value of $-2\ln\Lambda(\boldsymbol{\alpha})$ follows a χ^2 distribution with a number of degrees of freedom n equal to the dimensionality of the vector $\boldsymbol{\alpha}$ [59]. This property is assumed to hold for all the results presented in the following sections. Confidence intervals for a confidence level (CL) $1-p$ are then defined as the regions with values of $-2\ln\Lambda(\boldsymbol{\alpha})$ below a threshold $F^{-1}_{\chi^2_n}(1-p)$, where $F^{-1}_{\chi^2_n}$ is the quantile function of the χ^2 distribution with n degrees of freedom. The $\mathrm{CL_s}$ prescription [60] is applied when setting an upper limit on a single parameter directly related to measured event rates, for instance a production cross section.

For relevant parameters of interest, a physical bound on the parameter values is included in the statistical interpretation. For example, branching fraction parameters cannot conceptually be smaller than zero. The 95% confidence interval quoted for such parameters is then based on the profile likelihood ratio restricted to the allowed region of parameter space, using the $\tilde{t}_\mu$ test statistic of Ref. [59].

Total uncertainties in the measurement parameters are in some cases broken down into separate components for theory uncertainties affecting the background processes, theory uncertainties affecting the Higgs boson signal production, experimental uncertainties including MC statistical uncertainties, and statistical uncertainties. Each uncertainty component is derived by fixing the associated nuisance parameters to their best-fit values $\hat{\theta}$ in both the numerator and denominator of Λ, and computing again the uncertainty in the measurement parameters. This is done for each component in turn, following the order in which they are listed above. The uncertainty obtained at each step is then subtracted in quadrature from the uncertainty obtained in the previous step (in the first step, from the total uncertainty) to obtain the corresponding uncertainty component. The statistical uncertainty component is obtained in the last step, with all nuisance parameters fixed except for the ones that are solely constrained by data, such as parameters used to describe data-driven background estimates.

The level of compatibility with the Standard Model is quantified using the test statistic

$$\lambda_{\mathrm{SM}} = -2 \ln \Lambda(\boldsymbol{\alpha} = \boldsymbol{\alpha}_{\mathrm{SM}}),$$

where $\boldsymbol{\alpha}_{\mathrm{SM}}$ are the Standard Model values of the parameters of interest. A p-value[4] p_{SM} is computed in the asymptotic approximation as $p_{\mathrm{SM}} = 1 - F_{\chi^2_n}(\lambda_{\mathrm{SM}})$, with n equal to the number of free parameters of interest. For the cross-section and branching fraction measurements reported in this note, this definition does not account for the uncertainties in the SM values used as reference and may therefore lead to an underestimate of the p-value.

Results for expected significances and limits are obtained using the Asimov data set technique [59]. The Asimov data sets are defined by setting the signal yields to the values predicted by the SM, while setting the nuisance parameters to the values obtained from the fit to data with the signal yields left free-floating in the fit.

The correlation coefficients presented in this note are constructed to be symmetric around the observed best-fit values of the parameters of interest using the second derivatives of the negative log-likelihood ratio. Hence, the correlation matrices shown are not fully representative of the observed uncertainties that may be asymmetric. While the reported information is sufficient to reinterpret the measurements in terms of other parameterisations of the parameters of interest, this provides only an approximation to the information contained in the full likelihood function. For this reason, results for a number of commonly used parameterisations are also provided in Sections 4 to 6.

4 Combined measurements of signal strength, production cross sections and branching ratios

4.1 Global signal strength

The global signal strength μ is determined following the procedures used for the measurements performed at $\sqrt{s} = 7$ and 8 TeV [9]. For a specific production mode i and decay final state f, the signal yield is expressed in terms of a single modifier μ_{if}, as the production cross section σ_i and the branching fraction B_f cannot be separately measured without further assumptions. The modifiers are defined as the ratios of the measured Higgs boson yields and their SM expectations, denoted by the superscript 'SM',

$$\mu_{if} = \frac{\sigma_i}{\sigma_i^{\mathrm{SM}}} \times \frac{B_f}{B_f^{\mathrm{SM}}}. \tag{2}$$

The SM expectation by definition corresponds to $\mu_{if} = 1$. The uncertainties on the SM predictions are included as nuisance parameters in the measurement of the signal strength modifiers, following the methodology introduced in Section 3, where the procedures to decompose the uncertainties are also described.

In the model used in this section, all the μ_{if} are set to a global signal strength μ, describing a common scaling of the expected Higgs boson yield in all categories. Its measured value in the region $|y_H| < 2.5$ of the Higgs boson rapidity y_H is

[4] The p-value is defined as the probability to obtain a value of the test statistic that is at least as high as the observed value under the hypothesis that is being tested.

$$\mu = 1.06 \pm 0.06 \ = 1.06 \pm 0.03\,(\text{stat.}) \ \pm 0.03\,(\text{exp.}) \ \pm 0.04\,(\text{sig. th.}) \ \pm 0.02\,(\text{bkg. th.})$$

where the total uncertainty is decomposed into components for statistical uncertainties, experimental systematic uncertainties, and theory uncertainties in signal and background modeling. The signal theory component includes uncertainties due to missing higher-order perturbative QCD and electroweak corrections in the MC simulation, uncertainties in PDF and α_s values, the treatment of the underlying event, the matching between the hard-scattering process and the parton shower, choice of hadronisation models, and branching fraction uncertainties. The measurement is consistent with the SM prediction with a p-value of 35%, computed using the procedure defined in Section 3 with one degree of freedom. The value of $-2\ln\Lambda(\mu)$ as a function of μ is shown in Figure 1, for the full likelihood and the reduced ones with sets of nuisance parameters sequentially fixed to their best-fit values to obtain the components of the uncertainty, as detailed in Section 3. The total measurement uncertainty decreases by 10% compared to the previous combination [23], mainly driven by the reduction of the statistical uncertainty by 23% due to the increased amount of analysed data.

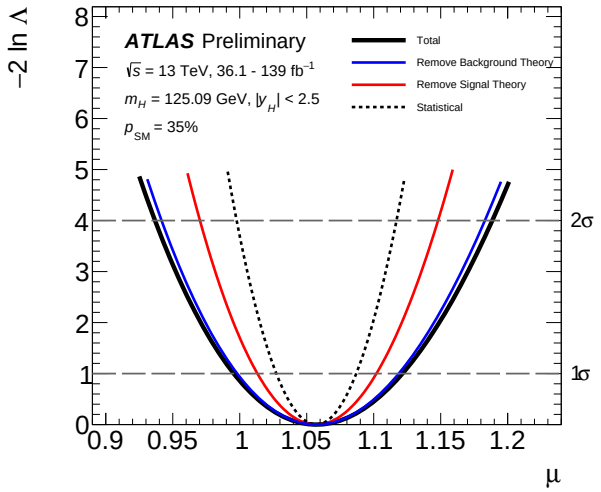

Figure 1: Observed variations of $-2\ln\Lambda(\mu)$ as a function of μ with all systematic uncertainties included (solid black line), with parameters describing theory uncertainties in background processes fixed to their best-fit values (solid blue line), with the same procedure also applied to theory uncertainties in the signal process (solid red line) and to all systematic uncertainties, so that only statistical uncertainties remain (dotted black line). The dashed horizontal lines show the 1σ and 2σ confidence intervals for μ. The level of compatibility between the measured global signal strength and the SM prediction corresponds to a p-value of 35%, computed using the procedure outlined in the text with one degree of freedom.

4.2 Production cross sections

Higgs boson production is studied in each of its main production modes. The production mechanisms considered are ggF, VBF, WH, ZH (including $gg \to ZH$), and the combination of $t\bar{t}H$ and tH ($t\bar{t}H + tH$). The small contribution from $b\bar{b}H$ (of the order of 1%) is grouped with ggF. In cases where several processes are combined, the combination assumes the relative fractions of each component to be as in

the SM within corresponding theory uncertainties. Cross sections are reported in the region $|y_H| < 2.5$. Results are obtained in a simultaneous fit to the data, with the cross sections of each production mechanism as parameters of interest. Higgs boson decay branching fractions are set to their SM values, within the uncertainties specified in Ref. [37]. The results are shown in Figure 2 and Table 2. The level of compatibility between the measurement and the SM prediction corresponds to a p-value of $p_{\text{SM}} = 63\%$, computed using the procedure outlined in Section 3 with five degrees of freedom.

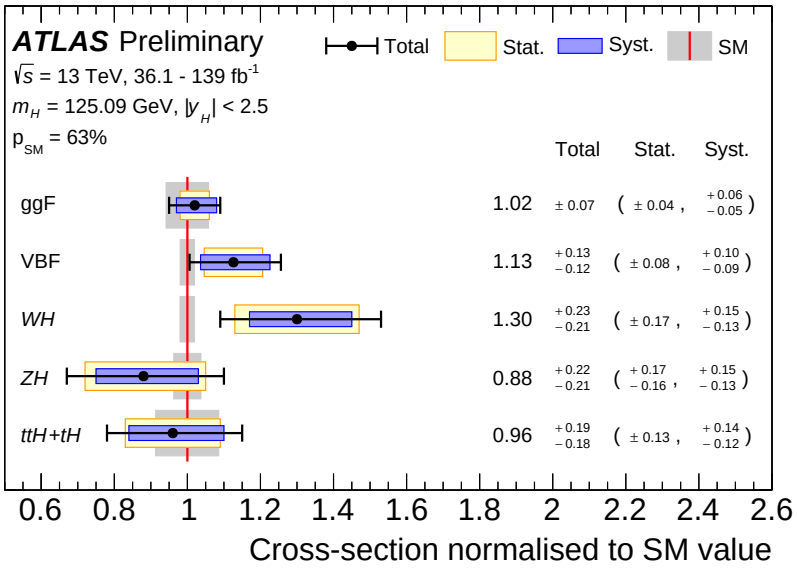

Figure 2: Cross sections for ggF, VBF, WH, ZH, and $t\bar{t}H + tH$ production modes. The cross sections are normalised to their SM predictions, measured assuming SM values for the decay branching fractions. The black error bars, blue boxes and yellow boxes show the total, systematic, and statistical uncertainties in the measurements, respectively. The gray bands indicate the theory uncertainties on the SM cross-section predictions. The level of compatibility between the measurement and the SM prediction corresponds to a p-value of $p_{\text{SM}} = 63\%$, computed using the procedure outlined in the text with five degrees of freedom.

The correlations between the measured cross sections, shown in Figure 3, are further reduced relative to previous analyses [23]. A modest correlation of -6% between the ggF and VBF processes remains, however, because of contributions from ggF production in the VBF-enriched selections. Compared to the previous results [61], the anti-correlation between WH and ZH measurements increased by a factor of two. This is mainly due to the inclusion of the $H \to \tau\tau$ channel updated with the full Run 2 data set, that is only sensitive inclusively to the VH production. This increase in anti-correlation also explains the larger difference in the observed WH and ZH cross section values compared to the previous result.

Table 2: Best-fit values and uncertainties for the production cross sections of the Higgs boson, assuming SM values for its decay branching fractions. The total uncertainties are decomposed into components for data statistics (Stat.) and systematic uncertainties (Syst.). SM predictions are shown for the cross section of each production process. They are obtained from the inclusive cross-sections and associated uncertainties reported in Ref. [37], multiplied by an acceptance factor for the region $|y_H| < 2.5$ computed using the Higgs boson simulation samples introduced in Section 2.

Process	Observed	Uncertainty [pb]			SM prediction
($\|y_H\| < 2.5$)	[pb]	Total	Stat.	Syst.	[pb]
σ_{ggF}	45.7	$^{+3.0}_{-3.2}$	$^{+1.7}_{-1.8}$	$^{+2.2}_{-2.7}$	44.8 ± 2.6
σ_{VBF}	4.0	± 0.4	± 0.3	$^{+0.3}_{-0.4}$	3.51 ± 0.07
σ_{WH}	1.56	$^{+0.26}_{-0.27}$	$^{+0.20}_{-0.21}$	$^{+0.16}_{-0.18}$	1.203 ± 0.024
σ_{ZH}	0.70	$^{+0.16}_{-0.18}$	± 0.13	$^{+0.10}_{-0.12}$	0.795 ± 0.030
σ_{ttH+tH}	0.56	$^{+0.10}_{-0.11}$	± 0.08	$^{+0.07}_{-0.08}$	0.58 ± 0.05

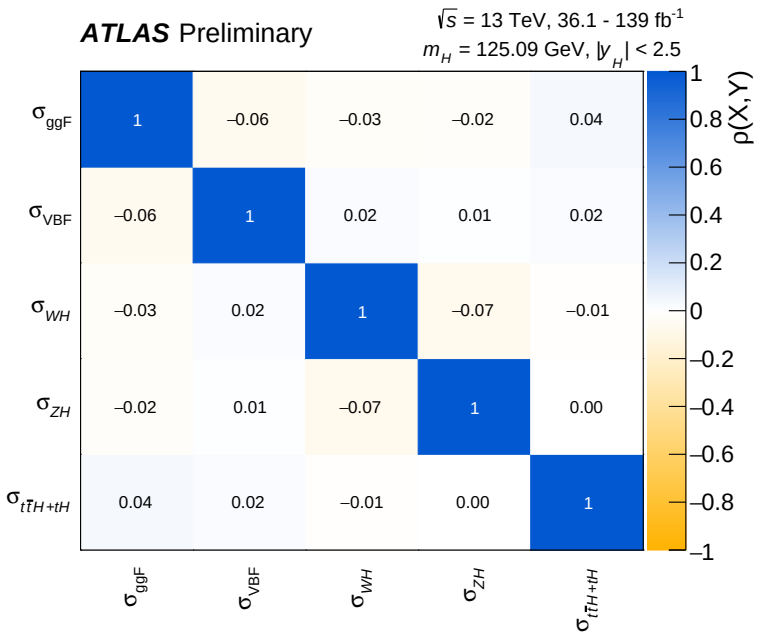

Figure 3: Correlation matrix from the measurement of production cross sections. The linear correlation coefficient $\rho(X,Y)$ between pairs of observables is indicated in color and given numerically. SM values are assumed for Higgs boson decay branching fractions.

4.3 Products of production cross sections and branching fractions

A description of both the production and decay mechanisms of the Higgs boson is obtained by considering the products $(\sigma \times B)_{if}$ of the cross section in production process i and branching fraction to final state f. The decay modes considered are $H\to\gamma\gamma$, $H \to ZZ^*$, $H \to WW^*$, $H \to \tau\tau$, $H \to b\bar{b}$, and $H \to \mu\mu$. The production processes are defined as in Section 4.2 with few exceptions. WH and ZH processes, which cannot be independently determined with the current $H\to ZZ^*\to \ell^+\ell^-\ell^+\ell^-$ and $H \to \tau\tau$ analysis due to limited data statistics, are considered together as a single VH process, with the ratio of WH to ZH cross sections fixed to its SM value within uncertainties. Similarly, ggF and VBF are grouped together in $H \to b\bar{b}$ due to the limited ggF sensitivity in decay mode, while in $H \to \mu\mu$ decay mode VBF and VH are measured together as are also ggF and $t\bar{t}H$. The results are obtained from a simultaneous fit of all input analyses, with the 21 independent $(\sigma \times B)$ products defined above as parameters of interest. They are shown in Figure 4 and Table 3. The measured VBF cross sections in the $H \to \gamma\gamma$ and, to a lower extent, in the $H \to \tau\tau$, $H \to WW^*$ and $H \to ZZ^*$ channels are smaller than those from each individual analysis due to correlations between the corresponding parameters of interest and the underlying event and parton shower theory uncertainty for the VBF production mode.

The correlation matrix of the measurements is shown in Figure 5. The largest correlations in absolute value are between the WH, $H\to\gamma\gamma$ and ZH, $H\to\gamma\gamma$ processes, between the ggF, $H \to \tau\tau$ and VBF, $H \to \tau\tau$ processes, between $t\bar{t}H$, $H \to WW^*$ and $t\bar{t}H$, $H \to \tau\tau$ processes, and between the ggF+$t\bar{t}H$, $H \to \mu\mu$ and VBF+VH, $H \to \mu\mu$ processes. In all cases, this is due to cross-contamination between these processes in the analyses providing the most sensitive measurements. Additionally, the VBF, $H \to \tau\tau$ and VBF, $H \to \gamma\gamma$ measurements are correlated due to the correlation of the corresponding systematic uncertainties from the underlying event and parton shower modeling.

The level of compatibility between the measurement and the SM prediction corresponds to a p-value of $p_{\text{SM}} = 79\%$, computed using the procedure outlined in Section 3 with 21 degrees of freedom.

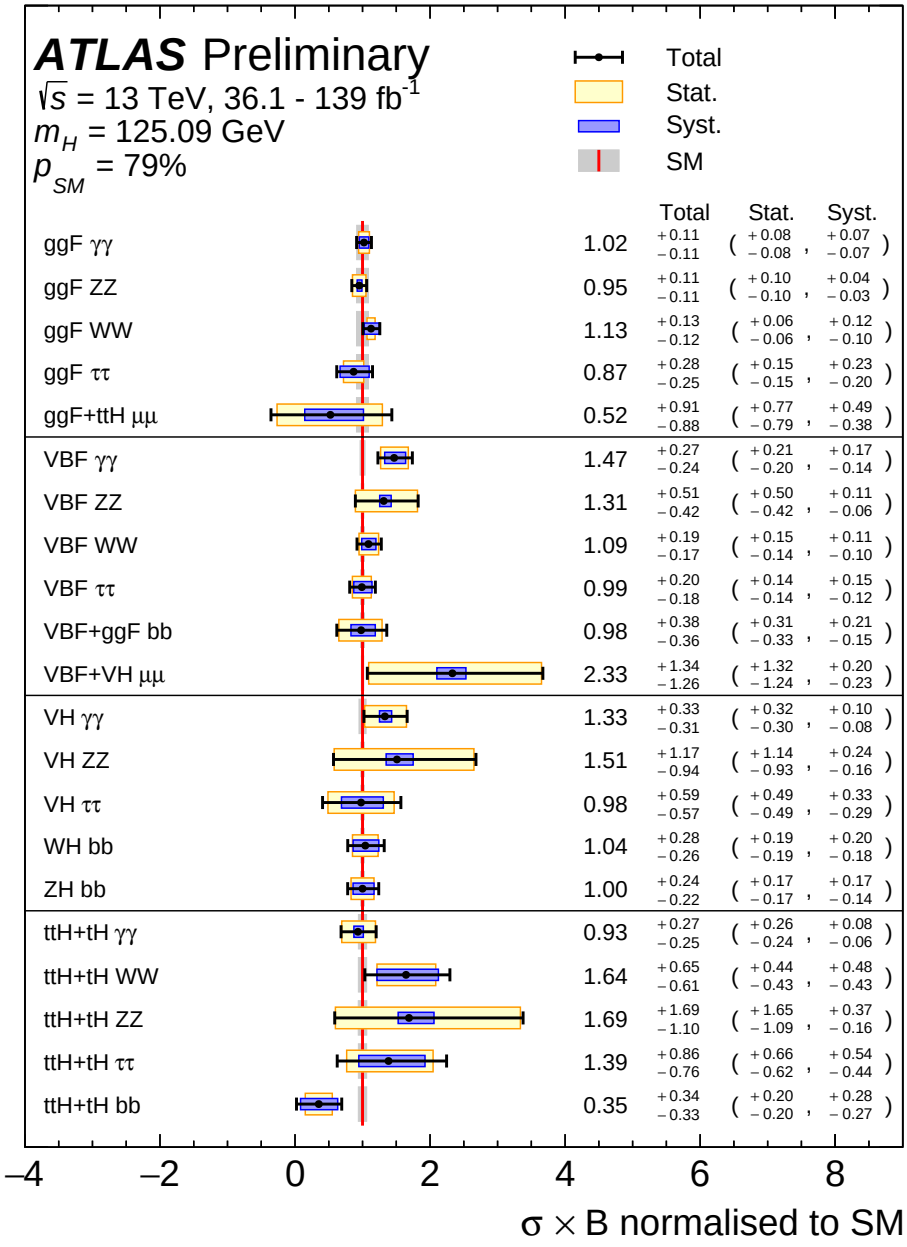

Figure 4: Cross sections times branching fraction for ggF, VBF, VH and $t\bar{t}H + tH$ production in each relevant decay mode, normalised to their SM predictions. The values are obtained from a simultaneous fit to all channels. The black error bars, blue boxes and yellow boxes show the total, systematic, and statistical uncertainties in the measurements, respectively. The gray bands show the theory uncertainties on the predictions. The level of compatibility between the measurement and the SM prediction corresponds to a p-value of $p_{\mathrm{SM}} = 79\%$, computed using the procedure outlined in the text with 21 degrees of freedom.

Table 3: Best-fit values and uncertainties for the production cross sections times branching fractions of the Higgs boson, for the combinations in which sufficient sensitivity is provided by the input analyses. Combinations not shown in the table are fixed to their SM values within uncertainties. The total uncertainties are decomposed into components for data statistics (Stat.) and systematic uncertainties (Syst.). SM predictions [37] are shown for each process.

Process	Observed	Uncertainty [fb]			SM prediction	
($\lvert y_H \rvert < 2.5$)	[fb]	Total	Stat.	Syst.	[fb]	
$\sigma^{\gamma\gamma}_{ggF}$	104	± 11	$^{+\ 8}_{-\ 9}$	± 7	102	± 6
σ^{ZZ}_{ggF}	1120	$^{+\ 120}_{-\ 130}$	± 120	$^{+\ 40}_{-\ 50}$	1180	± 70
σ^{WW}_{ggF}	10500	$^{+\ 1100}_{-\ 1200}$	± 600	$^{+\ 1000}_{-\ 1100}$	9400	± 600
$\sigma^{\tau\tau}_{ggF}$	2400	$^{+\ 700}_{-\ 800}$	± 400	± 600	2800	± 170
$\sigma^{\mu\mu}_{ggF+ttH}$	5	± 9	± 8	$^{+\ 4}_{-\ 5}$	9.8	± 0.6
$\sigma^{\gamma\gamma}_{VBF}$	11.7	$^{+\ 1.9}_{-\ 2.1}$	± 1.6	$^{+\ 1.1}_{-\ 1.4}$	7.97	$^{+\ 0.21}_{-\ 0.22}$
σ^{ZZ}_{VBF}	120	$^{+\ 40}_{-\ 50}$	$^{+\ 40}_{-\ 50}$	± 10	92.8	$^{+\ 2.3}_{-\ 2.4}$
σ^{WW}_{VBF}	820	$^{+\ 130}_{-\ 140}$	± 110	± 80	756	± 19
$\sigma^{\tau\tau}_{VBF}$	220	± 40	± 30	± 30	220	± 6
$\sigma^{bb}_{VBF+ggF}$	28000	$^{+\ 10000}_{-\ 11000}$	± 9000	$^{+\ 4000}_{-\ 6000}$	28000	± 1500
$\sigma^{\mu\mu}_{VBF+VH}$	7000	± 4000	± 4000	± 1000	3200	± 60
$\sigma^{\gamma\gamma}_{VH}$	6.0	$^{+\ 1.4}_{-\ 1.5}$	$^{+\ 1.3}_{-\ 1.4}$	$^{+\ 0.4}_{-\ 0.5}$	4.53	$^{+\ 0.13}_{-\ 0.14}$
σ^{ZZ}_{VH}	80	$^{+\ 50}_{-\ 60}$	$^{+\ 50}_{-\ 60}$	± 10	52.8	± 1.5
$\sigma^{\tau\tau}_{VH}$	120	± 70	± 60	± 40	125	± 4
σ^{bb}_{WH}	730	$^{+\ 180}_{-\ 190}$	± 130	$^{+\ 130}_{-\ 140}$	699	± 14
σ^{bb}_{ZH}	460	$^{+\ 100}_{-\ 110}$	± 80	$^{+\ 60}_{-\ 80}$	462	± 17
$\sigma^{\gamma\gamma}_{ttH+tH}$	1.24	$^{+\ 0.33}_{-\ 0.36}$	$^{+\ 0.32}_{-\ 0.35}$	$^{+\ 0.08}_{-\ 0.11}$	1.33	± 0.12
σ^{WW}_{ttH+tH}	210	± 80	$^{+\ 50}_{-\ 60}$	$^{+\ 50}_{-\ 60}$	126	± 11
σ^{ZZ}_{ttH+tH}	26	$^{+\ 17}_{-\ 26}$	$^{+\ 17}_{-\ 25}$	$^{+\ 2}_{-\ 6}$	15.4	± 1.4
$\sigma^{\tau\tau}_{ttH+tH}$	51	$^{+\ 28}_{-\ 31}$	$^{+\ 23}_{-\ 24}$	$^{+\ 16}_{-\ 20}$	36.6	$^{+\ 3.2}_{-\ 3.3}$
σ^{bb}_{ttH+tH}	120	$^{+\ 110}_{-\ 120}$	± 70	$^{+\ 90}_{-\ 100}$	340	± 29

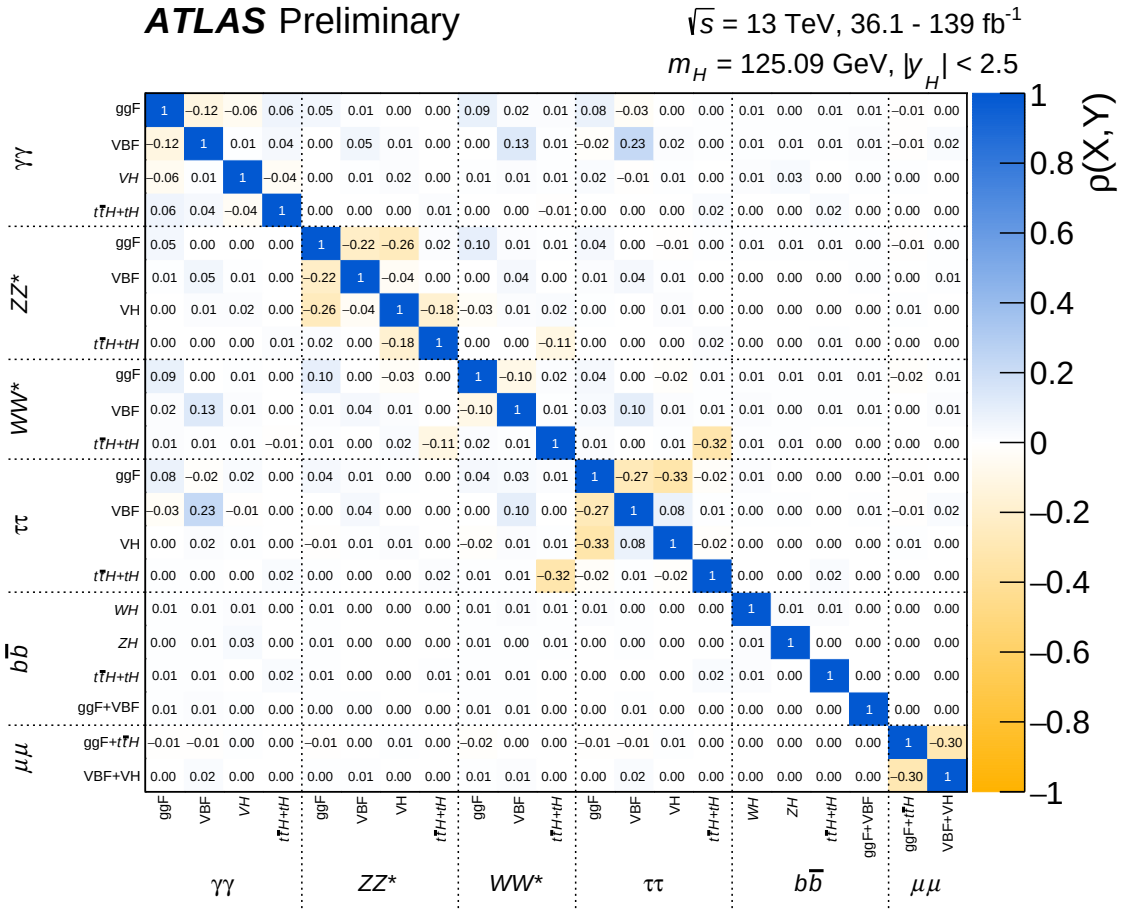

Figure 5: Correlation matrix from the measured values of the production cross sections times branching fractions of the Higgs boson, for the combinations in which sufficient sensitivity is provided by the input analyses. The linear correlation coefficient $\rho(X,Y)$ between pairs of observables is indicated in color and given numerically.

4.4 Ratios of cross sections and branching fractions

The products $(\sigma \times B)_{if}$ described in Section 4.3 can be expressed as

$$(\sigma \times B)_{if} = \sigma^{ZZ}_{\text{ggF}} \cdot \left(\frac{\sigma_i}{\sigma_{\text{ggF}}}\right) \cdot \left(\frac{B_f}{B_{ZZ}}\right),$$

in terms of the cross section times branching fraction σ^{ZZ}_{ggF} for the reference process $gg \to H \to ZZ^*$, which is precisely measured and exhibits small systematic uncertainties, ratios of production cross sections to that of ggF, $\sigma_i/\sigma_{\text{ggF}}$, and ratios of branching fractions to that of $H \to ZZ^*$, B_f/B_{ZZ}.

Results are shown in Figure 6 and Table 4. The level of compatibility between the measurements and the SM predictions corresponds to a p-value of $p_{\text{SM}} = 50\%$, computed using the procedure outlined in Section 3 with eleven degrees of freedom. Since the production and the decay rate in a given input channel cannot be disentangled, the measurements of the cross section ratios are closely interrelated to those of the

branching fraction ratios. This leads to some differences in the overall result compared to the cross section measurements in Section 4.2 where branching fractions are set to their SM values.

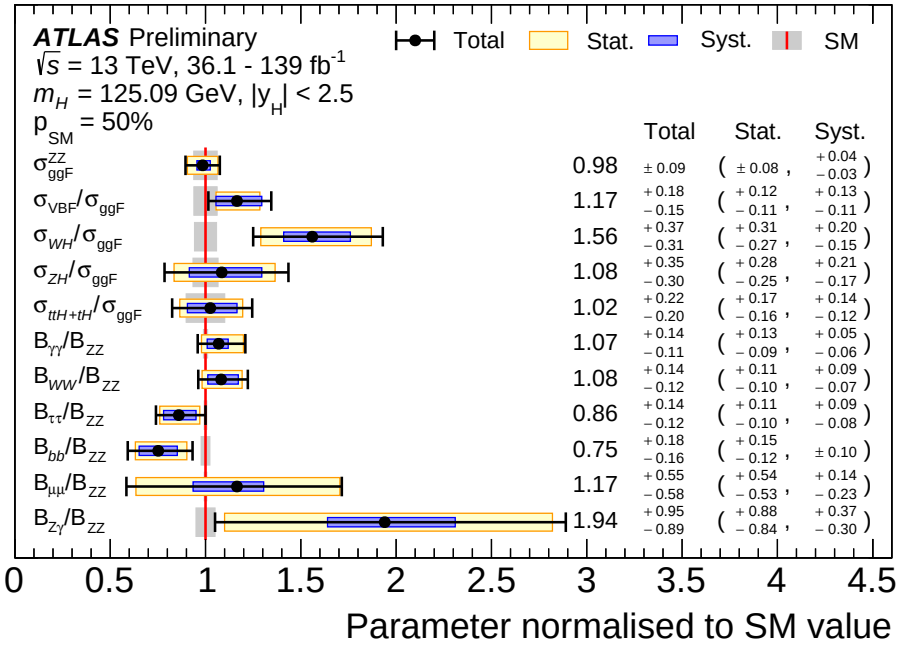

Figure 6: Results of a simultaneous fit for σ^{ZZ}_{ggF}, $\sigma_{\text{VBF}}/\sigma_{\text{ggF}}$, $\sigma_{WH}/\sigma_{\text{ggF}}$, $\sigma_{ZH}/\sigma_{\text{ggF}}$, $\sigma_{t\bar{t}H+tH}/\sigma_{\text{ggF}}$, $B_{\gamma\gamma}/B_{ZZ}$, B_{WW}/B_{ZZ}, $B_{\tau\tau}/B_{ZZ}$, and B_{bb}/B_{ZZ}. The fit results are normalised to the SM predictions. The black error bars, blue boxes and yellow boxes show the total, systematic, and statistical uncertainties in the measurements, respectively. The gray bands show the theory uncertainties on the predictions. The level of compatibility between the measurement and the SM prediction corresponds to a p-value of $p_{\text{SM}} = 50\%$, computed using the procedure outlined in the text with eleven degrees of freedom.

Table 4: Best-fit values and uncertainties for $\sigma^{ZZ}_{\mathrm{ggF}}$, together with ratios of production cross sections divided by σ_{ggF}, and ratios of branching fractions divided by B_{ZZ}. The total uncertainties are decomposed into components for data statistics (Stat.) and systematic uncertainties (Syst.). The SM predictions [37] are also shown with their total uncertainties.

Process ($\lvert y_H\rvert < 2.5$)		Observed	Uncertainty Total	Stat.	Syst.	SM prediction
σ^{ZZ}_{ggF}	[pb]	1.16	± 0.11	± 0.10	± 0.04	1.18 ± 0.07
$\sigma_{VBF}/\sigma_{ggF}$		0.091	$^{+0.012}_{-0.014}$	± 0.009	$^{+0.009}_{-0.010}$	0.079 ± 0.005
σ_{WH}/σ_{ggF}		0.042	$^{+0.008}_{-0.010}$	$^{+0.007}_{-0.008}$	$^{+0.004}_{-0.005}$	0.0269 ± 0.0016
σ_{ZH}/σ_{ggF}		0.019	$^{+0.005}_{-0.006}$	$^{+0.004}_{-0.005}$	$^{+0.003}_{-0.004}$	0.0178 ± 0.0012
$\sigma_{ttH+tH}/\sigma_{ggF}$		0.0134	$^{+0.0027}_{-0.0029}$	$^{+0.0021}_{-0.0022}$	$^{+0.0016}_{-0.0018}$	0.0131 ± 0.0013
$B_{\gamma\gamma}/B_{ZZ}$		0.092	$^{+0.010}_{-0.012}$	$^{+0.008}_{-0.011}$	$^{+0.005}_{-0.004}$	0.086 ± 0.001
B_{WW}/B_{ZZ}		8.8	$^{+1.0}_{-1.2}$	$^{+0.8}_{-0.9}$	$^{+0.6}_{-0.7}$	$8.15 \pm < 0.01$
$B_{\tau\tau}/B_{ZZ}$		2.04	$^{+0.29}_{-0.34}$	$^{+0.23}_{-0.25}$	$^{+0.19}_{-0.21}$	2.369 ± 0.017
B_{bb}/B_{ZZ}		16.5	$^{+3.5}_{-4.0}$	$^{+2.7}_{-3.4}$	± 2.2	22.0 ± 0.5
$B_{\mu\mu}/B_{ZZ}$		0.009	± 0.005	± 0.004	$^{+0.001}_{-0.002}$	$0.0082 \pm < 0.0001$
$B_{Z\gamma}/B_{ZZ}$		0.11	$^{+0.05}_{-0.06}$	± 0.05	± 0.02	0.0584 ± 0.0029

5 Combined measurements of simplified template cross sections

5.1 Simplified template cross-section framework

Simplified template cross sections [37–40] are defined through a partition of the phase space of the SM Higgs production processes into a set of non-overlapping regions. These regions are defined in terms of the kinematics of the Higgs boson and, when they are present, of associated jets and W and Z bosons, independently of the Higgs boson decay process. They are chosen according to three criteria: sensitivity to deviations from the SM expectation, avoidance of large theory uncertainties in the corresponding SM predictions, and to approximately match experimental selections so as to minimise model-dependent extrapolations. Analysis selections do not, however, necessarily correspond exactly to the STXS regions.

All regions are defined for a Higgs boson rapidity y_H satisfying $|y_H| < 2.5$, corresponding approximately to the region of experimental sensitivity. Jets are reconstructed from all stable particles with a lifetime greater than 10 ps, excluding the decay products of the Higgs boson and leptons from W and Z boson decays, using the anti-k_t algorithm with a jet radius parameter $R = 0.4$, and must have a transverse momentum $p_{\mathrm{T,jet}} > 30$ GeV.

The measurements presented in this paper use the regions of phase space specified by the Stage 1.2 splitting of the STXS framework. Higgs boson production is first classified according to the nature of the initial state and the associated particles, the latter including the decay products of the W and Z bosons if they are present. These classes are: $t\bar{t}H$ and tH processes; $qq \to Hqq$ processes, with contributions from both VBF production and quark-initiated VH production with a hadronic decay of the gauge boson; VH

production with a leptonic decay of the vector boson (V(lep)H), including $gg \to ZH$ production; and finally the ggF process. The last is considered together with $gg \to ZH$, $Z \to q\bar{q}$ production, as a single $gg \to H$ process. The contribution of the $b\bar{b}H$ production mode is taken into account as a 1% [37] increase of the $gg \to H$ yield in each STXS bin, since the acceptances for both processes are similar for all input analyses [37].

The input analyses included in this paper provide only limited sensitivity to the cross section in some bins of the Stage 1.2 scheme, mainly because of the small number of events in some regions. In other cases, they only provide sensitivity to a combination of bins, leading to strongly correlated measurements. To mitigate these effects, some of the bins as defined in Stage 1.2 have been merged for this combined analysis. These measurement bins are defined separately for the key production processes, as summarised in Figure 7, based on the jet multiplicity, the Higgs boson transverse momentum p_{T}^{H}, and in case there are at least two jets the invariant mass of the two leading jets m_{jj}. The regions for events with $p_{\mathrm{T}}^{H} \geq 200\,\mathrm{GeV}$, are defined to provide sensitivity to deviations from the SM at high momentum transfer.

The measured event yields are described by Eq. (1), with parameters of interest of the form $(\sigma \times B)_{if}$ denoting the cross section times branching fraction in STXS region i and decay channel f. The acceptance factors $(\epsilon \times A)_{if}^{k}$ for each analysis region k are determined from SM Higgs boson production processes, modeled using the samples used in the analyses, and act as templates in the fits of the STXS cross sections to the data. The dependence on the theory assumptions is less than in the measurement of the total cross sections in each production mode, since the $(\epsilon \times A)_{if}^{k}$ are computed over smaller regions. Assumptions about the kinematics within a given STXS region lead to some model-dependence, which can be reduced further by using a finer splitting of the phase space. This will be allowed by experimental precision in the future. As for the other results reported in this note, the STXS measurements assume the SM predictions for Higgs boson decays kinematics. BSM scenarios such as those described in Ref. [11] can significantly modify the acceptance of the signal, in particular for the WW^* or ZZ^* decay channels, which should be considered when using these measurements for the relevant interpretations.

Theory uncertainties for the $gg \to H$ process follow the scheme introduced in Section 2, while those for the $qq \to Hqq$, and $t\bar{t}H$ processes are defined as in Ref. [10, 11], and those of the V(lep)H process follow the scheme described in Ref. [62]. For the measurement bins defined by merging several bins of the STXS Stage-1.2 framework, the $(\epsilon \times A)$ factors are determined assuming that the relative fractions of each Stage-1.2 bin are given by their SM values, and the uncertainties predicted by the SM in these fractions are taken into account.

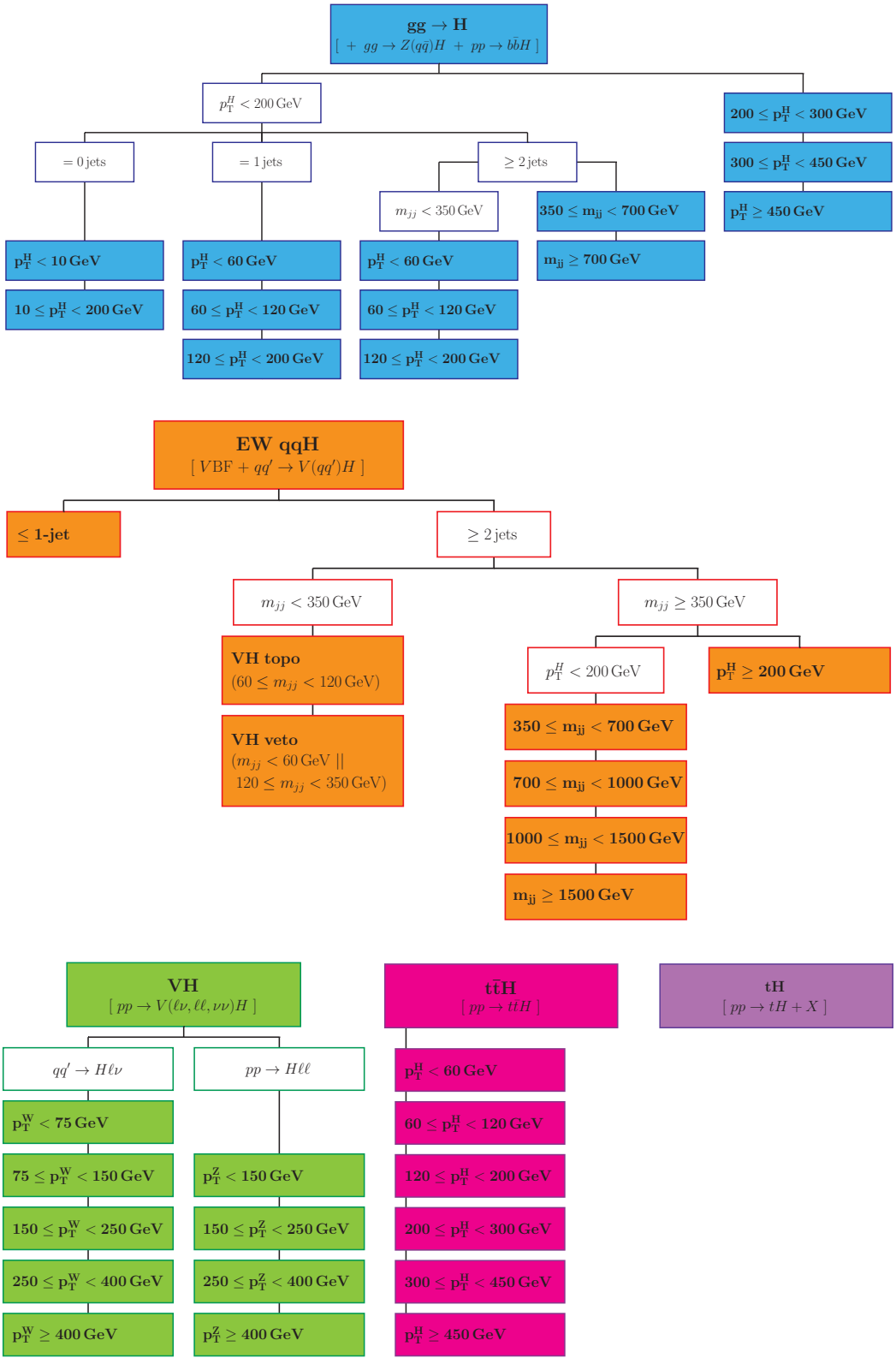

Figure 7: Definition of the STXS measurement regions used in this note. The top level box of a given color indicates the targeted production mode, the final STXS measurement regions for this mode are indicated by lower level colored boxes, while the clear boxes indicate the intermediate selection criteria.

5.2 Results

The fit parameters chosen for the combined STXS measurements are the cross sections for Higgs boson production in STXS region i times the branching fraction for the $H \to ZZ^*$ decay, $(\sigma \times B)_{i,ZZ}$, and the ratios of branching fractions B_f / B_{ZZ} for the other final states f. Similarly to the ratio model in Section 4.4, the cross sections times branching fractions for final states other than ZZ are parameterised as

$$(\sigma \times B)_{if} = (\sigma \times B)_{i,ZZ} \cdot \left(\frac{B_f}{B_{ZZ}} \right).$$

The results are shown in Figure 8 and Table 5. The observed (expected) significance for the tH STXS cross section bin is measured to be 1.0σ (0.4σ) relative to the hypothesis in which this production process is absent. The corresponding observed (expected) upper limit at 95% CL is 9.3 (6.7) times the SM prediction. The observed limit is 10% higher than the previous combined result due to the larger observed best-fit value of the measurement.

The results are in agreement with the SM predictions within uncertainties in a wide range of kinematic regions for the different Higgs boson production processes. The level of compatibility between the measurement and the SM prediction corresponds to a p-value of $p_{\text{SM}} = 92\%$, computed using the procedure outlined in Section 3 with 41 degrees of freedom.

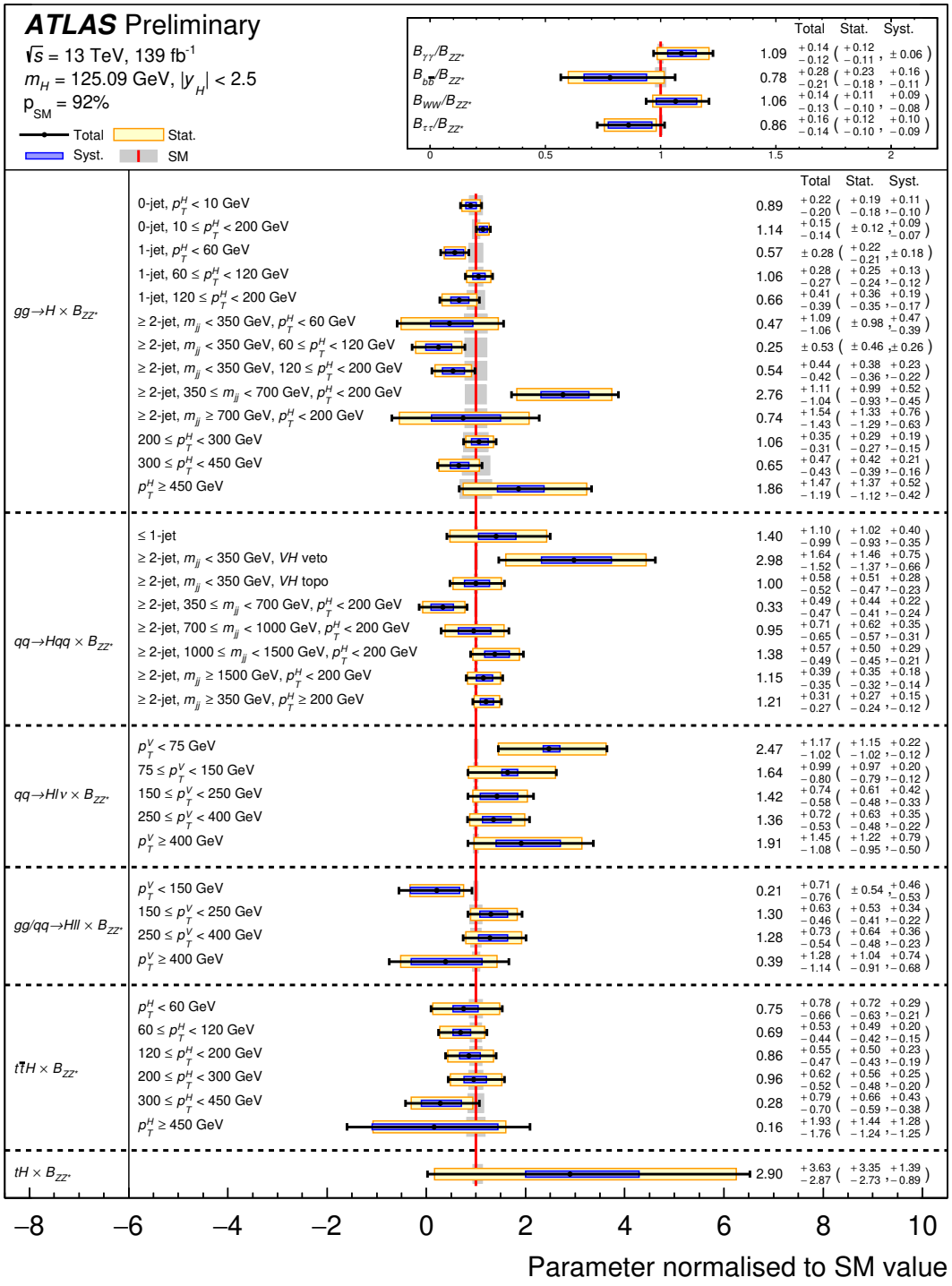

Figure 8: Best-fit values and uncertainties for the cross sections in each measurement region and of the ratios of branching fractions B_f/B_{ZZ}, normalised to the SM predictions for the various parameters. The parameters directly extracted from the fit are the products $(\sigma_i \times B_{ZZ})$ and the ratios B_f/B_{ZZ}. The black error bars, blue boxes and yellow boxes show the total, systematic, and statistical uncertainties in the measurements, respectively. The gray bands show the theory uncertainties on the predictions. The level of compatibility between the combined measurement and the SM prediction, estimated using the procedure outlined in the text with 41 degrees of freedom, corresponds to a p-value of $p_{\mathrm{SM}} = 92\%$.

Table 5: Best-fit values and uncertainties for the cross sections in each measurement region, and of the ratios of branching fractions B_f/B_{ZZ}. The total uncertainties are decomposed into components for data statistics (Stat.) and systematic uncertainties (Syst.). The SM predictions [37] are also shown for each quantity with their total uncertainties. The parameters directly extracted from the fit are the products $(\sigma_i \times B_{ZZ})$ and the ratios B_f/B_{ZZ}; the former are shown divided by the SM value of B_{ZZ}.

Measurement region $\left((\sigma_i \times B_{ZZ})/B_{ZZ}^{\mathrm{SM}}\right)$	Observed	Uncertainty [pb]			SM prediction
	[pb]	Total	Stat.	Syst.	[pb]
$gg \to H, 0-\text{jet}, p_{\mathrm{T}}^H < 10\,\text{GeV}$	5.9	$^{+1.5}_{-1.3}$	$^{+1.3}_{-1.2}$	$^{+0.7}_{-0.6}$	6.6 ± 0.9
$gg \to H, 0-\text{jet}, 10 \le p_{\mathrm{T}}^H < 200\,\text{GeV}$	23.6	$^{+3.1}_{-2.8}$	$^{+2.5}_{-2.4}$	$^{+1.8}_{-1.5}$	20.6 ± 1.6
$gg \to H, 1-\text{jet}, p_{\mathrm{T}}^H < 60\,\text{GeV}$	3.7	± 1.8	± 1.4	± 1.2	6.5 ± 0.9
$gg \to H, 1-\text{jet}, 60 \le p_{\mathrm{T}}^H < 120\,\text{GeV}$	4.8	$^{+1.3}_{-1.2}$	± 1.1	$^{+0.6}_{-0.5}$	4.5 ± 0.6
$gg \to H, 1-\text{jet}, 120 \le p_{\mathrm{T}}^H < 200\,\text{GeV}$	0.50	$^{+0.30}_{-0.29}$	$^{+0.27}_{-0.26}$	$^{+0.15}_{-0.13}$	0.75 ± 0.13
$gg \to H, \ge 2-\text{jet}, m_{jj} < 350\,\text{GeV}, p_{\mathrm{T}}^H < 60\,\text{GeV}$	0.6	$^{+1.3}_{-1.2}$	$^{+1.2}_{-1.1}$	± 0.5	1.17 ± 0.27
$gg \to H, \ge 2-\text{jet}, m_{jj} < 350\,\text{GeV}, 60 \le p_{\mathrm{T}}^H < 120\,\text{GeV}$	0.4	± 1.0	± 0.8	± 0.5	1.8 ± 0.4
$gg \to H, \ge 2-\text{jet}, m_{jj} < 350\,\text{GeV}, 120 \le p_{\mathrm{T}}^H < 200\,\text{GeV}$	0.5	± 0.4	$^{+0.4}_{-0.3}$	± 0.2	0.94 ± 0.21
$gg \to H, \ge 2-\text{jet}, 350 \le m_{jj} < 700\,\text{GeV}, p_{\mathrm{T}}^H < 200\,\text{GeV}$	1.7	$^{+0.7}_{-0.6}$	± 0.6	± 0.3	0.61 ± 0.13
$gg \to H, \ge 2-\text{jet}, m_{jj} \ge 700\,\text{GeV}, p_{\mathrm{T}}^H < 200\,\text{GeV}$	0.2	± 0.4	$^{+0.4}_{-0.3}$	± 0.2	0.27 ± 0.06
$gg \to H, 200 \le p_{\mathrm{T}}^H < 300\,\text{GeV}$	0.49	$^{+0.16}_{-0.14}$	$^{+0.13}_{-0.12}$	$^{+0.09}_{-0.07}$	0.46 ± 0.11
$gg \to H, 300 \le p_{\mathrm{T}}^H < 450\,\text{GeV}$	0.07	± 0.05	$^{+0.05}_{-0.04}$	± 0.02	0.106 ± 0.030
$gg \to H, p_{\mathrm{T}}^H \ge 450\,\text{GeV}$	0.033	$^{+0.026}_{-0.021}$	$^{+0.025}_{-0.020}$	$^{+0.009}_{-0.008}$	0.018 ± 0.006
$qq \to Hqq, \le 1-\text{jet}$	2.9	$^{+2.3}_{-2.1}$	$^{+2.1}_{-1.9}$	$^{+0.8}_{-0.7}$	2.10 ± 0.07
$qq \to Hqq, \ge 2-\text{jet}, m_{jj} < 350\,\text{GeV}, \text{VH veto}$	2.2	$^{+1.2}_{-1.1}$	$^{+1.1}_{-1.0}$	± 0.5	0.728 ± 0.022
$qq \to Hqq, \ge 2-\text{jet}, m_{jj} < 350\,\text{GeV}, \text{VH topo}$	0.53	$^{+0.31}_{-0.28}$	$^{+0.27}_{-0.25}$	$^{+0.15}_{-0.12}$	0.528 ± 0.019
$qq \to Hqq, \ge 2-\text{jet}, 350 \le m_{jj} < 700\,\text{GeV}, p_{\mathrm{T}}^H < 200\,\text{GeV}$	0.18	$^{+0.27}_{-0.26}$	$^{+0.24}_{-0.22}$	$^{+0.12}_{-0.13}$	0.545 ± 0.016
$qq \to Hqq, \ge 2-\text{jet}, 700 \le m_{jj} < 1000\,\text{GeV}, p_{\mathrm{T}}^H < 200\,\text{GeV}$	0.25	$^{+0.19}_{-0.17}$	$^{+0.16}_{-0.15}$	$^{+0.09}_{-0.08}$	0.266 ± 0.008
$qq \to Hqq, \ge 2-\text{jet}, 1000 \le m_{jj} < 1500\,\text{GeV}, p_{\mathrm{T}}^H < 200\,\text{GeV}$	0.33	$^{+0.14}_{-0.12}$	$^{+0.12}_{-0.11}$	$^{+0.07}_{-0.05}$	0.236 ± 0.007
$qq \to Hqq, \ge 2-\text{jet}, m_{jj} \ge 1500\,\text{GeV}, p_{\mathrm{T}}^H < 200\,\text{GeV}$	0.27	$^{+0.09}_{-0.08}$	$^{+0.08}_{-0.07}$	$^{+0.04}_{-0.03}$	0.233 ± 0.008
$qq \to Hqq, \ge 2-\text{jet}, m_{jj} \ge 350\,\text{GeV}, p_{\mathrm{T}}^H \ge 200\,\text{GeV}$	0.19	$^{+0.05}_{-0.04}$	± 0.04	± 0.02	0.160 ± 0.004
$qq \to H\ell\nu, p_{\mathrm{T}}^V < 75\,\text{GeV}$	0.51	$^{+0.24}_{-0.21}$	$^{+0.24}_{-0.21}$	$^{+0.05}_{-0.02}$	0.206 ± 0.008
$qq \to H\ell\nu, 75 \le p_{\mathrm{T}}^V < 150\,\text{GeV}$	0.21	$^{+0.13}_{-0.11}$	$^{+0.13}_{-0.10}$	$^{+0.03}_{-0.02}$	0.131 ± 0.006
$qq \to H\ell\nu, 150 \le p_{\mathrm{T}}^V < 250\,\text{GeV}$	0.059	$^{+0.031}_{-0.024}$	$^{+0.025}_{-0.020}$	$^{+0.017}_{-0.014}$	$0.0416\,^{+0.0018}_{-0.0019}$
$qq \to H\ell\nu, 250 \le p_{\mathrm{T}}^V < 400\,\text{GeV}$	0.015	$^{+0.008}_{-0.006}$	$^{+0.007}_{-0.005}$	$^{+0.004}_{-0.002}$	0.0108 ± 0.0005
$qq \to H\ell\nu, p_{\mathrm{T}}^V \ge 400\,\text{GeV}$	0.005	$^{+0.004}_{-0.003}$	$^{+0.003}_{-0.002}$	$^{+0.002}_{-0.001}$	0.00245 ± 0.00013
$gg/qq \to H\ell\ell, p_{\mathrm{T}}^V < 150\,\text{GeV}$	0.04	$^{+0.14}_{-0.15}$	± 0.11	$^{+0.09}_{-0.11}$	0.197 ± 0.008
$gg/qq \to H\ell\ell, 150 \le p_{\mathrm{T}}^V < 250\,\text{GeV}$	0.042	$^{+0.020}_{-0.015}$	$^{+0.017}_{-0.013}$	$^{+0.011}_{-0.007}$	0.032 ± 0.004
$gg/qq \to H\ell\ell, 250 \le p_{\mathrm{T}}^V < 400\,\text{GeV}$	0.009	$^{+0.005}_{-0.004}$	$^{+0.005}_{-0.004}$	$^{+0.003}_{-0.002}$	0.0073 ± 0.0008
$gg/qq \to H\ell\ell, p_{\mathrm{T}}^V \ge 400\,\text{GeV}$	0.0005	$^{+0.0018}_{-0.0016}$	$^{+0.0014}_{-0.0013}$	$^{+0.0010}_{-0.0009}$	0.00139 ± 0.00008
$t\bar{t}H, p_{\mathrm{T}}^H < 60\,\text{GeV}$	0.09	$^{+0.09}_{-0.08}$	$^{+0.09}_{-0.07}$	± 0.03	0.118 ± 0.016
$t\bar{t}H, 60 \le p_{\mathrm{T}}^H < 120\,\text{GeV}$	0.12	$^{+0.09}_{-0.08}$	$^{+0.09}_{-0.08}$	$^{+0.04}_{-0.03}$	0.178 ± 0.020
$t\bar{t}H, 120 \le p_{\mathrm{T}}^H < 200\,\text{GeV}$	0.11	$^{+0.07}_{-0.06}$	$^{+0.06}_{-0.05}$	$^{+0.03}_{-0.02}$	0.126 ± 0.016
$t\bar{t}H, 200 \le p_{\mathrm{T}}^H < 300\,\text{GeV}$	0.050	$^{+0.032}_{-0.027}$	$^{+0.030}_{-0.025}$	$^{+0.013}_{-0.010}$	0.053 ± 0.008
$t\bar{t}H, 300 \le p_{\mathrm{T}}^H < 450\,\text{GeV}$	0.005	$^{+0.015}_{-0.013}$	$^{+0.013}_{-0.011}$	$^{+0.008}_{-0.007}$	0.0190 ± 0.0031
$t\bar{t}H, p_{\mathrm{T}}^H \ge 450\,\text{GeV}$	0.001	$^{+0.010}_{-0.009}$	$^{+0.008}_{-0.007}$	± 0.007	0.0054 ± 0.0009
tH	0.25	$^{+0.31}_{-0.24}$	$^{+0.28}_{-0.23}$	$^{+0.12}_{-0.08}$	$0.085\,^{+0.011}_{-0.005}$
Branching fraction ratio					
$B_{\gamma\gamma}/B_{ZZ}$	0.094	$^{+0.012}_{-0.010}$	$^{+0.010}_{-0.009}$	$^{+0.006}_{-0.005}$	0.086 ± 0.001
$B_{b\bar{b}}/B_{ZZ}$	17	$^{+6}_{-5}$	$^{+5}_{-4}$	$^{+3}_{-2}$	22.0 ± 0.5
B_{WW}/B_{ZZ}	8.7	$^{+1.2}_{-1.0}$	$^{+0.9}_{-0.8}$	± 0.7	$8.15 \pm\ < 0.01$
$B_{\tau\tau}/B_{ZZ}$	2.04	$^{+0.37}_{-0.32}$	$^{+0.28}_{-0.25}$	$^{+0.24}_{-0.21}$	2.369 ± 0.017

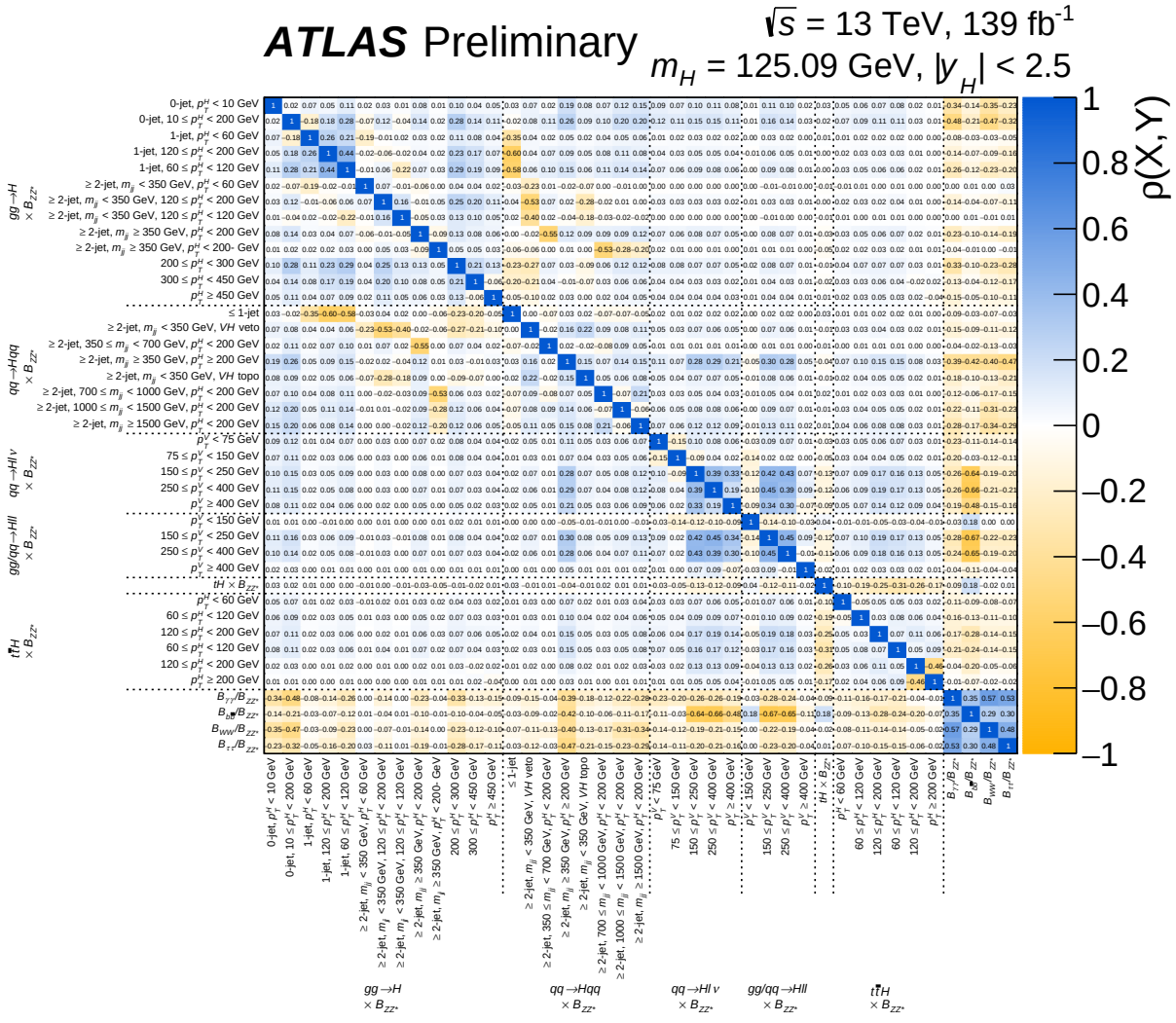

Figure 9: Correlation matrix for the measured values of the simplified template cross sections and ratios of branching fractions. The fit parameters are the products $(\sigma_i \times B_{ZZ})$ and the ratios B_f / B_{ZZ}. The linear correlation coefficient $\rho(X, Y)$ between pairs of observables is indicated in color and given numerically.

6 Interpretation of measurements in the κ framework

When testing the Higgs boson coupling strengths, the production cross sections σ_i and decay branching fractions B_f defined in Eq. (2) cannot be treated independently, as they often involve the same Higgs boson coupling strengths. Scenarios with a consistent treatment of coupling strengths in Higgs boson production and decay modes are presented in this section.

6.1 Framework for coupling-strength measurements

Coupling-strength modifiers $\boldsymbol{\kappa}$ are introduced to study modifications of the Higgs boson couplings related to BSM physics, within a framework [41] (κ-framework) based on the leading-order contributions to each production and decay process. Within the assumptions made in this framework, the Higgs boson production and decay can be factorised, such that the cross section times branching fraction of an individual channel $\sigma(i \to H \to f)$ contributing to a measured signal yield is parameterised as

$$\sigma_i \times B_f = \frac{\sigma_i(\boldsymbol{\kappa}) \times \Gamma_f(\boldsymbol{\kappa})}{\Gamma_H}, \tag{3}$$

where Γ_H is the total width of the Higgs boson and Γ_f is the partial width for Higgs boson decay into the final state f. For a given production process or decay mode j, the corresponding coupling-strength modifier κ_j is defined by

$$\kappa_j^2 = \frac{\sigma_j}{\sigma_j^{\mathrm{SM}}} \quad \text{or} \quad \kappa_j^2 = \frac{\Gamma_j}{\Gamma_j^{\mathrm{SM}}}.$$

The SM expectation, denoted by the label 'SM', by definition corresponds to $\kappa_j = 1$.

The total width of the Higgs boson is given by the sum of the partial widths for the decay modes included in the present measurements, and contributions from the following two additional classes of Higgs boson decays.

- Invisible decays: decays which are identified through an $E_{\mathrm{T}}^{\mathrm{miss}}$ signature in the analyses described in Ref. [22]. In the SM, the branching fraction of invisible decays is predicted to be 0.1%, exclusively from the $H \to ZZ^* \to 4\nu$ process. The BSM contribution to this branching fraction is denoted as $B_{\mathrm{i.}}$.
- Undetected decays: decays to which none of the analyses included in this combination are sensitive, such as decays to light quarks which have not yet been resolved, or undetected BSM particles without a sizable $E_{\mathrm{T}}^{\mathrm{miss}}$ in the final state. For the former, the SM contribution of these undetected decays is already included in Γ^{SM}, and amounts to 11%, mainly driven by the decays to gluon pairs. The BSM contribution to the undetected branching fraction is denoted as $B_{\mathrm{u.}}$. Note that deviations of the partial width of the input measurements of this analysis are separately included by scaling their partial width by κ_j.

BSM contributions to the total Higgs boson decay width may manifest themselves as a value of κ_j differing from one, or a value of $B_{\text{i.}}$ or $B_{\text{u.}}$ differing from zero. The Higgs boson total width is then expressed as $\Gamma_H(\boldsymbol{\kappa}, B_{\text{i.}}, B_{\text{u.}}) = \kappa_H^2(\boldsymbol{\kappa}, B_{\text{i.}}, B_{\text{u.}})\,\Gamma_H^{\text{SM}}$ with

$$\kappa_H^2(\boldsymbol{\kappa}, B_{\text{i.}}, B_{\text{u.}}) = \frac{\sum_j B_j^{\text{SM}} \kappa_j^2}{(1 - B_{\text{i.}} - B_{\text{u.}})}. \tag{4}$$

By definition, $B_{\text{u.}}$ is not directly constrained by any measurement, so that extracting values for both the κ parameters and $B_{\text{u.}}$ simultaneously requires additional assumptions or constraints. In fact, all the measured cross sections included in this combination would be left unchanged for certain choices of values for the κ parameters and $B_{\text{u.}}$, as the changes would divide out in the ratio, as can be seen from Eqs. (3) and (4). The simplest assumption is that there are no undetected Higgs boson decays and the invisible branching fraction is as predicted by the SM. An alternative, weaker assumption, is to require $\kappa_W \leq 1$ and $\kappa_Z \leq 1$ [41]. Another possible alternative, used in the previous combination [63] but not in the current note, is based on the measured signal strength of off-shell Higgs boson production to constrain the total Higgs width, assuming off-shell and on-shell coupling-strength scale factors are the same.

An alternative approach is to rely on measurements of ratios of coupling-strength scale factors, which can be measured without assumptions about the Higgs boson total width, since the dependence on Γ_H of each coupling strength cancels in their ratios [5].

The current LHC data are nearly insensitive to the coupling-strength modifiers κ_c and κ_s. Thus, in the following it is assumed that κ_c varies as κ_t and κ_s varies as κ_b. Other coupling modifiers (κ_u, κ_d, and κ_e) are irrelevant for the combination provided they are of order unity. The $gg \to H$, $H \to gg$, $gg \to ZH$, $H \to \gamma\gamma$, and $H \to Z\gamma$ processes are loop-induced in the SM. The ggH vertex and the $H \to \gamma\gamma$ and $H \to Z\gamma$ processes are treated either using effective scale factors κ_g, κ_γ and $\kappa_{Z\gamma}$, respectively, or expressed in terms of the more fundamental coupling-strength scale factors corresponding to the particles that contribute to the loop in the SM, including all interference effects. The $gg \to ZH$ process is never described using an effective scale factor and always resolved in terms of modifications of the SM Higgs boson couplings to the top quark and the Z boson. These relations are summarised in Table 6. All uncertainties in the best-fit values shown in the following take into account both the experimental and theoretical systematic uncertainties, following the procedures outlined in Section 3.

[5] For the validity of κ-framework the narrow-width assumption should still hold.

Table 6: Parametrisations of Higgs boson production cross sections σ_i, partial decay widths Γ^f, and the total width Γ_H, normalised to their SM values, as functions of the coupling-strength modifiers κ. The effect of invisible and undetected decays is not considered in the expression for Γ_H. For effective κ parameters associated with loop processes, the resolved scaling in terms of the modifications of the Higgs boson couplings to the fundamental SM particles is given. The coefficients are derived following the methodology in Ref. [37, 41].

Production cross section	Loops	Main interference	Effective modifier	Resolved modifier
$\sigma(\text{ggF})$	✓	t–b	κ_g^2	$1.040\,\kappa_t^2 + 0.002\,\kappa_b^2 - 0.038\,\kappa_t\kappa_b - 0.005\,\kappa_t\kappa_c$
$\sigma(\text{VBF})$	-	-	-	$0.733\,\kappa_W^2 + 0.267\,\kappa_Z^2$
$\sigma(qq/qg \to ZH)$	-	-	-	κ_Z^2
$\sigma(gg \to ZH)$	✓	t–Z	$\kappa_{(ggZH)}$	$2.456\,\kappa_Z^2 + 0.456\,\kappa_t^2 - 1.903\,\kappa_Z\kappa_t$ $- 0.011\,\kappa_Z\kappa_b + 0.003\,\kappa_t\kappa_b$
$\sigma(WH)$	-	-	-	κ_W^2
$\sigma(t\bar{t}H)$	-	-	-	κ_t^2
$\sigma(tHW)$	-	t–W	-	$2.909\,\kappa_t^2 + 2.310\,\kappa_W^2 - 4.220\,\kappa_t\kappa_W$
$\sigma(tHq)$	-	t–W	-	$2.633\,\kappa_t^2 + 3.578\,\kappa_W^2 - 5.211\,\kappa_t\kappa_W$
$\sigma(b\bar{b}H)$	-	-	-	κ_b^2
Partial decay width				
Γ^{bb}	-	-	-	κ_b^2
Γ^{WW}	-	-	-	κ_W^2
Γ^{gg}	✓	t–b	κ_g^2	$1.111\,\kappa_t^2 + 0.012\,\kappa_b^2 - 0.123\,\kappa_t\kappa_b$
$\Gamma^{\tau\tau}$	-	-	-	κ_τ^2
Γ^{ZZ}	-	-	-	κ_Z^2
Γ^{cc}	-	-	-	$\kappa_c^2\ (=\kappa_t^2)$
$\Gamma^{\gamma\gamma}$	✓	t–W	κ_γ^2	$1.589\,\kappa_W^2 + 0.072\,\kappa_t^2 - 0.674\,\kappa_W\kappa_t$ $+0.009\,\kappa_W\kappa_\tau + 0.008\,\kappa_W\kappa_b$ $-0.002\,\kappa_t\kappa_b - 0.002\,\kappa_t\kappa_\tau$
$\Gamma^{Z\gamma}$	✓	t–W	$\kappa_{(Z\gamma)}^2$	$1.118\,\kappa_W^2 - 0.125\,\kappa_W\kappa_t + 0.004\,\kappa_t^2 + 0.003\,\kappa_W\kappa_b$
Γ^{ss}	-	-	-	$\kappa_s^2\ (=\kappa_b^2)$
$\Gamma^{\mu\mu}$	-	-	-	κ_μ^2
Total width ($B_{\text{i.}} = B_{\text{u.}} = 0$)				
Γ_H	✓	-	κ_H^2	$0.581\,\kappa_b^2 + 0.215\,\kappa_W^2 + 0.082\,\kappa_g^2$ $+0.063\,\kappa_\tau^2 + 0.026\,\kappa_Z^2 + 0.029\,\kappa_c^2$ $+0.0023\,\kappa_\gamma^2 + 0.0015\,\kappa_{(Z\gamma)}^2$ $+0.0004\,\kappa_s^2 + 0.00022\,\kappa_\mu^2$

6.2 Fermion and gauge boson couplings

The model studied in this section probes the universal coupling-strength scale factors $\kappa_V = \kappa_W = \kappa_Z$ for all vector bosons and $\kappa_F = \kappa_t = \kappa_b = \kappa_\tau = \kappa_\mu$ for all fermions. The effective couplings corresponding to the ggH, $H \to \gamma\gamma$ and $H \to Z\gamma$ vertex loops are being resolved in terms of the fundamental SM couplings. It is assumed that there are no invisible or undetected Higgs boson decays, i.e. $B_{\text{i.}} = B_{\text{u.}} = 0$. Only the relative sign between κ_V and κ_F is physical. As a negative relative sign has been excluded with high confidence level [9], $\kappa_V \geq 0$ and $\kappa_F \geq 0$ are assumed. The best-fit values and uncertainties from a combined fit are

$$\kappa_V = 1.039^{+0.031}_{-0.030}$$
$$\kappa_F = 0.93 \pm 0.05.$$

Figure 10 shows the results of the combined fit in the (κ_V, κ_F) plane. Both κ_V and κ_F are measured to be compatible with the SM expectation. The level of compatibility between the SM hypothesis with the best-fit point corresponds to a p-value of $p_{\text{SM}} = 2.8\%$, computed using the procedure outlined in Section 3 with two degrees of freedom. Compared to the previous result [23], a lower p-value is observed mainly due to the lower fitted value for κ_F. This is driven by the updated $t\bar{t}H$, $H \to b\bar{b}$ and ggF, $H \to \tau\tau$ measurements. In the combined measurement a linear correlation of 43% between κ_V and κ_F is observed.

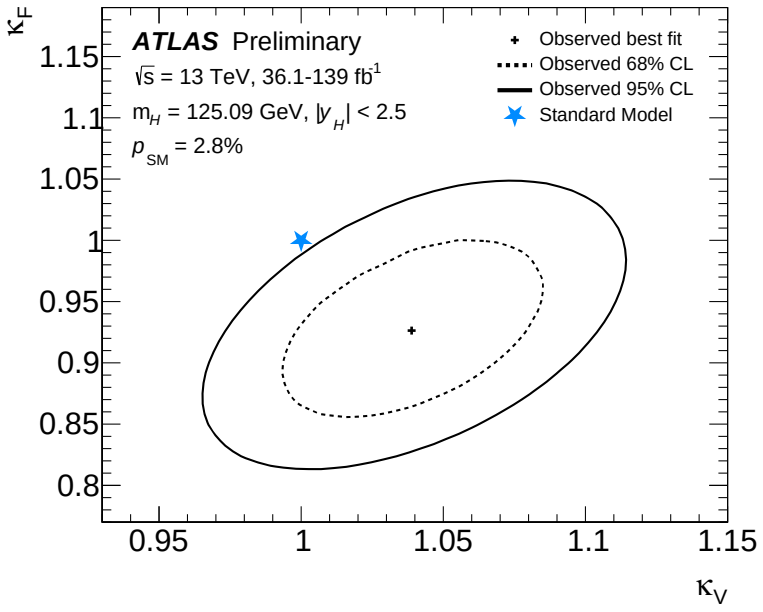

Figure 10: Negative log-likelihood contours at 68% and 95% CL in the (κ_V, κ_F) plane obtained from a combined fit, assuming no contributions from invisible or undetected Higgs boson decays. The best-fit value is indicated by a cross while the SM hypothesis is indicated by a star. A linear correlation of 43% between κ_V and κ_F is observed. The level of compatibility between the combined measurement and the SM prediction, estimated using the procedure outlined in the text with two degrees of freedom, corresponds to a p-value of $p_{\text{SM}} = 2.8\%$.

6.3 Probing BSM contributions in loops and decays

To probe contributions of new particles through loops, the effective coupling strengths to photons (κ_γ), gluons (κ_g) and to $Z\gamma$ ($\kappa_{Z\gamma}$) are measured. These parameters are defined to be positive as there is by construction no sensitivity to the sign of these coupling strengths. The modifiers corresponding to other loop-induced processes are resolved. Any potential BSM contribution to κ_γ, κ_g and $\kappa_{Z\gamma}$, corresponding to a deviation from unity, may also contribute to the total width of the Higgs boson. To check this, the branching fractions $B_{\text{i.}}$ and $B_{\text{u.}}$, defined in Section 6.1, can be fixed to zero or allowed free in the fit. Furthermore, the benchmark models studied in this section assume that all coupling-strength modifiers of known SM particles are unity, i.e. they follow the SM predictions, and that the kinematics of the Higgs boson decay products are not altered significantly.

Assuming $B_{\text{i.}} = B_{\text{u.}} = 0$, the best-fit values and uncertainties from a combined fit are

$$\begin{aligned}\kappa_g &= 1.00 \pm 0.05\\ \kappa_\gamma &= 1.06 \pm 0.05\\ \kappa_{Z\gamma} &= 1.43^{+0.31}_{-0.38}.\end{aligned}$$

The corresponding negative log-likelihood scans are shown in Figure 11. The level of compatibility between the SM hypothesis with the best-fit point corresponds to a p-value of $p_{\text{SM}} = 36\%$, computed using the procedure outlined in Section 3 with three degrees of freedom. The observed (expected) significance on $\kappa_{Z\gamma}$ relative to the absence of this coupling is 2.2σ (1.1σ).

To also consider additional contributions to the total width of the Higgs boson, the assumption of no invisible or undetected decays is dropped and $B_{\text{i.}}$ and $B_{\text{u.}}$ are included as independent parameters in the model. The measurement sensitive to Higgs boson decays into invisible final states described in Ref. [22] is included in the combination and used to constrain $B_{\text{i.}}$. The $B_{\text{u.}}$ parameter is constrained by decay modes that do not involve a loop process. The results from this model are

$$\begin{aligned}\kappa_g &= 0.98 \pm 0.06\\ \kappa_\gamma &= 1.06 \pm 0.05\\ \kappa_{Z\gamma} &= 1.43^{+0.31}_{-0.37}\\ B_{\text{i.}} &< 0.14 \text{ at } 95\% \text{ CL}\\ B_{\text{u.}} &< 0.15 \text{ at } 95\% \text{ CL}.\end{aligned}$$

Limits on $B_{\text{i.}}$ and $B_{\text{u.}}$ are set using the $\tilde{t}_\mu$ prescription presented in Section 3. The observed (expected) upper limits at 95% CL on $B_{\text{i.}}$ and $B_{\text{u.}}$ are 0.14 (0.13) and 0.15 (0.21), respectively. The level of compatibility between the SM hypothesis with the best-fit point corresponds to a p-value of $p_{\text{SM}} = 60\%$, computed using the procedure outlined in Section 3 with five degrees of freedom.

The results for both models are summarised in Figure 12.

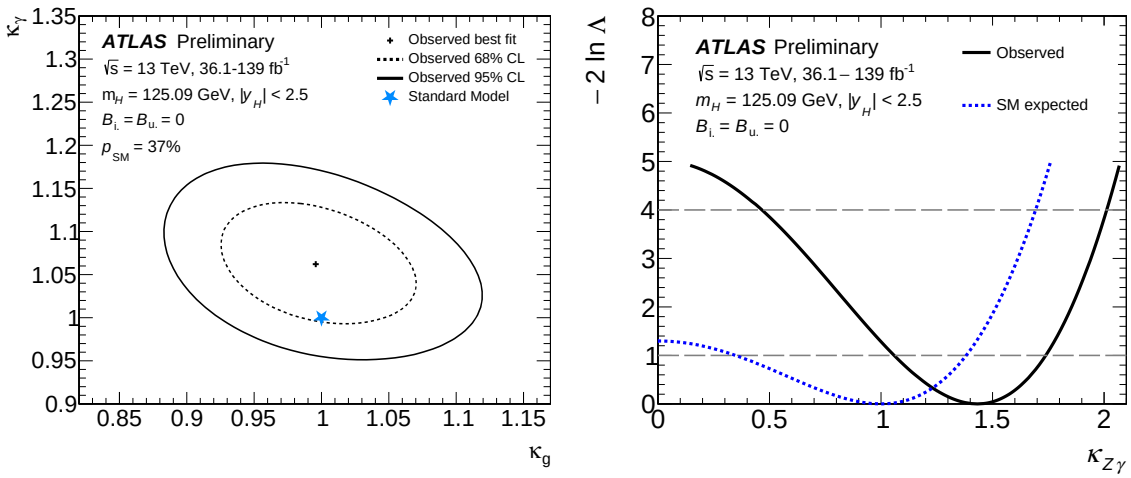

(a) (b)

Figure 11: (a) Negative log-likelihood contours at 68% and 95% CL in the $(\kappa_\gamma, \kappa_g)$ plane obtained from a combined fit and assuming no contributions from invisible or undetected Higgs boson decays. The best-fit value for each measurement is indicated by a cross while the SM hypothesis is indicated by a star. A linear correlation of −30% between κ_γ and κ_g is observed. The compatibility between the combined measurement and the SM prediction, estimated using the procedure outlined in the text with two degrees of freedom, corresponds to a p-value of $p_{SM} = 37\%$. (b) Observed (black solid) and expected (blue dashed) negative log-likelihood scans as a function of $\kappa_{Z\gamma}$ from a combined fit of the three parameters κ_g, κ_γ and $\kappa_{Z\gamma}$, assuming no contributions from invisible and undetected Higgs boson decays, $B_{\text{i.}} = B_{\text{u.}} = 0$. When scanning one parameter, other parameters of interest from the model are also varied in the maximisation procedure. The dashed horizontal lines show the levels $-2\ln\Lambda = 1$ and $-2\ln\Lambda = 4$ which are used to define, respectively, the 1σ and 2σ confidence intervals for the parameter of interest.

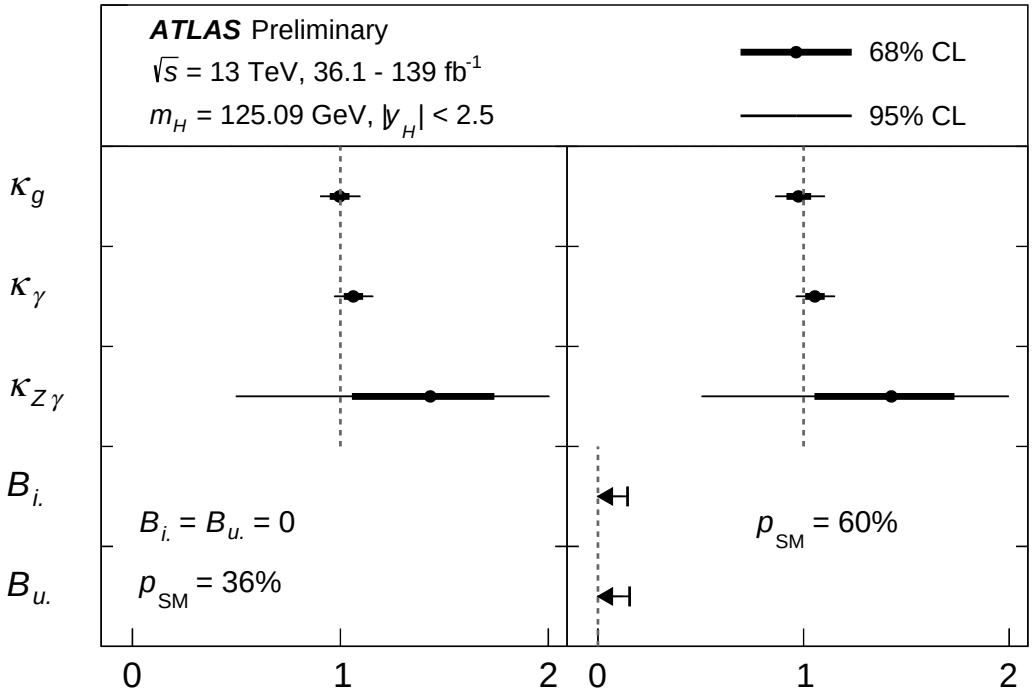

Figure 12: Best-fit values and uncertainties for effective modifiers to the gluon, photon and $Z\gamma$ couplings of the Higgs boson, with either $B_{\mathrm{i.}} = B_{\mathrm{u.}} = 0$ (left), or $B_{\mathrm{i.}}$ and $B_{\mathrm{u.}}$ included as free parameters (right). In the latter case, the measurement of the Higgs boson decay rate into invisible final states is included in the combination. For the $B_{\mathrm{i.}}$ and $B_{\mathrm{u.}}$ results, the bar with the left-facing arrow indicates an upper limit at 95% CL. The SM corresponds to $\kappa_g = \kappa_\gamma = \kappa_{Z\gamma} = 1$ and $B_{\mathrm{i.}} = B_{\mathrm{u.}} = 0$. All coupling-strength modifiers of known SM particles are assumed to be unity, i.e. they follow the SM predictions. The level of compatibility between the combined measurement and the SM prediction, estimated using the procedure outlined in the text with three (five) degrees of freedom for left (right) panel, corresponds to a p-value of $p_{\mathrm{SM}} = 36\%$ (60%).

6.4 Generic parameterisation assuming no new particles in loops and decays

In this model the scale factors for the coupling strengths to W, Z, t, b, τ and μ are treated independently. The modifiers of Higgs boson couplings to second-generation quarks are assumed to scale as the coupling modifiers for the third-generation quarks. SM values are assumed for the couplings to first-generation fermions. Furthermore, it is assumed that only SM particles contribute to Higgs boson vertices involving loops, and modifications of the coupling-strength scale factors for fermions and vector bosons are propagated through the loop calculations. Invisible or undetected Higgs boson decays are assumed not to exist. All coupling-strength scale factors are assumed to be positive. The results of the $H \to \mu\mu$ analysis are included for this specific benchmark model. The results are shown in Table 7. The updated $t\bar{t}H$, $H \to b\bar{b}$ measurement leads to a smaller observed value of κ_b compared to the previous combination result [23]. Consequently, the value of κ_μ has decreased due to the contribution of κ_b to the total Higgs boson decay width. The observed (expected) significance on κ_μ relative to the absence of this coupling is 2.1 σ (1.7 σ). The observed significance is slightly higher compared with the one reported in Ref. [20] due to other coupling strengths being profiled to the combined data set instead of fixed to SM.

Table 7: Fit results for κ_Z, κ_W, κ_b, κ_t, κ_τ and κ_μ, all assumed to be positive. In this benchmark model BSM contributions to Higgs boson decays are assumed not to exist and Higgs boson vertices involving loops are resolved in terms of their SM content.

Parameter	Result
κ_Z	0.99 ± 0.06
κ_W	1.03 ± 0.05
κ_b	0.88 ± 0.11
κ_t	0.92 ± 0.06
κ_τ	0.92 ± 0.07
κ_μ	$1.07\ ^{+\ 0.25}_{-\ 0.31}$

All measured coupling-strength scale factors in this generic model are found to be compatible with their SM expectation. The level of compatibility between the SM hypothesis with the best-fit point corresponds to a p-value of $p_{\text{SM}} = 19\%$, computed using the procedure outlined in Section 3 with six degrees of freedom. Figure 13 shows the results of this benchmark model in terms of reduced coupling-strength scale factors, defined as

$$y_V = \sqrt{\kappa_V \frac{g_V}{2v}} = \sqrt{\kappa_V}\frac{m_V}{v}$$

for weak bosons with a mass m_V, where g_V is the absolute Higgs boson coupling strength and $v = 246\,\text{GeV}$ is the vacuum expectation value of the Higgs field, and

$$y_F = \kappa_F \frac{g_F}{\sqrt{2}} = \kappa_F \frac{m_F}{v}$$

for fermions with a mass m_F. For the b quark and the top quark, the $\overline{MS}$ running mass evaluated at a scale of 125.09 GeV is used.

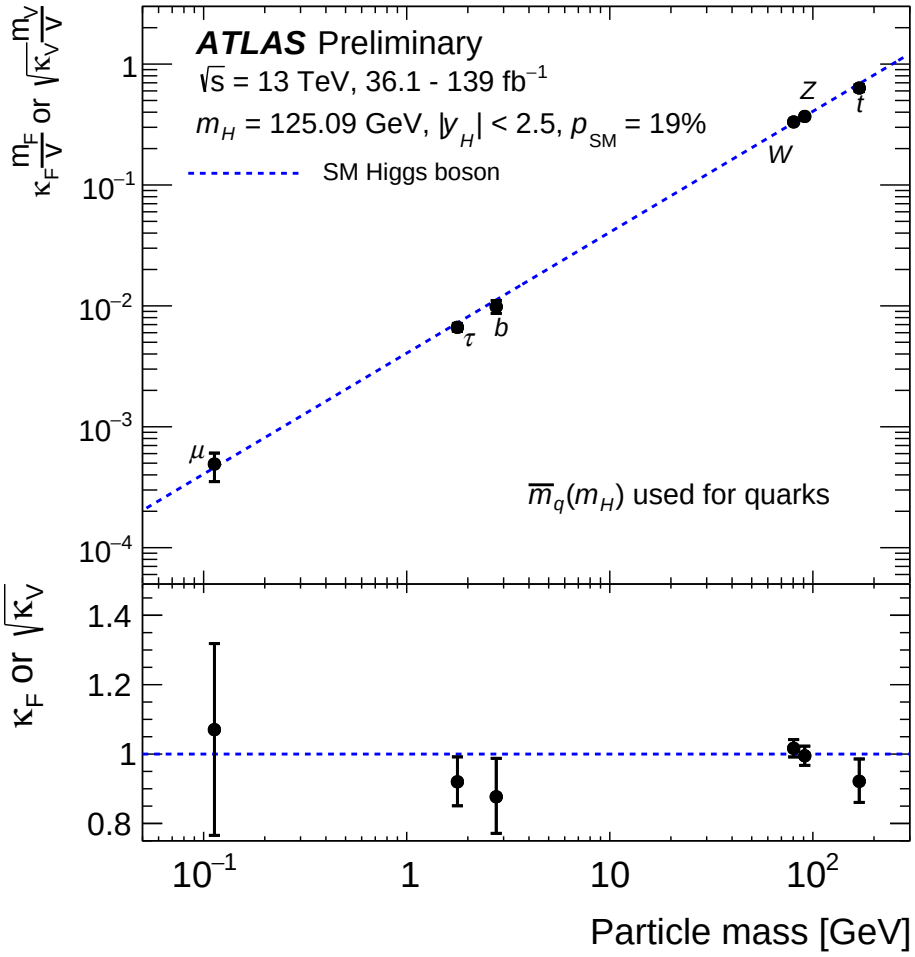

Figure 13: Reduced coupling-strength modifiers $\kappa_F \frac{m_F}{v}$ for fermions ($F = t, b, \tau, \mu$) and $\sqrt{\kappa_V}\frac{m_V}{v}$ for weak gauge bosons ($V = W, Z$) as a function of their masses m_F and m_V, respectively, and the vacuum expectation value of the Higgs field $v = 246$ GeV. The SM prediction for both cases is also shown (dashed line). The black error bars represent 68% CL intervals for the measured parameters. The coupling modifiers are measured assuming no BSM contributions to the Higgs boson decays, and the SM structure of loop processes such as ggF, $H \to \gamma\gamma$ and $H \to Z\gamma$. The lower panel shows the ratios of the values to their SM predictions. The level of compatibility between the combined measurement and the SM prediction, estimated using the procedure outlined in the text with six degrees of freedom, corresponds to a p-value of $p_{\text{SM}} = 19\%$.

6.5 Generic parameterisation including effective photon, $Z\gamma$ and gluon couplings with and without BSM contributions in decays

The models considered in this section are based on the same parameterisation as the one in Section 6.4 but the ggF, $H \to gg$, $H \to \gamma\gamma$ and $H \to Z\gamma$ loop processes are parameterised using the effective coupling-strength modifiers κ_g, κ_γ and $\kappa_{Z\gamma}$, similar to the benchmark model probed in Section 6.3.

The measured parameters include κ_Z, κ_W, κ_b, κ_t, κ_τ, κ_μ, κ_γ, $\kappa_{Z\gamma}$ and κ_g. The sign of κ_t can be either positive or negative, while κ_Z is assumed to be positive without loss of generality. All other model parameters are also assumed to be positive. Furthermore it is assumed that any potential BSM effect does not affect the kinematics of the Higgs boson decay products significantly.

Two scenarios are considered for the total width of the Higgs boson:

(a) No BSM contributions to the total width of the Higgs boson ($B_{\text{i.}} = B_{\text{u.}} = 0$).

(b) Both $B_{\text{i.}}$ and $B_{\text{u.}}$ are added as free parameters to the model. The measurement of Higgs boson decays into invisible final states, VBF, $H \to inv$, described in Ref. [22] is included in the combination and used to provide a constraint on $B_{\text{i.}}$. The conditions $\kappa_W \leq 1$ and $\kappa_Z \leq 1$ are used to provide a constraint on $B_{\text{u.}}$ as discussed in Section 6.1. $B_{\text{u.}}$ is assumed to be positive.

The numerical results for the two scenarios are summarised in Table 8 and illustrated in Figure 14. All probed fundamental coupling-strength scale factors, as well as the probed loop-induced coupling scale factors are measured to be compatible with their SM expectation.

In scenario (a) with no BSM contribution to the total width, a possible negative value for κ_t is excluded at 4.3σ (3.8σ expected) relative to the best-fit value with sensitivity coming from the tH and $gg \to ZH$ processes. The level of compatibility between the SM hypothesis with the best-fit point corresponds to a p-value of $p_{\text{SM}} = 33\%$, computed using the procedure outlined in Section 3 with nine degrees of freedom. In scenario (b) the observed (expected) 95% CL upper limits on the branching fractions are $B_{\text{i.}} < 0.09$ (0.11) and $B_{\text{u.}} < 0.16$ (0.23).

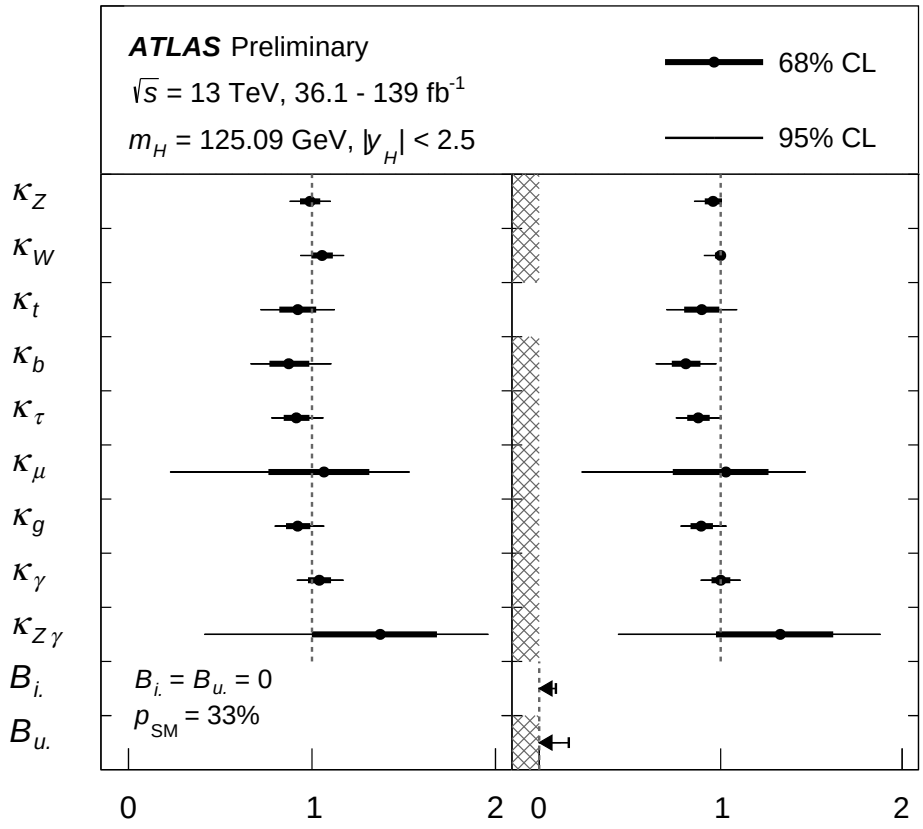

Figure 14: Best-fit values and uncertainties for Higgs boson coupling modifiers per particle type with effective photon, $Z\gamma$ and gluon couplings and either $B_{\text{i.}} = B_{\text{u.}} = 0$. (left), or $B_{\text{i.}}$ and $B_{\text{u.}}$ included as free parameters with the conditions $\kappa_{W,Z} \leq 1$ imposed and the measurement of the Higgs boson decay rate into invisible final states included in the combination (right). For the $B_{\text{i.}}$ and $B_{\text{u.}}$ results, the bar with the left-facing arrow indicates an upper limit at 95% CL. The SM corresponds to $B_{\text{i.}} = B_{\text{u.}} = 0$ and all κ parameters set to unity. All parameters except κ_t and $B_{\text{i.}}$ are assumed to be positive. In the former case, the level of compatibility between the combined measurement and the SM prediction, estimated using the procedure outlined in the text with nine degrees of freedom, corresponds to a p-value of $p_{\text{SM}} = 33\%$. In the latter scenario, p_{SM} in not provided due to the bounds on $\kappa_{W,Z}$.

Table 8: Fit results for Higgs boson coupling modifiers per particle type with effective photon, $Z\gamma$ and gluon couplings and either (a) $B_{\text{i.}} = B_{\text{u.}} = 0$, or (b) $B_{\text{i.}}$ and $B_{\text{u.}}$ included as free parameters, with the conditions $\kappa_{W,Z} \leq 1$ imposed and the measurement of the Higgs boson decay rate into invisible final states included in the combination. The SM corresponds to $B_{\text{i.}} = B_{\text{u.}} = 0$ and all κ parameters set to unity. All κ parameters except for κ_t are assumed to be positive.

Parameter	(a) $B_{\text{i.}} = B_{\text{u.}} = 0$	(b) $B_{\text{i.}}$ free, $B_{\text{u.}} \geq 0$, $\kappa_{W,Z} \leq 1$
κ_Z	0.99 ± 0.06	$0.96\ ^{+\ 0.04}_{-\ 0.05}$
κ_W	1.06 ± 0.06	$1.00\ ^{+\ 0.00}_{-\ 0.03}$
κ_b	0.87 ± 0.11	$0.81\ \pm 0.08$
κ_t	0.92 ± 0.10	$0.90\ \pm 0.10$
κ_μ	$1.07\ ^{+\ 0.25}_{-\ 0.30}$	$1.03\ ^{+\ 0.23}_{-\ 0.29}$
κ_τ	0.92 ± 0.07	0.88 ± 0.06
κ_γ	1.04 ± 0.06	1.00 ± 0.05
$\kappa_{Z\gamma}$	$1.37\ ^{+\ 0.31}_{-\ 0.37}$	$1.33\ ^{+\ 0.29}_{-\ 0.35}$
κ_g	$0.92\ ^{+\ 0.07}_{-\ 0.06}$	$0.89\ ^{+\ 0.07}_{-\ 0.06}$
$B_{\text{i.}}$	-	< 0.09 at 95% CL
$B_{\text{u.}}$	-	< 0.16 at 95% CL

6.6 Generic parameterisation using ratios of coupling modifiers

The six absolute coupling-strength scale factors and three effective loop-coupling scale factors measured in the previous benchmark model are expressed as ratios of scale factors that can be measured independent of any assumptions about the Higgs boson total width, together with a global scale factor determined by the $gg \to H \to ZZ^*$ process. The model parameters are defined in Table 9. All parameters are assumed to be positive. This parameterisation represents the most model-independent determination of coupling-strength scale factors that is currently possible in the κ-framework. The numerical results from the fit to this benchmark model are summarised in Table 9 and visualised in Figure 15. All model parameters are measured to be compatible with their SM expectation. The level of compatibility between the SM hypothesis with the best-fit point corresponds to a p-value of 34%, computed using the procedure outlined in Section 3 with nine degrees of freedom.

The parameter λ_{WZ} in this model is of particular interest: identical coupling-strength scale factors for the W and Z bosons are required within tight bounds by the SU(2) custodial symmetry and the ρ parameter measurements at LEP and at the Tevatron [64]. The ratios $\lambda_{\gamma Z}$ and $\lambda_{Z\gamma Z}$ are sensitive to new charged particles contributing to the $H \to \gamma\gamma$ and $H \to Z\gamma$ loops unlike in $H \to ZZ^*$ decays. Similarly, the ratio λ_{tg} is sensitive to new colored particles contributing through the ggF loop unlike in $t\bar{t}H$ or tH events. The observed values are in agreement with the SM expectation.

Table 9: Best-fit values and uncertainties for ratios of coupling modifiers. The second column provides the expression of the measured parameters in terms of the coupling modifiers defined in previous sections. All parameters are defined to be unity in the SM.

Parameter	Definition in terms of κ modifiers	Result
κ_{gZ}	$\kappa_g\kappa_Z/\kappa_H$	0.98 ± 0.05
λ_{tg}	κ_t/κ_g	1.00 ± 0.11
λ_{Zg}	κ_Z/κ_g	1.07 ± 0.09
λ_{WZ}	κ_W/κ_Z	1.07 ± 0.06
$\lambda_{\gamma Z}$	κ_γ/κ_Z	1.05 ± 0.06
$\lambda_{Z\gamma Z}$	$\kappa_{Z\gamma}/\kappa_Z$	$1.39\ ^{+\ 0.31}_{-\ 0.37}$
$\lambda_{\tau Z}$	κ_τ/κ_Z	0.93 ± 0.07
λ_{bZ}	κ_b/κ_Z	$0.89\ ^{+\ 0.10}_{-\ 0.09}$
$\lambda_{\mu\tau}$	κ_μ/κ_τ	$1.16\ ^{+\ 0.28}_{-\ 0.33}$

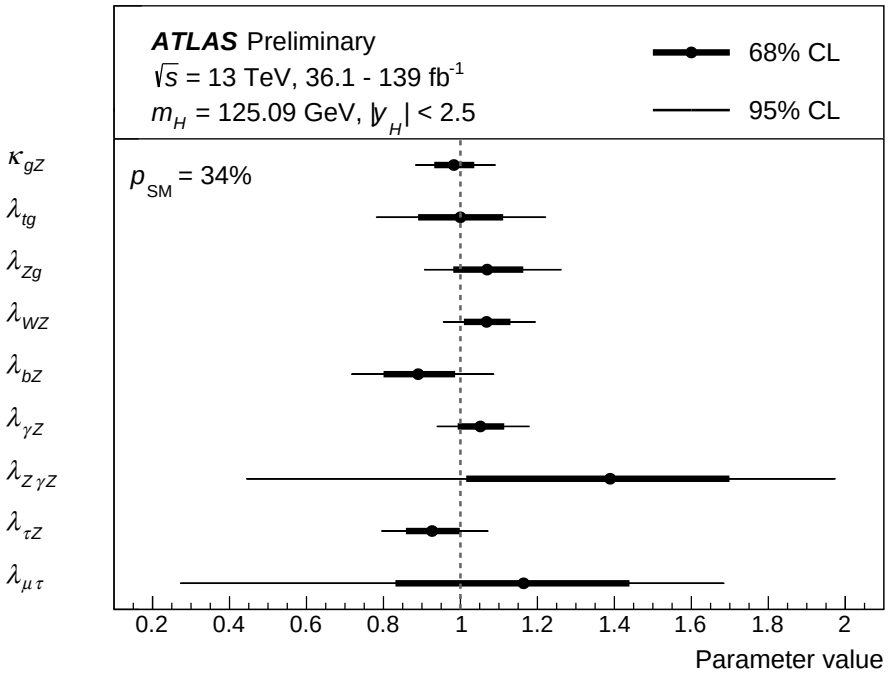

Figure 15: Measured ratios of coupling modifiers. The dashed line indicates the SM value of unity for each parameter. The level of compatibility between the combined measurement and the SM prediction, estimated using the procedure outlined in the text with nine degrees of freedom, corresponds to a p-value of 34%.

7 Interpretation within the SM Effective Field Theory framework

Effective field theories provide a model-independent approach, systematically improvable with higher-order perturbative calculations, to parametrise the effects of candidate BSM theories that reduce to the Standard Model at low energies. In SM Effective Field Theory (SMEFT), the effects of BSM dynamics at energy scales Λ that are large in comparison to the Higgs vacuum-expectation-value v ($\Lambda \gg v$) can be parametrised at low energies, $E \ll \Lambda$, in terms of higher-dimensional operators built up from the Standard Model fields and respecting its symmetries:

$$\mathcal{L}_{\text{SMEFT}} = \mathcal{L}_{\text{SM}} + \sum_{i}^{N_{d6}} \frac{c_i}{\Lambda^2} O_i^{(6)} + \sum_{j}^{N_{d8}} \frac{b_i}{\Lambda^4} O_i^{(8)} + \ldots, \tag{5}$$

where $\mathcal{L}_{\text{SM}}$ is the SM Lagrangian, $O_i^{(6)}$ and $O_i^{(8)}$ represent a complete set of operators of mass-dimensions $d = 6$ and $d = 8$, while c_i and b_j are the corresponding Wilson coefficients. Operators with $d = 5$ and $d = 7$ violate lepton and/or baryon number conservation and are not relevant for Higgs physics. The effective theory expansion in Eq. 5 is robust, fully general, and can be systematically matched to explicit ultraviolet-complete BSM scenarios.

Measurements of (fiducial) cross-sections can be used to constrain the Wilson coefficients associated to each SMEFT operator, and hence put constraints on new physics at a given fixed scale Λ. The interpretation of the cross-section measurements presented in this note closely follows the methodology introduced in Ref. [46]. The expected number of signal events (Eq. 1) is expressed for each Stage 1.2 STXS bin i and Higgs boson decay mode f in terms of signal strength modifiers $\mu_{if} = (\sigma \times B)_{if} / (\sigma \times B)_{if}^{\text{SM}}$ multiplying the corresponding highest-order state-of-the-art prediction. Dedicated (next-to-)leading-order SMEFT predictions are employed to parametrise the signal strength modifiers μ_{if} as a function of relevant Wilson coefficients (see Section 7.1). It is assumed that these parametrisations will not be significantly affected by higher-order contributions [65]. Second, since not all Wilson coefficients can be simultaneously constrained by the available data, a dedicated set of all relevant linear combinations of Wilson coefficients (eigenvectors) is chosen for the fit to data (Section 7.2). Finally, the SMEFT signal parametrisation is then used to constrain the Wilson coefficients in the combined fit to all STXS input measurements listed in Table 1 (Section 7.3). Compared to the previous SMEFT interpretation [46], the new input measurements from $H \to WW^*$, $H \to \tau\tau$ and VBF, $t\bar{t}H$ and high-p_T^H-VH $H \to b\bar{b}$ channels used in this analysis provide an improved sensitivity and help in resolving ambiguities among the fitted parameters.

The SMEFT operators are defined within the Warsaw basis [66] which forms a complete set of all $O_i^{(6)}$ operators allowed by the SM gauge symmetries. Contributions of operators of mass-dimension $d = 8$ or higher are not considered, as the corresponding calculations are not available for all considered processes. The analysis aims to constrain the $d = 6$ Wilson coefficients corresponding to operators that either directly or indirectly impact Higgs boson couplings to SM particles. Table 10 lists the operators considered in this analysis and their corresponding Wilson coefficients c_i. Here, all CP-even $d = 6$ operators were considered for which the Λ^{-2}-suppressed contribution to any of the $(\sigma \times B)_{if}$ predictions exceeds 1‰ with respect to the SM prediction at $c_i = 1$. In this analysis, a value of $\Lambda = 1$ TeV is assumed, coefficients for alternative values of $\Lambda = X$ can be trivially obtained through a scaling with a factor $(X/1\,\text{TeV})^2$. All complex-valued Wilson coefficients, notably c_{uW}, c_{uG}, c_{uB} and c_{uH} in this analysis, are used with $\Im(c_i) = 0$.

Table 10: Wilson coefficients c_i and corresponding dimension-6 SMEFT operators $O_i^{(6)}$ used in this analysis.

Wilson coefficient	Operator	Wilson coefficient	Operator
$c_{H\Box}$	$(H^\dagger H)\Box(H^\dagger H)$	c_{uG}	$(\bar{q}_p\sigma^{\mu\nu}T^A u_r)\widetilde{H}\,G^A_{\mu\nu}$
c_{HDD}	$\left(H^\dagger D^\mu H\right)^*\left(H^\dagger D_\mu H\right)$	c_{uW}	$(\bar{q}_p\sigma^{\mu\nu}u_r)\tau^I\widetilde{H}\,W^I_{\mu\nu}$
c_{HG}	$H^\dagger H\,G^A_{\mu\nu}G^{A\mu\nu}$	c_{uB}	$(\bar{q}_p\sigma^{\mu\nu}u_r)\widetilde{H}\,B_{\mu\nu}$
c_{HB}	$H^\dagger H\,B_{\mu\nu}B^{\mu\nu}$	c'_{ll}	$(\bar{l}_p\gamma_\mu l_t)(\bar{l}_r\gamma^\mu l_s)$
c_{HW}	$H^\dagger H\,W^I_{\mu\nu}W^{I\mu\nu}$	$c^{(1)}_{qq}$	$(\bar{q}_p\gamma_\mu q_t)(\bar{q}_r\gamma^\mu q_s)$
c_{HWB}	$H^\dagger\tau^I H\,W^I_{\mu\nu}B^{\mu\nu}$	$c^{(3)}_{qq}$	$(\bar{q}_p\gamma_\mu\tau^I q_r)(\bar{q}_s\gamma^\mu\tau^I q_t)$
c_{eH}	$(H^\dagger H)(\bar{l}_p e_r H)$	c_{qq}	$(\bar{q}_p\gamma_\mu q_t)(\bar{q}_r\gamma^\mu q_s)$
c_{uH}	$(H^\dagger H)(\bar{q}_p u_r\widetilde{H})$	$c^{(31)}_{qq}$	$(\bar{q}_p\gamma_\mu\tau^I q_t)(\bar{q}_r\gamma^\mu\tau^I q_s)$
c_{dH}	$(H^\dagger H)(\bar{q}_p d_r\widetilde{H})$	c_{uu}	$(\bar{u}_p\gamma_\mu u_r)(\bar{u}_s\gamma^\mu u_t)$
$c^{(1)}_{Hl}$	$(H^\dagger i\overleftrightarrow{D}_\mu H)(\bar{l}_p\gamma^\mu l_r)$	$c^{(1)}_{uu}$	$(\bar{u}_p\gamma_\mu u_t)(\bar{u}_r\gamma^\mu u_s)$
$c^{(3)}_{Hl}$	$(H^\dagger i\overleftrightarrow{D}^I_\mu H)(\bar{l}_p\tau^I\gamma^\mu l_r)$	$c^{(1)}_{qu}$	$(\bar{q}_p\gamma_\mu q_t)(\bar{u}_r\gamma^\mu u_s)$
c_{He}	$(H^\dagger i\overleftrightarrow{D}_\mu H)(\bar{e}_p\gamma^\mu e_r)$	$c^{(8)}_{ud}$	$(\bar{u}_p\gamma_\mu T^A u_r)(\bar{d}_s\gamma^\mu T^A d_t)$
$c^{(1)}_{Hq}$	$(H^\dagger i\overleftrightarrow{D}_\mu H)(\bar{q}_p\gamma^\mu q_r)$	$c^{(8)}_{qu}$	$(\bar{q}_p\gamma_\mu T^A q_r)(\bar{u}_s\gamma^\mu T^A u_t)$
$c^{(3)}_{Hq}$	$(H^\dagger i\overleftrightarrow{D}^I_\mu H)(\bar{q}_p\tau^I\gamma^\mu q_r)$	$c^{(8)}_{qd}$	$(\bar{q}_p\gamma_\mu T^A q_r)(\bar{d}_s\gamma^\mu T^A d_t)$
c_{Hu}	$(H^\dagger i\overleftrightarrow{D}_\mu H)(\bar{u}_p\gamma^\mu u_r)$	c_W	$\epsilon^{IJK}W^{I\nu}_\mu W^{J\rho}_\nu W^{K\mu}_\rho$
c_{Hd}	$(H^\dagger i\overleftrightarrow{D}_\mu H)(\bar{d}_p\gamma^\mu d_r)$	c_G	$f^{ABC}G^{A\nu}_\mu G^{B\rho}_\nu G^{C\mu}_\rho$

7.1 Simulation of the impact of SMEFT operators

The impact of the $d = 6$ SMEFT operators listed in Table 10 has been computed with the UFO model using MadGraph5_aMC@NLO [67]. Calculations for most Higgs production and decay modes have been performed at LO accuracy in QCD with SMEFTsim v3.0 [68], under the assumption of a $U(3)^5$ flavour symmetry, and providing the Fermi constant G_F, and the Z and W boson masses as input. Exception are ggF, $gg \to ZH$ and $H \to gg$ calculations, performed at NLO accuracy in QCD with SMEFTatNLO [69], and calculations for SMEFT-SM interference terms in $H\to\gamma\gamma$, performed at NLO accuracy in QED [70], all providing m_W as input. SMEFT modifications to the background processes in the included analyses are not considered.

A fully linearised signal parametrisation is employed (Section 3.2 in Ref. [46]), considering only EFT contributions from the interference between the SM and the dimension-6 SMEFT operators. These are suppressed by up to factor $1/\Lambda^2$ compared to the SM contribution and have a linear dependence on the dimension-6 Wilson coefficients. The expected impact of the most relevant SMEFT operators on the signal cross section in a given Stage-1.2 STXS bin and on the branching ratio of a given Higgs decay channel is shown in Figure 16. Further BSM contributions involving exclusively dimension-6 SMEFT operators introduce a quadratic dependence on the dimension-6 Wilson coefficients. Being suppressed by a factor $1/\Lambda^4$, they are generally expected to be small and are neglected in this analysis, though their impact may still be non-negligible in certain regions of phase space. Due to the limited time available, the impact of such terms will only be considered in the next iteration of the analysis. Their contribution, however, has to be considered with caution, since the lowest-order cross-section interference terms generated by $d = 8$ operators are also suppressed by a factor $1/\Lambda^4$ and may have a comparable contribution.

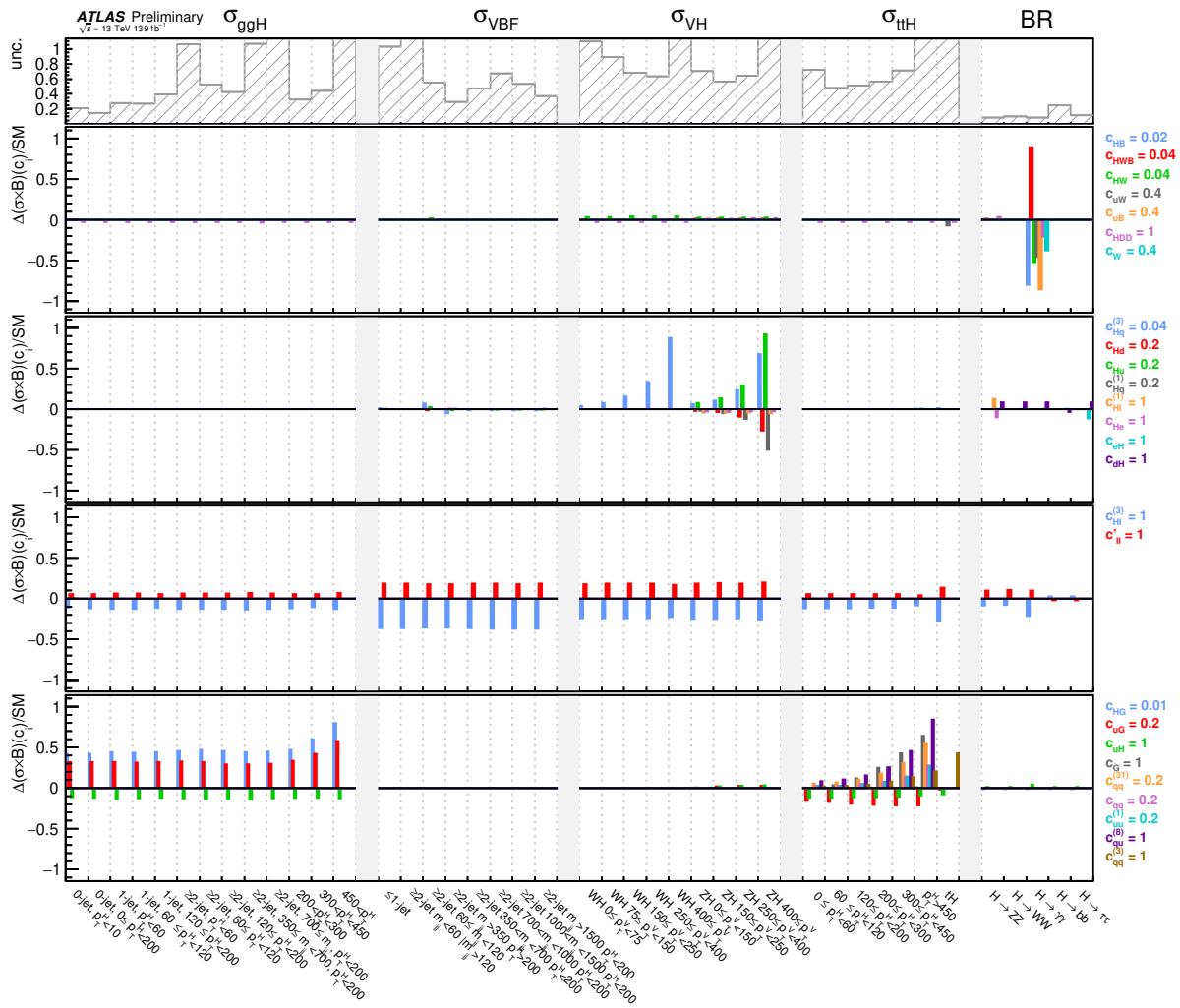

Figure 16: Impact of the most relevant SMEFT operators on the STXS regions and decay modes, relative to the SM cross-section, under the assumption of the linearised SMEFT model. To judge the experimental sensitivity to constrain the operators from the data in the listed STXS regions, the total uncertainty on measurement in the corresponding regions is shown in the top panel. For presentational clarity, the statistical uncertainty of low precision STXS regions is clipped in the plot.

It is assumed that the systematic uncertainties assigned to the acceptance factors $(A \times \epsilon)^k_{if}$ that multiply μ_{if} in Eq. 1, arising from theory uncertainties which are fully taken into account in the SM cross-section prediction, cover the possible acceptance changes induced by SMEFT operators in Higgs production through the full validity range of the SMEFT model. The use of this assumption is motivated by the similarity of reconstruction-level analysis regions to STXS cross-section regions, which are designed to be relatively insensitive to acceptance changes induced by SMEFT operators. The effect of SMEFT operators on other observables used in the definition of the analysis regions, e.g through multivariate discriminants, is assumed to be negligible.

On the other hand, the impact of SMEFT operators on Higgs boson decays can strongly affect the acceptance factors since decays are not limited to a restricted fiducial phase space in the STXS framework. While for most decays, in particular two-body decays, such acceptance effects are found to be negligible, there is a significant impact observed on the $H \to 4\ell$ and $H \to \ell\nu\ell\nu$ four-body decays. Dedicated acceptance corrections are therefore evaluated in these two channels for each Wilson coefficient that affects the corresponding Higgs decay vertex. Corrections are obtained as a difference of the fiducial and the inclusive signal predictions for the considered decay vertex using the fully linearised signal parametrisation approach, and then added to the linearised inclusive signal prediction. The linearised acceptance corrections evaluated for the $H \to 4\ell$ decay channel are shown to be in good agreement with those calculated previously with a non-linear parametrisation in Ref. [11].

7.2 Choice of EFT fit parameters

The available data samples contain insufficient information to constrain all coefficients c_i in Table 10 simultaneously. As degrees of freedom left unconstrained by the data do not necessarily correspond to individual coefficients c_i, but may also be linear combinations $\sum_i a_i c_i$, a modified basis of Wilson coefficients c'_i is estimated following the methodology described in Ref. [46]. First, the eigenvalue decomposition procedure is performed based on the SM expected covariance matrix of $(\sigma \times B)_{if}$ STXS measurements, assuming the Gaussian behaviour of STXS measurements, in order to determine to which Wilson coefficients the fit is sensitive. In order to reduce the impact of correlations with low-sensitivity parameters on the fit results while grouping the parameters into groups with a similar physics impact, only eigenvectors with a significant eigenvalue (larger than ~0.1) are further considered. The chosen eigenvalue threshold approaches the domain with the limited validity of the EFT approach. Based on this selection, the final choice of linear combinations c'_i is then obtained from a subsequent new eigenvector decomposition in sub-spaces of Wilson coefficients, which are grouped together based on the following physics information:

- Parameter $c_{H\Box}$ appears as an overall normalisation to all bins; it is thus excluded from the fit and can be added back to the results as an overall correction to all fitted parameters.
- Parameter $c^{(3)}_{Hq}$ has a good standalone sensitivity and could be fitted separately; it's sensitivity is driven by the VH measurements, in particular in the $H \to b\bar{b}$ channel.
- While the parameter c_{eH} was not accessible in the previous combined interpretation [46], it can now be constrained mainly due to the Yukawa coupling measurements in the $H \to \tau\tau$ channel.
- Parameters c_{HG}, c_{uG} and c_{uH} are constrained by both the ggF and $t\bar{t}H$ measurements, while $c^{(1)}_{qq}$, c_{qq}, $c^{(3)}_{qq}$, $c^{(31)}_{qq}$, c_{uu}, $c^{(1)}_{uu}$, $c^{(8)}_{ud}$, $c^{(1)}_{qu}$, $c^{(8)}_{qu}$, $c^{(8)}_{qd}$ and c_G are only constrained from $t\bar{t}H$ (and, for some, tH) and affect the shape of the signal in a similar way. The updated $t\bar{t}H$, $H \to b\bar{b}$ measurement

introduces additional separation power between the ggF and $t\bar{t}H$ related parameters. The operators c_{HG}, c_{uG} and c_{uH} that are strongest constrained from the ggF production mode are therefore grouped into one sub-space, while the remaining ones are joined together within another sub-space (referred to as c_{top}).

- Parameters c_{uW} and c_{uB} are also constrained by $t\bar{t}H$ but are additionally and mostly constrained by the $H \to \gamma\gamma$ decay, as are also c_{HW}, c_{HB}, and c_{HWB} parameters. The c_W operator also gives a small contribution to the $H \to \gamma\gamma$ channel and is now taken into account, while it was neglected in the previous combination. Therefore, a rotation of these six Wilson coefficients is considered in addition to c_{HDD}. Their correlation with the ggF and top-quark related parameters is due to the strength of the measurement of these production modes in $ggH(\to \gamma\gamma)$ channel.
- Parameters $c_{Hl}^{(1)}$, $c_{Hl}^{(3)}$, c_{He} and $c_{Hq}^{(1)}$, are strongly correlated, constrained mainly by the VH, $H \to b\bar{b}$ (and VBF $H \to b\bar{b}$) measurements. Similarly, there there is also a correlation between $c_{Hl}^{(3)}$ and c'_{ll} as well as between c_{Hu} and c_{Hd} parameters. Based on the main constraining processes, three groupings are defined here: $\{c_{Hl}^{(1)}, c_{He}\}$, $\{c_{Hl}^{(3)}, c'_{ll}\}$ and $\{c_{Hu}, c_{Hd}, c_{Hq}^{(1)}\}$.
- Parameter c_{dH} affecting the Hbb Yukawa coupling can now also be probed due to the additional sensitivity provided by an updated VBF $H \to b\bar{b}$ measurement, which reduces the correlation between the parameters in the VH production and the $H \to b\bar{b}$ decay.

The final parameter set c'_i entering the combined fit and the corresponding rotation matrix of this basis with respect to the Warsaw basis is visualised in Figure 17.

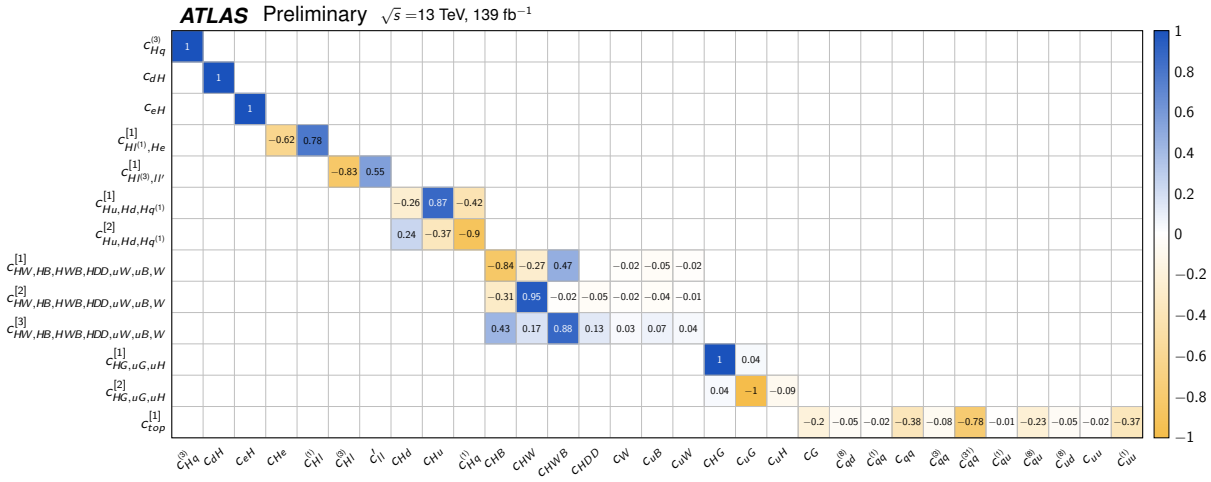

Figure 17: Visualisation of the projection matrix from the Warsaw basis c_i (x-axis) to the fit basis c'_i (y-axis).

7.3 EFT interpretation results

The observed and the SM expected constraints on the parameters c'_i using the linearised SMEFT model are summarised in Table 11 and visualised in Figure 18. All measured parameters are consistent with the SM expectation within their uncertainty. The level of compatibility between the SM hypothesis with the best-fit point corresponds to a p-value of $p_{\text{SM}} = 59\%$, computed using the procedure outlined in Section 3 with 13 degrees of freedom. Comparing the observed results with those from the interpretation in terms of

Table 11: Summary of the observed and the SM expected measurement of the parameters c_i' with the SMEFT linearised model. The ranges correspond to 68% and 95% confidence level intervals, where all other coefficients and all nuisance parameters were left as free parameters in the fit.

Model Parameter	Observed			Expected	
(Λ = 1 TeV)	Best-fit	68% CI	95% CI	68% CI	95% CI
$c_{Hq}^{(3)}$	0.0	$[-0.04, 0.05]$	$[-0.08, 0.1]$	$[-0.04, 0.05]$	$[-0.08, 0.09]$
c_{dH}	3.2	$[0.5, 6]$	$[-2.1, 9]$	$[-2.7, 2.7]$	$[-5, 5]$
c_{eH}	1.8	$[0.23, 4]$	$[-1.5, 5]$	$[-1.7, 1.7]$	$[-3.5, 3.2]$
$c^{[1]}_{HW,HB,HWB,HDD,uW,uB,W}$	0.001	$[-0.004, 0.005]$	$[-0.009, 0.01]$	$[-0.005, 0.004]$	$[-0.009, 0.009]$
$c^{[2]}_{HW,HB,HWB,HDD,uW,uB,W}$	0.4	$[-0.30, 1.0]$	$[-0.9, 1.7]$	$[-0.6, 0.6]$	$[-1.3, 1.3]$
$c^{[3]}_{HW,HB,HWB,HDD,uW,uB,W}$	-0.4	$[-4, 1.9]$	$[-6, 5]$	$[-2.7, 2.8]$	$[-5, 6]$
$c^{[1]}_{Hl^{(1)},He}$	-0.4	$[-1.4, 0.7]$	$[-2.5, 1.7]$	$[-1.0, 1.0]$	$[-2.0, 2.0]$
$c^{[1]}_{Hu,Hd,Hq^{(1)}}$	0.0	$[-0.4, 0.4]$	$[-0.9, 0.8]$	$[-0.4, 0.4]$	$[-0.9, 0.8]$
$c^{[2]}_{Hu,Hd,Hq^{(1)}}$	-0.8	$[-6, 4]$	$[-10, 9]$	$[-5, 5]$	$[-10, 10]$
$c^{[1]}_{Hl^{(3)},ll'}$	0.15	$[-0.4, 0.7]$	$[-0.9, 1.3]$	$[-0.5, 0.5]$	$[-1.0, 1.0]$
$c^{[1]}_{HG,uG,uH}$	-0.005	$[-0.01, -0.0018]$	$[-0.013, 0.0021]$	$[-0.004, 0.004]$	$[-0.008, 0.008]$
$c^{[2]}_{HG,uG,uH}$	-0.23	$[-0.7, 0.18]$	$[-1.1, 0.6]$	$[-0.4, 0.5]$	$[-0.9, 0.9]$
$c^{[1]}_{top}$	0.15	$[-0.18, 0.5]$	$[-0.5, 0.8]$	$[-0.4, 0.4]$	$[-0.7, 0.7]$

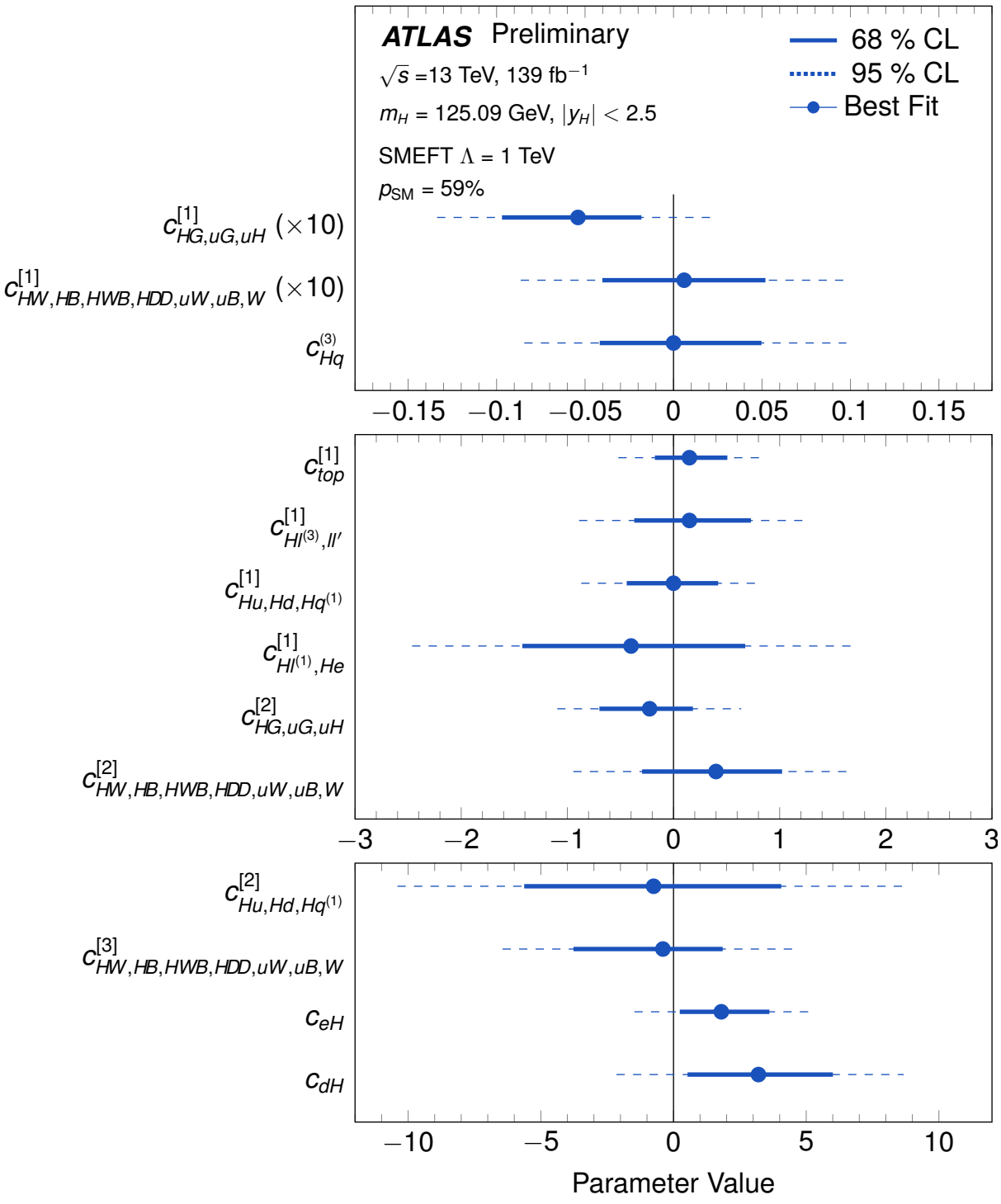

Figure 18: Summary of observed measurements of the parameters c_i' within the SMEFT linearised model. The ranges shown correspond to 68% (solid) and 95% (dashed) confidence level intervals.

the generic parametrisation within the κ-framework (Section 6.5), the following trends in deviations from SM predictions are observed: deviations of the best-fit κ_g and $c^{[1]}_{HG,uG,uH}$ values are both of similar size relative to the measurement uncertainty, and are both below the SM prediction, in accordance with their expected positively correlated impact on the ggF cross section; deviations of the κ_τ and c_{eH} best-fit values are also of similar size but in opposite directions, as is expected from their negatively correlated impact on the $H \to \tau\tau$ decay rate; and finally, similar behavior is also observed for the κ_b and c_{dH} parameters, both of which affect the $H \to b\bar{b}$ decay vertex.

The correlation matrix of the measurement is shown in Figure 19.

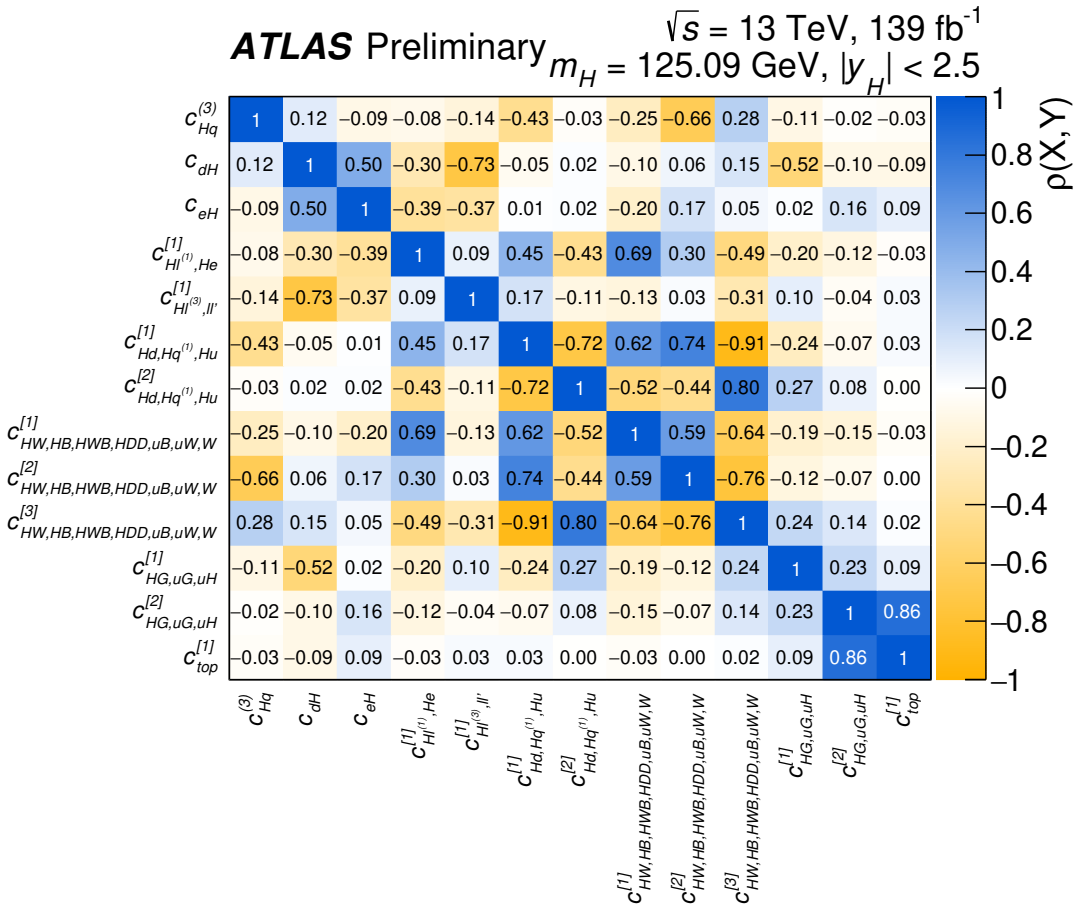

Figure 19: Correlation from the linearised SMEFT model for the observed data. The linear correlation coefficient $\rho(X, Y)$ between pairs of observables is indicated in color and given numerically.

Compared to the previous results in Ref. [46], the correlations between different subgroups of Wilson coefficients are in general reduced due to the additional input from the $H \to \tau\tau$, VBF, $H \to b\bar{b}$ and $t\bar{t}H$, $H \to b\bar{b}$ channels. Together with the additional sensitivity, this allows for the first time for the constraints on the c_{eH}, c_{dH} and $c^{[1]}_{top}$ parameters to be set independently of other parameters in the fit. Furthermore, the sensitivity to the most sensitive directions in the remaining groups of parameters is in general improved by up to 70%.

8 Interpretation in the context of UV-complete BSM theories

In 2HDMs, the SM Higgs sector is extended by introducing an additional complex isodoublet scalar field with a weak hypercharge of one. Both SU(2) doublet Higgs fields acquire a vacuum expectation value, resulting in the prediction of two neutral CP-even, one neutral CP-odd and two charged Higgs bosons. Four types of 2HDMs satisfy the Paschos–Glashow–Weinberg condition [71, 72], which prevents the appearance of tree-level flavor-changing neutral currents:

- Type I: One Higgs doublet couples to vector bosons, while the other one couples to fermions. The first doublet is *fermiophobic* in the limit where the two Higgs doublets do not mix.
- Type II: One Higgs doublet couples to up-type quarks and the other one to down-type quarks and charged leptons.
- Lepton-specific: The Higgs bosons have the same couplings to quarks as in the Type I model and to charged leptons as in Type II.
- Flipped: The Higgs bosons have the same couplings to quarks as in the Type II model and to charged leptons as in Type I.

The observed Higgs boson is identified with the light CP-even neutral scalar predicted by 2HDMs, and its accessible production and decay modes are assumed to be the same as those of the SM Higgs boson, i.e. no other Higgs boson production or decay mechanism contributes to the measured cross sections. Furthermore, it is assumed that only the 2HDMs are responsible for the potential BSM effects in the Higgs boson couplings to vector bosons, up-type quarks, down-type quarks and leptons. The changes with respect to the corresponding SM predictions are expressed as functions of the mixing angle α between the light and the heavy CP-even neutral scalars, and the ratio of the vacuum expectation values of the two Higgs doublets, $\tan\beta$ [73].

Figure 20 shows the regions of the $(\cos(\beta-\alpha), \tan\beta)$ plane that are excluded at a confidence level of 95 % or higher, for each of the four types of 2HDMs. The expected exclusion limits in the SM hypothesis are also overlaid. The data are consistent with the alignment limit [45] at $\cos(\beta-\alpha) = 0$, in which the couplings of h match those of the SM Higgs boson, within one standard deviation or better in each of the tested models. The allowed regions also include narrow, curved *petal* regions at positive $\cos(\beta-\alpha)$ and moderate $\tan\beta$ in the Type II, Lepton-specific, and Flipped models. These correspond to regions with $\cos(\beta+\alpha) \approx 0$, for which some fermion couplings have the same magnitude as in the SM, but the opposite sign.

In general, the expected constraints on different studied 2HDM scenarios improve by about 20%. Compared to previous interpretation results [23], a shift of the exclusion contour towards the smaller $\cos(\beta-\alpha)$ values is observed for the 2HDM Type-I scenario. This is mainly due to the updated $H \to \tau\tau$, $H \to b\bar{b}$ and $t\bar{t}H$ measurements which drive the Yukawa couplings of τ leptons, b quarks and top quarks towards the values below the SM prediction. Similarly, in case of the lepton-specific 2HDM scenario, the lepton coupling (coupling to down-type quarks) at large (small) $\tan\beta$ values shifts the constraints on $\cos(\beta-\alpha)$ towards larger (smaller) values.

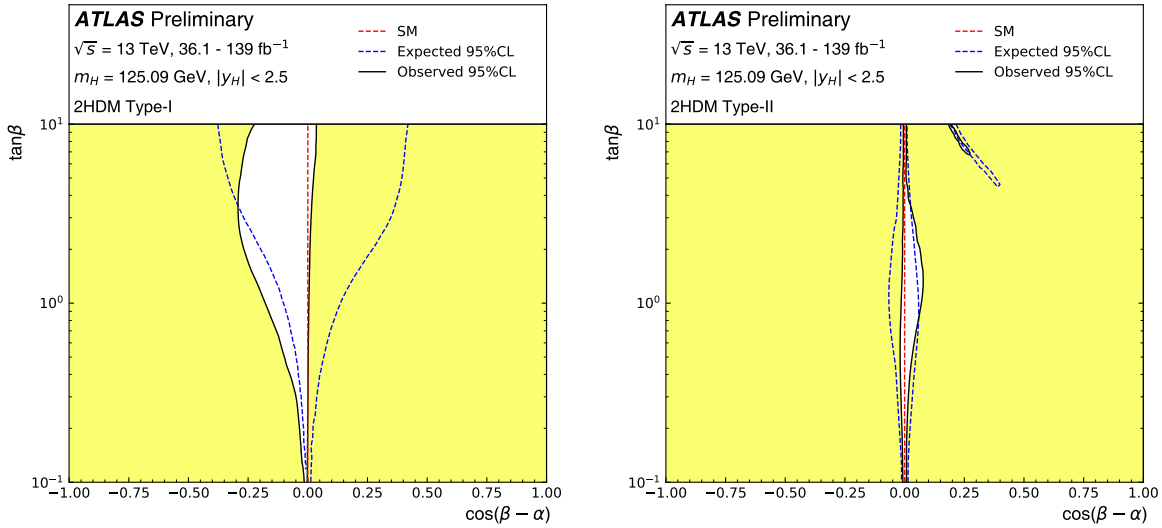

(a)

(b)

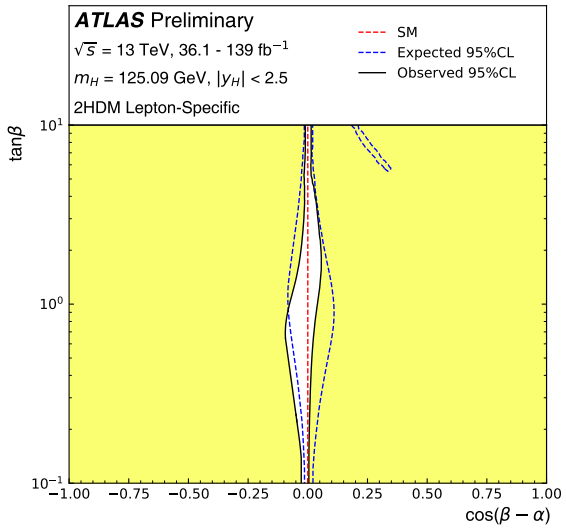

(c)

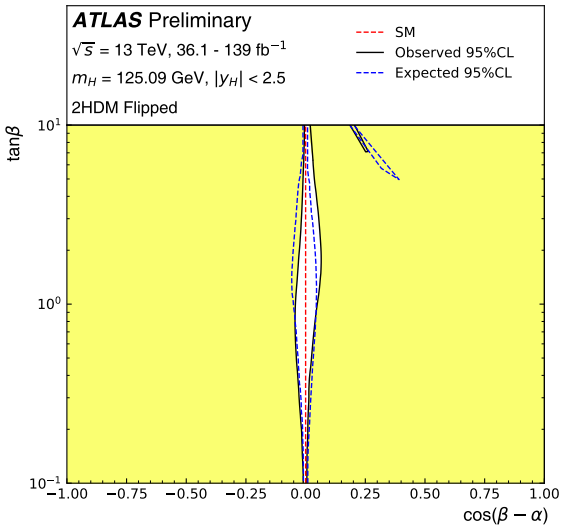

(d)

Figure 20: Regions of the $(\cos(\beta-\alpha), \tan\beta)$ plane of four types of 2HDMs excluded by fits to the measured rates of Higgs boson production and decays. Contours at 95% CL, defined in the asymptotic approximation by $-2\ln\Lambda = 5.99$, are drawn for both the data and the expectation for the SM Higgs sector. In all cases, the observed best-fit points are out of the range, compatible with the degeneracy in $\tan\beta$ along the $\cos(\beta-\alpha) = 0$ axis. The angles α and β are taken to satisfy $0 \leq \beta \leq \pi/2$ and $0 \leq \beta - \alpha \leq \pi$ without loss of generality. The alignment limit at $\cos(\beta-\alpha) = 0$, in which all Higgs boson couplings take their SM values, is indicated by the dashed red line. Best-fit values are not shown due to the limited sensitivity to the $\tan\beta$ parameter. The observed best-fit values for $\cos(\beta-\alpha)$ are -0.006 for the Type-I, 0.002 for the Type-II, 0.001 for the lepton-specific and 0.002 for the flipped scenario.

9 Conclusions

Measurements of Higgs boson production cross sections and branching fractions have been performed using up to 139 fb^{-1} of pp collision data produced by the LHC at $\sqrt{s}$ = 13 TeV and recorded by the ATLAS detector. The results presented in this note are based on the combination of analyses of the $H \to \gamma\gamma$, $H \to ZZ^*$, $H \to WW^*$, $H \to \tau\tau$, $H \to b\bar{b}$, $H \to \mu\mu$ and $H \to Z\gamma$ decay modes and a search for decays into invisible final states in the vector boson fusion (VBF) production mode. Compared to the previous combined measurement, the $Z\gamma$ decays, the $b\bar{b}$ decays with highly boosted Higgs bosons, the $H \to \tau\tau$ decays produced in association with a vector boson, and the fully-hadronic $H \to \tau\tau$ decays produced in association with top quarks are included for the first time, while the WW and $\tau\tau$ analyses targeting both the ggF and VBF production modes, as well as the $b\bar{b}$ analyses targeting the VBF and $t\bar{t}H$ production modes are updated to the full Run 2 data set.

The global signal strength is determined to be $\mu = 1.06 \pm 0.06$, improving by 10% compared to the previous result. The Higgs boson production cross sections within the region $|y_H| < 2.5$ are measured in a combined fit for the gluon–gluon fusion process, vector boson fusion, the associated production with a W or Z boson and the associated production with top quarks, assuming the SM Higgs boson branching fractions. Several other measurements have been performed, including production cross section times branching fraction for each pair of production and decay processes, and ratios of production cross sections relative to gluon–gluon fusion and ratios of branching fractions relative to $H \to ZZ^*$, together with the cross section of the $gg \to H \to ZZ^*$ process. Measurements are also provided in the simplified template cross section framework. In addition, the measurements are interpreted in terms of the coupling strength modifiers (κ-framework) and in the context of the Standard Model Effective Field Theory (SMEFT) and Two-Higgs-Doublet-Model predictions.

The vector boson fusion cross section measurement improves by about 30% due to the updated $H \to WW^*$ and VBF $H \to b\bar{b}$ input analyses, while the updated $H \to \tau\tau$ and $H \to b\bar{b}$ analyses lead to improvements of the corresponding branching ratio and coupling modifier measurements by up to 50%. The combination includes for the first time also the $Z\gamma$ decay channel, allowing to set constraints on the corresponding effective coupling modifier, with the observed (expected) signal significance of 2.2 σ (1.1 σ) relative to the absence of this coupling. The newly added measurement of the $H \to b\bar{b}$ process with boosted Higgs bosons produced in association with a vector boson, as well as an increased amount of data in the updated input analyses allow for a higher granularity of simplified template cross section measurements at large Higgs boson transverse momentum as well as at large invariant mass of the dijet system. Constraints on different groups of linear combinations of SMEFT parameters are improved by up to 70%. For the first time, two additional SMEFT parameters, related to the τ-lepton and b-quark Yukawa couplings, are probed separately from other parameters of interest in the fit. Furthermore, the sensitivity on the $(\cos(\beta - \alpha), \tan\beta)$ parameter space for selected benchmark scenarios of the Two Higgs Doublet Model is also improved by about 20% compared to the previous results. In all cases, no significant deviations from SM predictions are observed.

Appendix

A Additional material concerning the cross section measurements

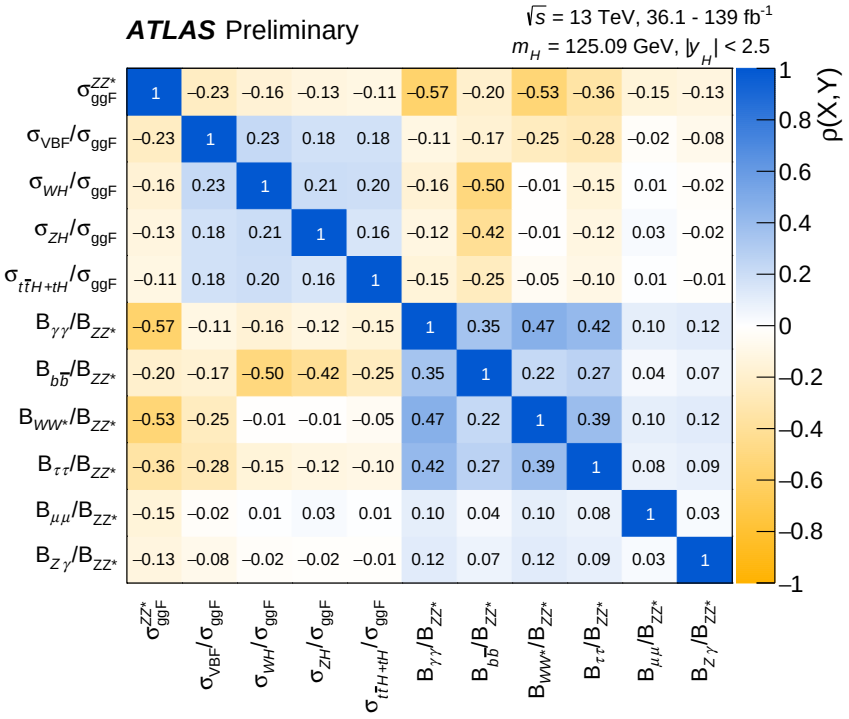

Figure 21: Observed correlation matrix from a simultaneous fit for σ^{ZZ}_{ggF}, $\sigma_{\text{VBF}}/\sigma_{\text{ggF}}$, $\sigma_{WH}/\sigma_{\text{ggF}}$, $\sigma_{ZH}/\sigma_{\text{ggF}}$, $\sigma_{t\bar{t}H+tH}/\sigma_{\text{ggF}}$, $B_{\gamma\gamma}/B_{ZZ}$, B_{WW}/B_{ZZ}, $B_{\tau\tau}/B_{ZZ}$, and B_{bb}/B_{ZZ}. The linear correlation coefficient $\rho(X,Y)$ between pairs of observables is indicated in color and given numerically.

B Additional material concerning the interpretation in the κ framework

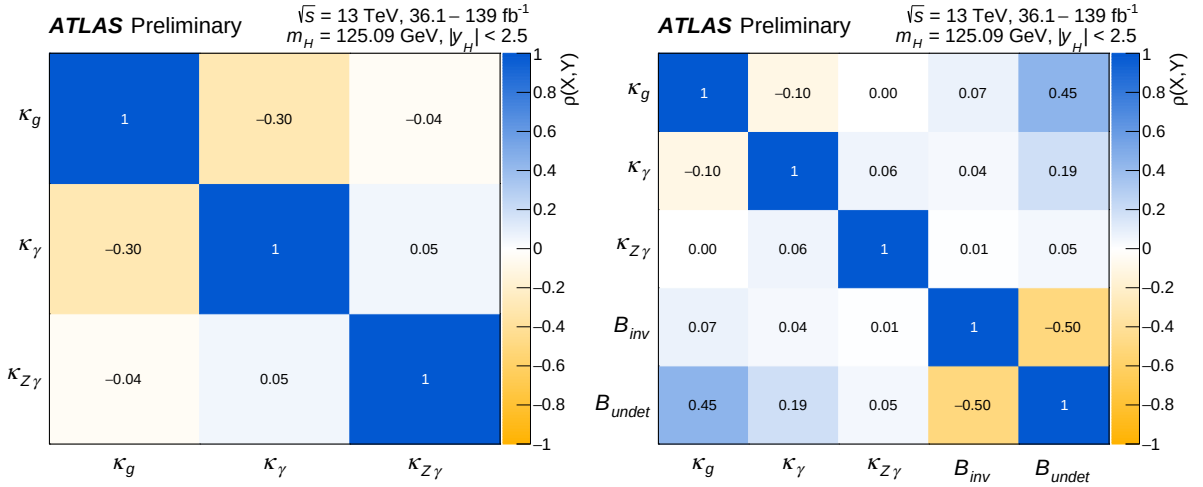

(a) (b)

Figure 22: Observed correlation matrix from the fit of (a) κ_g, κ_γ and $\kappa_{Z\gamma}$, assuming $B_{i.} = B_{u.} = 0$, and (b) κ_g, κ_γ, $\kappa_{Z\gamma}$, $B_{i.}$ and $B_{u.}$ parameters. The linear correlation coefficient $\rho(X, Y)$ between pairs of observables is indicated in color and given numerically.

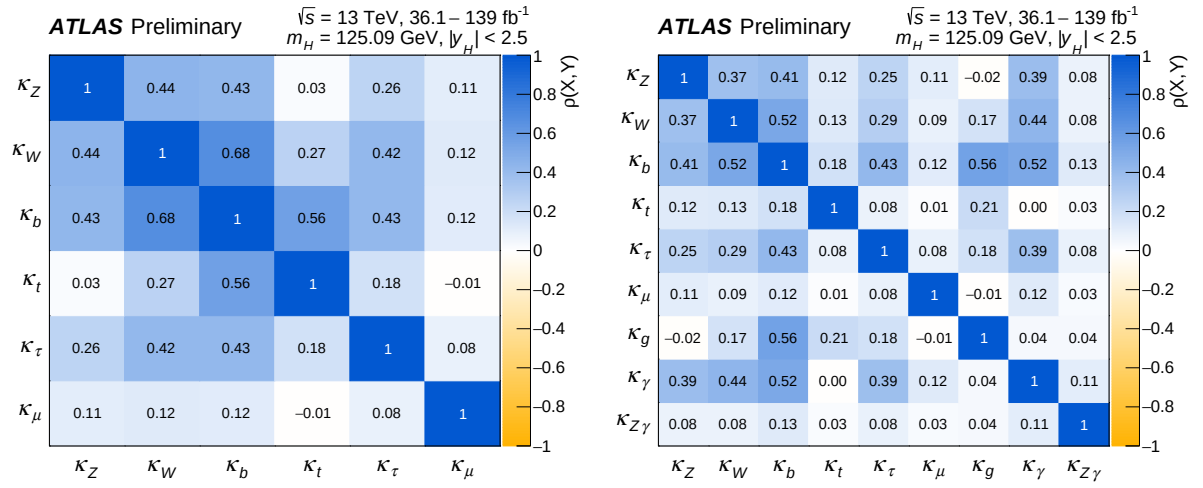

(a) (b)

Figure 23: (a) Observed correlation matrix from the fit of κ_Z, κ_W, κ_b, κ_t, κ_τ and κ_μ, all assumed to be positive. (b) Observed correlation matrix from the fit of the Higgs boson coupling modifiers per particle type with effective photon, $Z\gamma$ and gluon couplings and $B_{\mathrm{i.}} = B_{\mathrm{u.}} = 0$. The linear correlation coefficient $\rho(X, Y)$ between pairs of observables is indicated in color and given numerically.

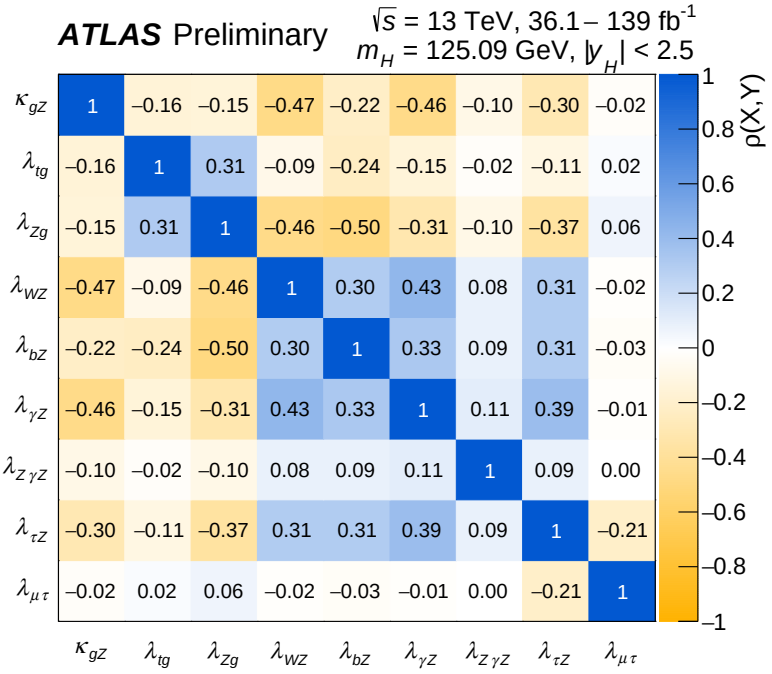

Figure 24: Observed correlation matrix from the fit of the ratios of coupling modifiers. The linear correlation coefficient $\rho(X, Y)$ between pairs of observables is indicated in color and given numerically.

C Additional material concerning the EFT interpretation

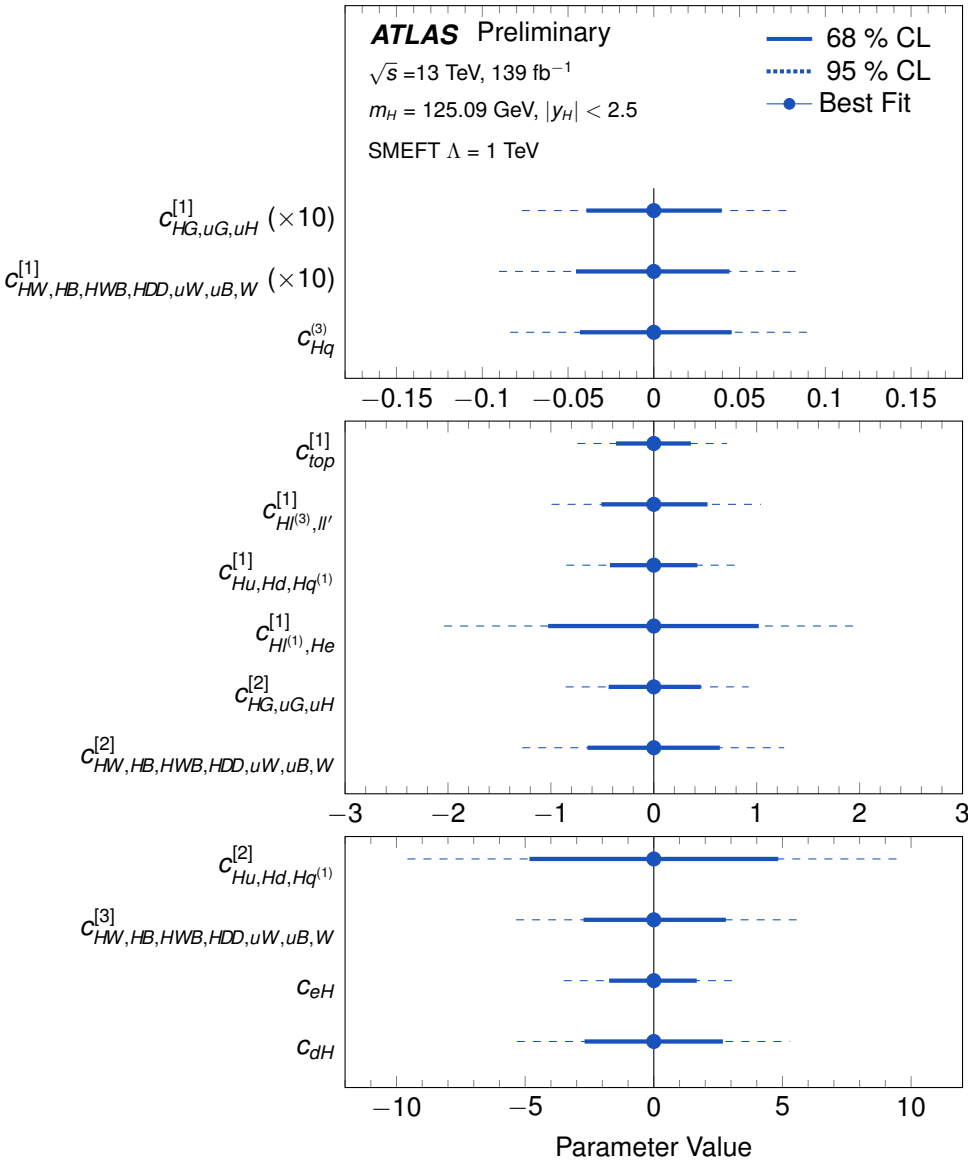

Figure 25: Summary of expected measurements of the parameters c_i' with the SMEFT linearised model. The ranges shown correspond to 68% (solid) and 95% (dashed) confidence level intervals, where all other coefficients and all nuisance parameters were profiled.

Table 12: Parametrisation of the EFT interference terms normalized to the SM prediction for the $gg \to H$ and $qq \to Hqq$ bins of the STXS as defined in its stage 1.2 with the parameter definitions of the SMEFTsim model. The numbers are rounded according to their statistical uncertainty. Dimensional quantities are printed in units of GeV.

STXS Category	**Parameterisation**
$\boldsymbol{gg \to H}$	
$gg \to H$, 0 − jet, $0 < p_{\mathrm{T}}^{H} < 10$	$0.118c_{H\Box} - 0.0294c_{HDD} + 42.0c_{HG} - 0.117c_{uH} + 1.59c_{uG} - 0.117c_{Hl}^{(3)} + 0.0587c'_{ll}$
$gg \to H$, 0 − jet, $10 < p_{\mathrm{T}}^{H} < 200$	$0.1176c_{H\Box} - 0.0295c_{HDD} + 42.2c_{HG} - 0.1186c_{uH} + 1.62c_{uG} - 0.1182c_{Hl}^{(3)} + 0.0590c'_{ll}$
$gg \to H$, 1 − jet, $0 < p_{\mathrm{T}}^{H} < 60$	$0.132c_{H\Box} - 0.0330c_{HDD} + 44.0c_{HG} - 0.132c_{uH} + 1.60c_{uG} - 0.132c_{Hl}^{(3)} + 0.065c'_{ll}$
$gg \to H$, 1 − jet, $60 < p_{\mathrm{T}}^{H} < 120$	$0.125c_{H\Box} - 0.0314c_{HDD} + 43.5c_{HG} - 0.125c_{uH} + 1.58c_{uG} - 0.125c_{Hl}^{(3)} + 0.063c'_{ll}$
$gg \to H$, 1 − jet, $120 < p_{\mathrm{T}}^{H} < 200$	$0.115c_{H\Box} - 0.028c_{HDD} + 44c_{HG} - 0.118c_{uH} + 1.60c_{uG} - 0.112c_{Hl}^{(3)} + 0.058c'_{ll}$
$gg \to H$, ≥ 2 − jet, $0 < m_{jj} < 350$, $0 < p_{\mathrm{T}}^{H} < 60$	$0.128c_{H\Box} - 0.033c_{HDD} + 46c_{HG} - 0.128c_{uH} + 1.63c_{uG} - 0.132c_{Hl}^{(3)} + 0.065c'_{ll}$
$gg \to H$, ≥ 2 − jet, $0 < m_{jj} < 350$, $60 < p_{\mathrm{T}}^{H} < 120$	$0.130c_{H\Box} - 0.033c_{HDD} + 47c_{HG} - 0.133c_{uH} + 1.59c_{uG} - 0.130c_{Hl}^{(3)} + 0.065c'_{ll}$
$gg \to H$, ≥ 2 − jet, $0 < m_{jj} < 350$, $120 < p_{\mathrm{T}}^{H} < 200$	$0.133c_{H\Box} - 0.032c_{HDD} + 46c_{HG} - 0.132c_{uH} + 1.48c_{uG} - 0.130c_{Hl}^{(3)} + 0.066c'_{ll}$
$gg \to H$, ≥ 2 − jet, $350 < m_{jj} < 700$, $0 < p_{\mathrm{T}}^{H} < 200$	$0.137c_{H\Box} - 0.035c_{HDD} + 44c_{HG} - 0.144c_{uH} + 1.48c_{uG} - 0.135c_{Hl}^{(3)} + 0.069c'_{ll}$
$gg \to H$, ≥ 2 − jet, $700 < m_{jj}$, $0 < p_{\mathrm{T}}^{H} < 200$	$0.13c_{H\Box} - 0.032c_{HDD} + 45c_{HG} - 0.13c_{uH} + 1.5c_{uG} - 0.131c_{Hl}^{(3)} + 0.065c'_{ll}$
$gg \to H$, $200 < p_{\mathrm{T}}^{H} < 300$	$0.111c_{H\Box} - 0.030c_{HDD} + 47c_{HG} - 0.122c_{uH} + 1.69c_{uG} - 0.120c_{Hl}^{(3)} + 0.058c'_{ll}$
$gg \to H$, $300 < p_{\mathrm{T}}^{H} < 450$	$0.12c_{H\Box} - 0.029c_{HDD} + 60c_{HG} - 0.12c_{uH} + 2.1c_{uG} - 0.11c_{Hl}^{(3)} + 0.055c'_{ll}$
$gg \to H$, $450 < p_{\mathrm{T}}^{H}$	$0.13c_{H\Box} - 0.029c_{HDD} + 80c_{HG} - 0.13c_{uH} + 2.9c_{uG} - 0.13c_{Hl}^{(3)} + 0.07c'_{ll}$
$\boldsymbol{qq \to Hqq}$	
$qq \to Hqq$, ≤ 1 − jets	$0.121c_{H\Box} - 0.0099c_{HDD} + 0.227c_{HW} + 0.0075c_{HB} + 0.0561c_{HWB} - 0.363c_{Hl}^{(3)} + 0.369c_{Hq}^{(3)} + 0.0313c_{Hu} - 0.0136c_{Hd} + 0.182c'_{ll}$
$qq \to Hqq$, ≥ 2 − jet, $m_{jj} \in (0, 60), (120, 350)$, $0 < p_{\mathrm{T}}^{H} < 200$	$0.122c_{H\Box} - 0.0089c_{HDD} + 0.027c_{HW} + 0.0029c_{HB} + 0.0407c_{HWB} - 0.365c_{Hl}^{(3)} - 0.002c_{Hq}^{(1)} - 0.059c_{Hq}^{(3)} + 0.0038c_{Hu} + 0.182c'_{ll}$
$qq \to Hqq$, ≥ 2 − jet, $60 < p_{\mathrm{T}}^{H} < 120$	$0.119c_{H\Box} - 0.0041c_{HDD} + 0.575c_{HW} + 0.0221c_{HB} + 0.102c_{HWB} - 0.357c_{Hl}^{(3)} - 0.004c_{Hq}^{(1)} + 1.76c_{Hq}^{(3)} + 0.149c_{Hu} - 0.0605c_{Hd} + 0.180c'_{ll}$
$qq \to Hqq$, ≥ 2 − jet, $350 < m_{jj} < 700$, $0 < p_{\mathrm{T}}^{H} < 200$	$0.121c_{H\Box} - 0.0097c_{HDD} - 0.134c_{HW} + 0.0270c_{HWB} - 0.367c_{Hl}^{(3)} - 0.003c_{Hq}^{(1)} - 0.370c_{Hq}^{(3)} - 0.0198c_{Hu} + 0.0091c_{Hd} + 0.184c'_{ll}$
$qq \to Hqq$, ≥ 2 − jet, $700 < m_{jj} < 1000$, $0 < p_{\mathrm{T}}^{H} < 200$	$0.123c_{H\Box} - 0.0100c_{HDD} - 0.145c_{HW} + 0.024c_{HWB} - 0.371c_{Hl}^{(3)} + 0.005c_{Hq}^{(1)} - 0.40c_{Hq}^{(3)} - 0.0242c_{Hu} + 0.0096c_{Hd} + 0.183c'_{ll}$
$qq \to Hqq$, ≥ 2 − jet, $1000 < m_{jj} < 1500$, $0 < p_{\mathrm{T}}^{H} < 200$	$0.123c_{H\Box} - 0.0092c_{HDD} - 0.147c_{HW} - 0.0014c_{HB} + 0.025c_{HWB} - 0.371c_{Hl}^{(3)} + 0.010c_{Hq}^{(1)} - 0.42c_{Hq}^{(3)} - 0.0259c_{Hu} + 0.0090c_{Hd} + 0.181c'_{ll}$
$qq \to Hqq$, ≥ 2 − jet, $1500 < m_{jj}$, $0 < p_{\mathrm{T}}^{H} < 200$	$0.123c_{H\Box} - 0.010c_{HDD} - 0.158c_{HW} + 0.028c_{HWB} - 0.370c_{Hl}^{(3)} + 0.024c_{Hq}^{(1)} - 0.43c_{Hq}^{(3)} - 0.0296c_{Hu} + 0.0085c_{Hd} + 0.186c'_{ll}$
$qq \to Hqq$, ≥ 2 − jet, $350 < m_{jj}$, $200 < p_{\mathrm{T}}^{H}$	$0.120c_{H\Box} - 0.0063c_{HDD} + 0.18c_{HW} + 0.040c_{HWB} - 0.355c_{Hl}^{(3)} + 0.037c_{Hq}^{(1)} - 1.26c_{Hq}^{(3)} - 0.088c_{Hu} + 0.0311c_{Hd} + 0.178c'_{ll}$

Table 13: Parametrisation of the EFT interference terms normalized to the SM prediction for the $qq \to Hl\nu$, $pp \to Hll$, $t\bar{t}H$ and tH bins of the STXS as defined in its stage 1.2 with the parameter definitions of the SMEFTsim model. The numbers are rounded according to their statistical uncertainty. Dimensional quantities are printed in units of GeV.

STXS Category	Parameterisation
$\boldsymbol{qq \to Hl\nu}$	
$qq \to Hl\nu$, $0<p_{\mathrm{T}}^{V}<75$	$0.1209c_{H\Box} - 0.0301c_{HDD} + 0.814c_{HW} - 0.241c_{Hl}^{(3)} + 1.14c_{Hq}^{(3)} + 0.181c'_{ll}$
$qq \to Hl\nu$, $0<p_{\mathrm{T}}^{V}<150$	$0.121c_{H\Box} - 0.0305c_{HDD} + 0.941c_{HW} - 0.242c_{Hl}^{(3)} + 1.91c_{Hq}^{(3)} + 0.182c'_{ll}$
$qq \to Hl\nu$, $150<p_{\mathrm{T}}^{V}<250$	$0.123c_{H\Box} - 0.0303c_{HDD} + 1.05c_{HW} - 0.242c_{Hl}^{(3)} + 3.85c_{Hq}^{(3)} + 0.184c'_{ll}$
$qq \to Hl\nu$, $250<p_{\mathrm{T}}^{V}<400$	$0.122c_{H\Box} - 0.031c_{HDD} + 1.12c_{HW} - 0.242c_{Hl}^{(3)} + 8.4c_{Hq}^{(3)} + 0.186c'_{ll}$
$qq \to Hl\nu$, $400<p_{\mathrm{T}}^{V}$	$0.116c_{H\Box} - 0.028c_{HDD} + 1.06c_{HW} - 0.23c_{Hl}^{(3)} + 22c_{Hq}^{(3)} + 0.17c'_{ll}$
$\boldsymbol{pp \to Hll}$	
$pp \to Hll$, $0<p_{\mathrm{T}}^{V}<150$	$1 + 0.1350c_{H\Box} + 0.0101c_{HDD} + 0.6820c_{HW} + 0.0820c_{HB} + 0.3030c_{HWB} + 0.0060c_{uH} + 0.0435c_{uG} - 0.0458c_{Hl}^{(1)} - 0.2470c_{Hl}^{(3)} - 0.0326c_{He} - 0.1100c_{Hq}^{(1)} + 1.5500c_{Hq}^{(3)} + 0.3880c_{Hu} - 0.1170c_{Hd} + 0.1880c'_{ll}$
$pp \to Hll$, $150<p_{\mathrm{T}}^{V}<250$	$1 + 0.1380c_{H\Box} + 0.0126c_{HDD} + 0.6800c_{HW} + 0.0830c_{HB} + 0.3000c_{HWB} + 0.0189c_{uH} + 0.1070c_{uG} - 0.0460c_{Hl}^{(1)} - 0.2500c_{Hl}^{(3)} - 0.0328c_{He} - 0.2500c_{Hq}^{(1)} + 2.6700c_{Hq}^{(3)} + 0.6860c_{Hu} - 0.1960c_{Hd} + 0.1930c'_{ll}$
$pp \to Hll$, $250<p_{\mathrm{T}}^{V}<400$	$1 + 0.131c_{H\Box} + 0.019c_{HDD} + 0.690c_{HW} + 0.096c_{HB} + 0.310c_{HWB} + 0.031c_{uH} + 0.132c_{uG} - 0.044c_{Hl}^{(1)} - 0.244c_{Hl}^{(3)} - 0.032c_{He} - 0.610c_{Hq}^{(1)} + 5.800c_{Hq}^{(3)} + 1.450c_{Hu} - 0.460c_{Hd} + 0.186c'_{ll}$
$pp \to Hll$, $400<p_{\mathrm{T}}^{V}$	$1 + 0.130c_{H\Box} + 0.022c_{HDD} + 0.660c_{HW} + 0.130c_{HB} + 0.370c_{HWB} + 0.038c_{uH} + 0.149c_{uG} - 0.050c_{Hl}^{(1)} - 0.260c_{Hl}^{(3)} - 0.032c_{He} - 2.500c_{Hq}^{(1)} + 17.0c_{Hq}^{(3)} + 4.600c_{Hu} - 1.340c_{Hd} + 0.200c'_{ll}$
$\boldsymbol{t\bar{t}H}$	
$t\bar{t}H$, $0<p_{\mathrm{T}}^{H}<60$	$-0.002c_G + 0.117c_{H\Box} - 0.0294c_{HDD} + 0.408c_{HG} - 0.119c_{uH} - 0.775c_{uG} - 0.004c_{uW} - 0.001c_{uB} - 0.120c_{Hl}^{(3)} + 0.002c_{Hq}^{(3)} + 0.0595c'_{ll} + 0.0061c_{qq}^{(1)} + 0.130c_{qq} + 0.0234c_{qq}^{(3)} + 0.294c_{qq}^{(31)} + 0.0087c_{uu} + 0.131c_{uu}^{(1)} - 0.001c_{ud}^{(1)} + 0.0218c_{ud}^{(8)} + 0.0055c_{qu}^{(1)} + 0.085c_{qu}^{(8)} - 0.001c_{qd}^{(1)} + 0.0220c_{qd}^{(8)}$
$t\bar{t}H$, $60<p_{\mathrm{T}}^{H}<120$	$0.037c_G + 0.118c_{H\Box} - 0.0295c_{HDD} + 0.479c_{HG} - 0.118c_{uH} - 0.859c_{uG} - 0.005c_{uW} - 0.001c_{uB} - 0.119c_{Hl}^{(3)} + 0.003c_{Hq}^{(3)} + 0.0599c'_{ll} + 0.0077c_{qq}^{(1)} + 0.161c_{qq} + 0.0292c_{qq}^{(3)} + 0.357c_{qq}^{(31)} + 0.0106c_{uu} + 0.159c_{uu}^{(1)} - 0.001c_{ud}^{(1)} + 0.0265c_{ud}^{(8)} + 0.0069c_{qu}^{(1)} + 0.104c_{qu}^{(8)} - 0.001c_{qd}^{(1)} + 0.0263c_{qd}^{(8)}$
$t\bar{t}H$, $120<p_{\mathrm{T}}^{H}<200$	$0.119c_G + 0.116c_{H\Box} - 0.0290c_{HDD} + 0.599c_{HG} + 0.001c_{HW} - 0.117c_{uH} - 0.97c_{uG} - 0.007c_{uW} - 0.002c_{uB} - 0.119c_{Hl}^{(3)} + 0.004c_{Hq}^{(3)} + 0.0597c'_{ll} + 0.0130c_{qq}^{(1)} + 0.244c_{qq} + 0.0453c_{qq}^{(3)} + 0.537c_{qq}^{(31)} + 0.0161c_{uu} + 0.240c_{uu}^{(1)} - 0.002c_{ud}^{(1)} + 0.0385c_{ud}^{(8)} + 0.0102c_{qu}^{(1)} + 0.155c_{qu}^{(8)} - 0.001c_{qd}^{(1)} + 0.0384c_{qd}^{(8)}$
$t\bar{t}H$, $200<p_{\mathrm{T}}^{H}<300$	$0.252c_G + 0.112c_{H\Box} - 0.0284c_{HDD} + 0.73c_{HG} + 0.001c_{HW} - 0.001c_{HWB} - 0.115c_{uH} - 1.03c_{uG} - 0.0106c_{uW} - 0.003c_{uB} - 0.115c_{Hl}^{(3)} - 0.001c_{Hq}^{(1)} + 0.0088c_{Hq}^{(3)} + 0.0582c'_{ll} + 0.0226c_{qq}^{(1)} + 0.409c_{qq} + 0.076c_{qq}^{(3)} + 0.88c_{qq}^{(31)} + 0.0270c_{uu} + 0.406c_{uu}^{(1)} - 0.004c_{ud}^{(1)} + 0.0617c_{ud}^{(8)} + 0.0163c_{qu}^{(1)} + 0.257c_{qu}^{(8)} - 0.002c_{qd}^{(1)} + 0.0616c_{qd}^{(8)}$
$t\bar{t}H$, $300<p_{\mathrm{T}}^{H}<450$	$0.43c_G + 0.110c_{H\Box} - 0.0278c_{HDD} + 0.87c_{HG} + 0.002c_{HW} - 0.001c_{HWB} - 0.110c_{uH} - 1.06c_{uG} - 0.0155c_{uW} - 0.0055c_{uB} - 0.112c_{Hl}^{(3)} - 0.0041c_{Hq}^{(1)} + 0.0238c_{Hq}^{(3)} + 0.0044c_{Hu} - 0.001c_{Hd} + 0.056c'_{ll} + 0.042c_{qq}^{(1)} + 0.73c_{qq} + 0.133c_{qq}^{(3)} + 1.53c_{qq}^{(31)} + 0.0464c_{uu} + 0.72c_{uu}^{(1)} - 0.0069c_{ud}^{(1)} + 0.102c_{ud}^{(8)} + 0.0264c_{qu}^{(1)} + 0.456c_{qu}^{(8)} - 0.003c_{qd}^{(1)} + 0.103c_{qd}^{(8)}$
$t\bar{t}H$, $450<p_{\mathrm{T}}^{H}$	$0.64c_G + 0.126c_{H\Box} - 0.031c_{HDD} + 1.26c_{HG} + 0.002c_{HW} - 0.001c_{HWB} - 0.091c_{uH} - 1.08c_{uG} - 0.0172c_{uW} - 0.0066c_{uB} - 0.083c_{Hl}^{(3)} - 0.0198c_{Hq}^{(1)} + 0.087c_{Hq}^{(3)} + 0.0212c_{Hu} - 0.0058c_{Hd} + 0.041c'_{ll} + 0.075c_{qq}^{(1)} + 1.39c_{qq} + 0.208c_{qq}^{(3)} + 2.72c_{qq}^{(31)} + 0.075c_{uu} + 1.37c_{uu}^{(1)} - 0.0099c_{ud}^{(1)} + 0.172c_{ud}^{(8)} + 0.037c_{qu}^{(1)} + 0.84c_{qu}^{(8)} - 0.0044c_{qd}^{(1)} + 0.172c_{qd}^{(8)}$
$\boldsymbol{tH}$	
tH	$0.1112c_{H\Box} - 0.0278c_{HDD} + 0.232c_{HG} + 0.1841c_{HW} - 0.0784c_{uH} - 0.116c_{uG} - 0.178c_{uW} - 0.274c_{Hl}^{(3)} + 0.321c_{Hq}^{(3)} + 0.1369c'_{ll} + 0.428c_{qq}^{(3)}$

Table 14: Parametrisation of the EFT interference terms normalized to the SM prediction for the decay widths of the considered Higgs boson decays as well as of the total Higgs boson width with the parameter definitions of the SMEFTsim model. The numbers are rounded according to their statistical uncertainty. Only terms with $\frac{\Gamma_{INT}}{\Gamma_{SM}} > 0.001\% c_i$ are considered.

Decay mode	Parameterisation
$H \to ZZ^* \to 4\ell$	0.119 $c_{H\Box}$ + 0.003 c_{HDD} - 0.303 c_{HW} - 0.200 c_{HB} + 0.299 c_{HWB} + 0.127 $c_{Hl}^{(1)}$ - 0.235 $c_{Hl}^{(3)}$ - 0.102 c_{He} + 0.181 c'_{ll}
$H \to WW^* \to l\nu l\nu$	0.122 $c_{H\Box}$ - 0.031 c_{HDD} - 0.096 c_{HW} + 0.006 c_{HB} + 0.002 c_{HWB} - 0.229 $c_{Hl}^{(3)}$ - 0.004 c_{He} + 0.183 c'_{ll}
$H \to \gamma\gamma$	-0.945 c_W + 0.121 $c_{H\Box}$ - 0.241 c_{HDD} - 13.065 c_{HW} - 40.113 c_{HB} + 22.379 c_{HWB} + 0.034 c_{uH} - 1.150 c_{uW} - 2.148 c_{uB} - 0.363 $c_{Hl}^{(3)}$ + 0.182 c'_{ll}
$H \to b\bar{b}$	0.121 $c_{H\Box}$ - 0.030 c_{HDD} - 0.121 c_{dH} - 0.121 $c_{Hl}^{(3)}$ + 0.061 c'_{ll}
$H \to \tau\tau$	0.121 $c_{H\Box}$ - 0.030 c_{HDD} - 0.121 c_{eH} - 0.121 $c_{Hl}^{(3)}$ + 0.061 c'_{ll}
$H \to$ all	0.001 c_W + 0.121 $c_{H\Box}$ - 0.030 c_{HDD} + 1.363 c_{HG} - 0.048 c_{HW} - 0.049 c_{HB} + 0.046 c_{HWB} - 0.005 c_{eH} - 0.012 c_{uH} - 0.085 c_{dH} + 0.051 c_{uG} - 0.002 c_{uW} - 0.003 c_{uB} - 0.151 $c_{Hl}^{(3)}$ + 0.013 $c_{Hq}^{(3)}$ + 0.079 c'_{ll}

Table 15: Parametrisation of the acceptance corrections in the relevant Higgs boson decay channels in terms of the EFT parameters defined in the SMEFTsim model. Corrections are obtained as a difference of the fiducial and the inclusive signal predictions for the considered decay vertex using the fully linearised signal parametrisation approach.

Decay mode	Acceptance Parameterisation
$H \to 4l$	$0.162 c_{HW} + 0.021 c_{HB} - 0.162 c_{HWB}$
ggH, $H \to l\nu l\nu$	$-0.007 c_{HW} + 0.006 c_{Hl}^{(3)}$
VBF, $H \to l\nu l\nu$	$-0.018 c_{HW} + 0.007 c_{Hl}^{(3)}$

References

[1] F. Englert and R. Brout, *Broken Symmetry and the Mass of Gauge Vector Mesons*, Phys. Rev. Lett. **13** (1964) 321 (cit. on p. 2).

[2] P. W. Higgs, *Broken symmetries, massless particles and gauge fields*, Phys. Lett. **12** (1964) 132 (cit. on p. 2).

[3] P. W. Higgs, *Broken Symmetries and the Masses of Gauge Bosons*, Phys. Rev. Lett. **13** (1964) 508 (cit. on p. 2).

[4] G. Guralnik, C. Hagen and T. Kibble, *Global Conservation Laws and Massless Particles*, Phys. Rev. Lett. **13** (1964) 585 (cit. on p. 2).

[5] P. W. Higgs, *Spontaneous symmetry breakdown without massless bosons*, Phys. Rev. **145** (1966) 1156 (cit. on p. 2).

[6] T. Kibble, *Symmetry breaking in non-Abelian gauge theories*, Phys. Rev. **155** (1967) 1554 (cit. on p. 2).

[7] ATLAS Collaboration, *Observation of a new particle in the search for the Standard Model Higgs boson with the ATLAS detector at the LHC*, Phys. Lett. B **716** (2012) 1, arXiv: 1207.7214 [hep-ex] (cit. on p. 2).

[8] CMS Collaboration, *Observation of a new boson at a mass of 125 GeV with the CMS experiment at the LHC*, Phys. Lett. B **716** (2012) 30, arXiv: 1207.7235 [hep-ex] (cit. on p. 2).

[9] ATLAS and CMS Collaborations, *Measurements of the Higgs boson production and decay rates and constraints on its couplings from a combined ATLAS and CMS analysis of the LHC pp collision data at $\sqrt{s} = 7$ and 8 TeV*, JHEP **08** (2016) 045, arXiv: 1606.02266 [hep-ex] (cit. on pp. 2, 4, 7, 26).

[10] ATLAS Collaboration, *Measurement of the properties of Higgs boson production at $\sqrt{s} = 13$ TeV in the $H \to \gamma\gamma$ channel using $139\,fb^{-1}$ of pp collision data with the ATLAS experiment*, ATLAS-CONF-2020-026, 2020, URL: https://cds.cern.ch/record/2725727 (cit. on pp. 2, 4, 17).

[11] ATLAS Collaboration, *Higgs boson production cross-section measurements and their EFT interpretation in the 4ℓ decay channel at $\sqrt{s} = 13$ TeV with the ATLAS detector*, Eur. Phys. J. C **80** (2020) 957, arXiv: 2004.03447 [hep-ex] (cit. on pp. 2, 4, 17, 39), Erratum: Eur. Phys. J. C **81** (2021) 29.

[12] ATLAS Collaboration, *Measurements of gluon fusion and vector-boson-fusion production of the Higgs boson in $H \to WW^* \to e\nu\mu\nu$ decays using pp collisions at $\sqrt{s} = 13$ TeV with the ATLAS detector*, ATLAS-CONF-2021-014, 2021, URL: https://cds.cern.ch/record/2759651 (cit. on pp. 2, 4).

[13] ATLAS Collaboration, *Measurements of Higgs boson production cross-sections in the $H \to \tau^+\tau^-$ decay channel in pp collisions at $\sqrt{s} = 13$ TeV with the ATLAS detector*, ATLAS-CONF-2021-044, 2021, URL: https://cds.cern.ch/record/2779179 (cit. on pp. 2, 4).

[14] ATLAS Collaboration, *Measurements of WH and ZH production in the $H \to b\bar{b}$ decay channel in pp collisions at 13 TeV with the ATLAS detector*, Eur. Phys. J. C **81** (2021) 178, arXiv: 2007.02873 [hep-ex] (cit. on pp. 2, 4).

[15] ATLAS Collaboration, *Measurement of the associated production of a Higgs boson decaying into b-quarks with a vector boson at high transverse momentum in pp collisions at $\sqrt{s} = 13$ TeV with the ATLAS detector*, Phys. Lett. B **816** (2021) 136204, arXiv: 2008.02508 [hep-ex] (cit. on pp. 2, 4).

[16] *Combination of measurements of Higgs boson production in association with a W or Z boson in the $b\bar{b}$ decay channel with the ATLAS experiment at $\sqrt{s} = 13$ TeV*, tech. rep., CERN, 2021, URL: https://cds.cern.ch/record/2782535 (cit. on pp. 2, 4).

[17] ATLAS Collaboration, *Measurements of Higgs Bosons Decaying to Bottom Quarks from Vector Boson Fusion Production with the ATLAS Experiment at $\sqrt{s} = 13$ TeV*, (2020), arXiv: 2011.08280 [hep-ex] (cit. on pp. 2, 4).

[18] ATLAS Collaboration, *Measurement of the Higgs boson decaying to $b-$quarks produced in association with a top-quark pair in pp collisions at $\sqrt{s}$ =13 TeV with the ATLAS detector*, CERN-EP-2021-202, 2021 (cit. on pp. 2, 4).

[19] ATLAS Collaboration, *Evidence for the associated production of the Higgs boson and a top quark pair with the ATLAS detector*, Phys. Rev. D **97** (2018) 072003, arXiv: 1712.08891 [hep-ex] (cit. on pp. 2, 4).

[20] ATLAS Collaboration, *A search for the dimuon decay of the Standard Model Higgs boson with the ATLAS detector*, Phys. Lett. B **812** (2021) 135980, arXiv: 2007.07830 [hep-ex] (cit. on pp. 2, 4, 30).

[21] ATLAS Collaboration, *A search for the $Z\gamma$ decay mode of the Higgs boson in pp collisions at $\sqrt{s} = 13$ TeV with the ATLAS detector*, Phys. Lett. B **809** (2020) 135754, arXiv: 2005.05382 [hep-ex] (cit. on pp. 2, 4).

[22] ATLAS Collaboration, *Search for invisible Higgs boson decays with vector boson fusion signatures with the ATLAS detector using an integrated luminosity of* $139\,fb^{-1}$, ATLAS-CONF-2020-008, 2020, URL: https://cds.cern.ch/record/2715447 (cit. on pp. 2, 4, 23, 27, 32).

[23] ATLAS Collaboration, *A combination of measurements of Higgs boson production and decay using up to* $139\,fb^{-1}$ *of proton–proton collision data at* $\sqrt{s} = 13$ *TeV collected with the ATLAS experiment*, ATLAS-CONF-2020-027, 2020, URL: https://cds.cern.ch/record/2725733 (cit. on pp. 2, 3, 8, 9, 26, 30, 44).

[24] ATLAS and CMS Collaborations, *Combined Measurement of the Higgs Boson Mass in* pp *Collisions at* $\sqrt{s} = 7$ *and* 8 *TeV with the ATLAS and CMS Experiments*, Phys. Rev. Lett. **114** (2015) 191803, arXiv: 1503.07589 [hep-ex] (cit. on p. 2).

[25] CMS Collaboration, *Measurements of Higgs boson production via gluon fusion and vector boson fusion in the diphoton decay channel at* $\sqrt{s} = 13$ *TeV*, CMS-PAS-HIG-18-029, 2019, URL: https://cds.cern.ch/record/2667225 (cit. on p. 2).

[26] CMS Collaboration, *Measurements of* $t\bar{t}H$ *Production and the CP Structure of the Yukawa Interaction between the Higgs Boson and Top Quark in the Diphoton Decay Channel*, Phys. Rev. Lett. **125** (2020) 061801, arXiv: 2003.10866 [hep-ex] (cit. on p. 2).

[27] CMS Collaboration, *Measurements of properties of the Higgs boson in the four-lepton final state in proton-proton collisions at* $\sqrt{s} = 13$ TeV, CMS-PAS-HIG-19-001, 2019, URL: https://cds.cern.ch/record/2668684 (cit. on p. 2).

[28] CMS Collaboration, *Measurements of properties of the Higgs boson decaying to a W boson pair in* pp *collisions at* $\sqrt{s} = 13$ *TeV*, Phys. Lett. B **791** (2019) 96, arXiv: 1806.05246 [hep-ex] (cit. on p. 2).

[29] CMS Collaboration, *Measurement of Higgs boson production and decay to the* $\tau\tau$ *final state*, CMS-PAS-HIG-18-032, 2019, URL: https://cds.cern.ch/record/2668685 (cit. on p. 2).

[30] CMS Collaboration, *Observation of Higgs Boson Decay to Bottom Quarks*, Phys. Rev. Lett. **121** (2018) 121801, arXiv: 1808.08242 [hep-ex] (cit. on p. 2).

[31] CMS Collaboration, *Measurement of* $\mathrm{t\bar{t}H}$ *production in the* $\mathrm{H} \to \mathrm{b\bar{b}}$ *decay channel in* $41.5\,\mathrm{fb}^{-1}$ *of proton-proton collision data at* $\sqrt{s} = 13$ TeV, CMS-PAS-HIG-18-030, 2019, URL: https://cds.cern.ch/record/2675023 (cit. on p. 2).

[32] CMS Collaboration, *Evidence for associated production of a Higgs boson with a top quark pair in final states with electrons, muons, and hadronically decaying* τ *leptons at* $\sqrt{s} = 13$ *TeV*, JHEP **08** (2018) 066, arXiv: 1803.05485 [hep-ex] (cit. on p. 2).

[33] CMS Collaboration, *Measurement of the associated production of a Higgs boson with a top quark pair in final states with electrons, muons and hadronically decaying* τ *leptons in data recorded in 2017 at* $\sqrt{s} = 13$ TeV, CMS-PAS-HIG-18-019, 2018, URL: https://cds.cern.ch/record/2649199 (cit. on p. 2).

[34] CMS Collaboration, *Search for the Higgs Boson Decaying to Two Muons in Proton–Proton Collisions at* $\sqrt{s} = 13$ *TeV*, Phys. Rev. Lett. **122** (2019) 021801, arXiv: 1807.06325 [hep-ex] (cit. on p. 2).

[35] CMS Collaboration, *Measurements of the Higgs boson width and anomalous HVV couplings from on-shell and off-shell production in the four-lepton final state*, Phys. Rev. D **99** (2019) 112003, arXiv: 1901.00174 [hep-ex] (cit. on p. 2).

[36] CMS Collaboration, *Combined Higgs boson production and decay measurements with up to 137 fb-1 of proton-proton collision data at* $\sqrt{s}$ = 13 TeV, CMS-PAS-HIG-19-005, 2020, URL: https://cds.cern.ch/record/2706103 (cit. on p. 2).

[37] LHC Higgs Cross Section Working Group, D. de Florian et al., *Handbook of LHC Higgs Cross Sections: 4. Deciphering the Nature of the Higgs Sector*, (2016), arXiv: 1610.07922 [hep-ph] (cit. on pp. 2, 3, 6, 9, 10, 13, 16, 17, 21, 25).

[38] J. R. Andersen et al., *Les Houches 2015: Physics at TeV Colliders Standard Model Working Group Report*, (2016), arXiv: 1605.04692 [hep-ph] (cit. on pp. 2, 16).

[39] N. Berger et al., *Simplified Template Cross Sections - Stage 1.1*, (2019), arXiv: 1906.02754 [hep-ph] (cit. on pp. 2, 16).

[40] S. Amoroso et al., 'Les Houches 2019: Physics at TeV Colliders: Standard Model Working Group Report', *11th Les Houches Workshop on Physics at TeV Colliders: PhysTeV Les Houches*, 2020, arXiv: 2003.01700 [hep-ph] (cit. on pp. 2, 16).

[41] LHC Higgs Cross Section Working Group, S. Heinemeyer et al., *Handbook of LHC Higgs Cross Sections: 3. Higgs Properties*, CERN-2013-004 (2013), arXiv: 1307.1347 [hep-ph] (cit. on pp. 2, 3, 23–25).

[42] I. Brivio and M. Trott, *The Standard Model as an Effective Field Theory*, Phys. Rept. **793** (2017) 1, arXiv: 1706.08945 [hep-ph] (cit. on p. 3).

[43] T. D. Lee, *A Theory of Spontaneous T Violation*, Phys. Rev. D **8** (1973) 1226 (cit. on p. 3).

[44] J. F. Gunion and H. E. Haber, *The CP conserving two Higgs doublet model: The Approach to the decoupling limit*, Phys. Rev. D **67** (2003) 075019, arXiv: hep-ph/0207010 (cit. on p. 3).

[45] G. Branco et al., *Theory and phenomenology of two-Higgs-doublet models*, Phys. Rept. **516** (2012) 1, arXiv: 1106.0034 [hep-ph] (cit. on pp. 3, 44).

[46] ATLAS Collaboration, *Interpretations of the combined measurement of Higgs boson production and decay*, ATLAS-CONF-2020-053, 2020, URL: https://cds.cern.ch/record/2743067 (cit. on pp. 3, 36, 37, 39, 43).

[47] ATLAS Collaboration, *The ATLAS Experiment at the CERN Large Hadron Collider*, JINST **3** (2008) S08003 (cit. on p. 3).

[48] ATLAS Collaboration, *ATLAS Insertable B-Layer Technical Design Report*, ATLAS-TDR-19; CERN-LHCC-2010-013, 2010, URL: https://cds.cern.ch/record/1291633 (cit. on p. 3), Addendum: ATLAS-TDR-19-ADD-1; CERN-LHCC-2012-009, 2012, URL: https://cds.cern.ch/record/1451888.

[49] B. Abbott et al., *Production and integration of the ATLAS Insertable B-Layer*, JINST **13** (2018) T05008, arXiv: 1803.00844 [physics.ins-det] (cit. on p. 3).

[50] ATLAS Collaboration, *Luminosity determination in pp collisions at* $\sqrt{s}$ = 13 *TeV using the ATLAS detector at the LHC*, ATLAS-CONF-2019-021, 2019, URL: https://cds.cern.ch/record/2677054 (cit. on p. 3).

[51] G. Avoni et al., *The new LUCID-2 detector for luminosity measurement and monitoring in ATLAS*, JINST **13** (2018) P07017 (cit. on p. 3).

[52] S. Agostinelli et al., *GEANT4—a simulation toolkit*, Nucl. Instrum. Methods **506** (2003) 250 (cit. on p. 3).

[53] ATLAS Collaboration, *The ATLAS Simulation Infrastructure*, Eur. Phys. J. C **70** (2010) 823, arXiv: 1005.4568 [physics.ins-det] (cit. on p. 3).

[54] A. Martin, W. Stirling, R. Thorne and G. Watt, *Parton distributions for the LHC*, Eur. Phys. J. C **63** (2009) 189, arXiv: 0901.0002 [hep-ph] (cit. on p. 3).

[55] ATLAS Collaboration, *Summary of ATLAS Pythia 8 tunes*, ATL-PHYS-PUB-2012-003, 2012, URL: https://cds.cern.ch/record/1474107 (cit. on p. 3).

[56] ATLAS Collaboration, *The Pythia 8 A3 tune description of ATLAS minimum bias and inelastic measurements incorporating the Donnachie–Landshoff diffractive model*, ATL-PHYS-PUB-2016-017, 2016, URL: https://cds.cern.ch/record/2206965 (cit. on p. 3).

[57] R. J. Barlow and C. Beeston, *Fitting using finite Monte Carlo samples*, Comput. Phys. Commun. **77** (1993) 219 (cit. on p. 5).

[58] K. Cranmer, G. Lewis, L. Moneta, A. Shibata and W. Verkerke, *HistFactory: A tool for creating statistical models for use with RooFit and RooStats*, CERN-OPEN-2012-016 (2012), URL: http://cdsweb.cern.ch/record/1456844 (cit. on p. 5).

[59] G. Cowan, K. Cranmer, E. Gross and O. Vitells, *Asymptotic formulae for likelihood-based tests of new physics*, Eur. Phys. J. C **71** (2011) 1554, arXiv: 1007.1727 [physics.data-an], Erratum: Eur. Phys. J. C73 (2013) 2501 (cit. on pp. 6, 7).

[60] A. L. Read, *Presentation of search results: the CL_s technique*, J. Phys. G **28** (2002) 2693 (cit. on p. 6).

[61] ATLAS Collaboration, *Measurement of the dijet momentum balance in Pb+Pb and pp collisions at $\sqrt{s_{NN}} = 5.02$ TeV with the ATLAS detector*, ATLAS-CONF-2020-017, 2020, URL: https://cds.cern.ch/record/2720247 (cit. on p. 9).

[62] ATLAS Collaboration, *Evaluation of theoretical uncertainties for simplified template cross section measurements of V-associated production of the Higgs boson*, ATL-PHYS-PUB-2018-035, 2018, URL: https://cds.cern.ch/record/2649241 (cit. on p. 17).

[63] ATLAS Collaboration, *Combined measurements of Higgs boson production and decay using up to $80\,fb^{-1}$ of proton–proton collision data at $\sqrt{s} = 13$ TeV collected with the ATLAS experiment*, Phys. Rev. D **101** (2020) 012002, arXiv: 1909.02845 [hep-ex] (cit. on p. 24).

[64] ALEPH, CDF, D0, DELPHI, L3, OPAL, SLD Collaborations; LEP and Tevatron Electroweak Working Group; and SLD Electroweak and Heavy Flavour Groups, *Precision Electroweak Measurements and Constraints on the Standard Model*, (2010), arXiv: 1012.2367 [hep-ex] (cit. on p. 34).

[65] C. Degrande, B. Fuks, K. Mawatari, K. Mimasu and V. Sanz, *Electroweak Higgs boson production in the standard model effective field theory beyond leading order in QCD*, Eur. Phys. J. **C77** (2017) 262, arXiv: 1609.04833 [hep-ph] (cit. on p. 36).

[66] B. Grzadkowski, M. Iskrzynski, M. Misiak and J. Rosiek, *Dimension-Six Terms in the Standard Model Lagrangian*, JHEP **10** (2010) 085, arXiv: 1008.4884 [hep-ph] (cit. on p. 36).

[67] J. Alwall et al., *The automated computation of tree-level and next-to-leading order differential cross sections, and their matching to parton shower simulations*, JHEP **07** (2014) 079, arXiv: 1405.0301 [hep-ph] (cit. on p. 37).

[68] I. Brivio, *SMEFTsim 3.0 – a practical guide*, JHEP **04** (2021) 073, arXiv: 2012.11343 [hep-ph] (cit. on p. 37).

[69] C. Degrande et al., *Standard Model Effective Theory at Next-to-Leading-Order in QCD*, URL: http://feynrules.irmp.ucl.ac.be/wiki/SMEFTatNLO (cit. on p. 37).

[70] S. Dawson and P. P. Giardino, *Electroweak corrections to Higgs boson decays to $\gamma\gamma$ and W^+W^- in standard model EFT*, Phys. Rev. D **98** (2018) 095005, arXiv: 1807.11504 [hep-ph] (cit. on p. 37).

[71] S. L. Glashow and S. Weinberg, *Natural Conservation Laws for Neutral Currents*, Phys. Rev. D **15** (1977) 1958 (cit. on p. 44).

[72] E. A. Paschos, *Diagonal Neutral Currents*, Phys. Rev. D **15** (1977) 1966 (cit. on p. 44).

[73] ATLAS Collaboration, *Constraints on new phenomena via Higgs boson couplings and invisible decays with the ATLAS detector*, JHEP **11** (2015) 206, arXiv: 1509.00672 [hep-ex] (cit. on p. 44).